Synthesis of Nitrogen-Doped Graphene-Coated Metal Nanoparticles and Their Catalysis for the Oxygen Reduction Reaction

PHAN Phu Quoc

Synthesis of Nitrogen-Doped Graphene-Coated Metal Nanoparticles and Their Catalysis for the Oxygen Reduction Reaction

A Doctoral Dissertation by

PHAN Phu Quoc

2020

Graduate School of Engineering,

Department of Chemical Systems Engineering,

Nagoya University

Table of Content

Acknowledgements

This thesis was carried out during my PhD study at the Department of Chemical Systems Engineering, Graduate School of Engineering, Nagoya University under the supervision of Professor Nagahiro Saito. This work has been financially supported by the Japan Science and Technology Corporation-Strategic International Collaborative Research Program (Grant number: JPMJSC18H1) and the Japan Science and Technology Corporation-Open Innovation Platform with Enterprises, Research Institute, and Academia (Grant number: JPMJOP1843).

I would like to greatly acknowledge the study support from JICA Technical Cooperation Project for ASEAN University Network/Southeast Asia Engineering Education Development Network (Program number: J-1710176) for my study in Japan. I am very thankful to JICA and JICA's staff members for always taking care of me during the time I live in Japan.

I would like to express my appreciation to Professor Nagahiro Saito for allowing me to work in his group, for his professional guidance, and for his kindness in supporting me during my study at Nagoya University.

I would also like to thank Saito’s laboratory members for creating a good working atmosphere, for sharing their knowledge in experimental, and for giving their valuable feedback on my research.

I would like to thank Assistant Professor Takeshi Hagio from Institutes of Innovation for Future Society for providing me with the ICP-OES measurement and for teaching me the related knowledge in my experiment.

Finally, I would love to thank my family for their love, support, and patience through all these years. Thank you for encouraging my dream of becoming an expert in my chosen career. Furthermore, I would also like to thank my all friends and colleagues who have supported me.

Sincerely,

Phan Quoc Phu

Abstract

The proton exchange membrane fuel cell (PEMFC) has the potential to become a future green energy source as an alternative to fossil fuels. The platinum (Pt) catalyst is a practical catalyst for PEMFC owing to its low overpotential for oxygen reduction reaction (ORR) and fast reaction rate. However, the development of alternative materials is still essential due to the remaining issues of the Pt catalyst, including the high cost, low durability, and poor tolerance to poisoning. To overcome these drawbacks, I have proposed the possibility of applying nitrogen-doped graphene-coated metal nanoparticles (hereinafter referred to as core-shell nanoparticles) as a solution, in which nitrogen-doped few-layer graphene (NFG) is coated on Pt-based bimetallic nanoparticles. The NFG layer not only protects the metal-core but also causes localization of the π-conjugated system induced by nitrogen doping in graphene. Therefore, the ORR activity can be expected to enhance depending on the relationship between the Fermi level of the core metal. In this thesis, the development of a novel synthesis process for the core-shell nanoparticles by the solution plasma (SP) method as well as their ORR properties and corrosion resistance were evaluated. The possibility to overcome the trade-off characteristics by the proposed structure is verified.

Chapter 1 provides an overview of the current state of the world regarding PEMFC, redox platinum catalysts, and the metal-carbon core-shell structure synthesis techniques and clarifies the superiority of the method applied in this study, namely the SP method for synthesizing both the metal-core and the NFG-shell.

Chapter 2 shows the results of the synthesis, structural analysis, and corrosion resistance test of the core-shell nanoparticles with Cu-core (Cu-NFG) prepared by the SP method. The synthesized Cu-NFG consists of a shell of 3-5 layers of nitrogen-doped graphene and a core of Cu nanoparticles. As a result of an immersion test in an acidic solution for 48 hours, the elution

of the Cu-core in the presence of NFG-shell was revealed to be reduced to below one-tenth compared to that of bare Cu nanoparticles.

Chapter 3 shows the results of the synthesis and catalytic performance of the core-shell nanoparticles with Pt-core (Pt-NFG) prepared via the SP method. Compared with the commercial Pt/C catalyst, the synthesized Pt-NFG nanoparticles have higher reaction selectivity against the 4-electron pathway for ORR in an acidic medium. Furthermore, it demonstrated that the durability in immersion tests is improved compared to that of the commercial Pt/C catalyst.

Chapter 4 shows the results on the synthesis and catalytic performance of the core-shell nanoparticles with Pt-based bimetallic core (PtM-NFG) prepared using the SP method. It was found that a higher ORR performance than the Pt-NFG nanoparticle can be obtained when the Pt-core is replaced with the PtPd bimetallic nanoparticle.

Finally, Chapter 5 summarizes the results of Chapters 2 to 4 and concludes with a general remark. It was shown that the formation of a core-shell structure by coating the metal catalyst with the NFG-shell makes it possible to prevent corrosion from the surrounding acidic solution without deactivating the catalyst properties of the metal-core. Because the results of this study reveal the possibility of developing a novel catalyst with higher catalytic performance and durability than Pt by designing the bimetal for the metal-core and type and amount of dopant in the graphene shell, an alternative catalyst for PEMFC with low-cost must be developed in the near future by utilizing material design methods such as first-principles calculations.

Chapter 1

General Introduction

Chapter 1 - General Introduction

1.1 Proton exchange membrane fuel cell

Energy consumption, based on hydrocarbon sources (e.g., coal, oil, and gas), has been rising globally, causing enormous pollution amount as well as fossil sources depletion. According to concerns from many sectors, the finding of eco-friendly alternative sources of energy has drawn much attention. As one of the leading clean energy sources, fuel cell, discovered by Sir William Grove in 1839, is the effective conversion system of chemical energy into electricity with low environmental impact. In the last few decades, the fuel cell systems have been developing into six main types, including proton exchange membrane fuel cell (PEMFC), phosphoric acid fuel cell (PAFC), direct methanol fuel cell (DMFC), alkaline fuel cell (AFC), solid oxide fuel cell (SOFC) and molten carbonate fuel cell (MCFC).[1] The characteristics of each fuel cell system are displayed in Table 1.1. Fuel cell systems have been extensively utilized for several applications such as transportation, heating, and power production, due to their effective electrical transfer, compact size, and low operation noise.

Table 1.1 Different fuel cell types and characteristic.[1]

Type	Mobile ion	Working temperature (ºC)	Catalyst
PEMFC	H^+	30–100	Pt
PAFC	H^+	175–210	Pt
DMFC	H^+	20–90	Pt, Pt/Ru
AFC	OH^-	70–130	Ni, Ag, Pt
SOFC	O^{2-}	500–1000	Perovskites, Ni
MCFC	CO_3^{2-}	550–650	Ni

Among the mentioned fuel cell types, the PEMFC has been indicated as a promising electrochemical energy conversion system for various applications such as automobile, stationary, and compact power devices.[2] Especially, the PEMFC systems demonstrate the efficient energy conversion, low working temperature, low noise, compact and lightweight systems which are normally desired in vehicle developments.[3] The PEMFC system is composed of a proton exchange membrane placed between cathode and anode electrodes followed by two gas diffusion channels. The whole basic construction, named a membrane electrode assembly (MEA), is shown in Figure 1.1.

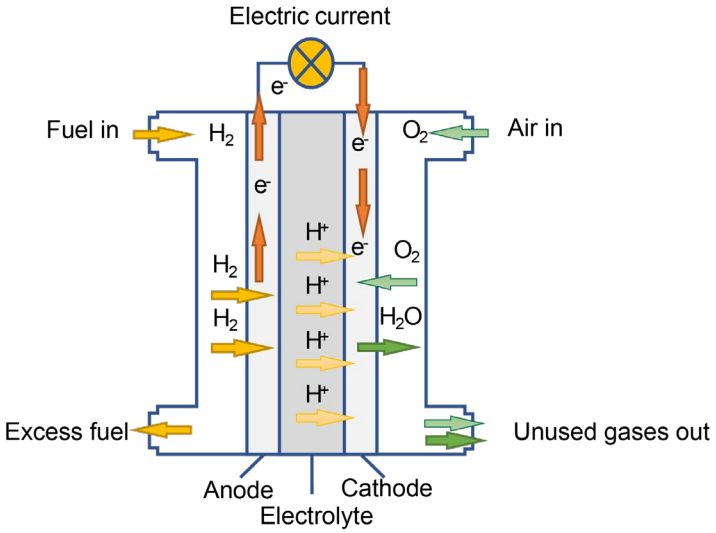

Figure 1.1 Sketch MEA construction diagram of the PEMFC single-cell.[4]

According to Figure 1.1, the PEMFC system is operated with the supply of hydrogen and oxygen gases to the anode and cathode through the flow channels, respectively.[5] At the anode, the hydrogen fuel will be oxidized and split to create protons and electrons as below:

$$2H_2 \rightarrow 4H^+ + 4e^- \quad (1)$$

the proton exchange membrane plays an important role to conduct only the generated protons from anode to cathode. The electrons move from the conductive anode to the cathode through the current collector which electricity is produced. When the circuit is connected, the oxygen reduction reaction (ORR) can be occurred at the cathode through the combination of protons on

the membrane electrolyte, the electrons arriving from the collector, and the supplied oxygen to form water, as shown below:

$$O_2 + 4H^+ + 4e^- \rightarrow 2H_2O \quad (2)$$

Overall, the obtain current indicates the electrical direct current based on the reaction of the PEMFC operation as shown below:

$$2H_2 + O_2 \rightarrow 2H_2O \quad (3)$$

Until now, the commercialization of the PEMFC systems in vehicle applications have been succeeded such as Toyota Mirai,[6] Hyundai Nexo,[7] and Mercedes-Benz.[8] However, there are still significant challenges due to the drawbacks of high cost, low durability, and requirement of an optimized design which need to overcome for broadening their applications.

1.2 Catalyst for PEMFC

In the PEMFC system, the most important part is the MEA which can directly convert chemical reactions to electricity, including the ORR and the hydrogen oxidation reaction (HOR). The catalyst used in the cathode of the MEA, where the ORR occurs, is an important key for optimizing the fuel cell efficiency, due to its much larger overpotential than that of the HOR. Many researchers have been focusing on the enhancement of the cathode catalytic performances as well as the support materials.

1.2.1 Platinum (Pt) alloys catalyst

Platinum (Pt) has been used as the common catalyst for both electrode sides of the MEA in the PEMFC system. However, the Pt catalyst indicated several drawbacks of the high cost, low poisoning resistance, and dramatic agglomeration as well as it catalyzes the corrosion process of the carbon support in the PEMFC.[9-11] For minimizing the used amount of catalyst amount, alloying Pt with the other metal to form PtM nanoparticles is one of the promising methods. Especially, the PtM nanoparticles can not only help to approach the target of reducing the amount of Pt but also show higher catalytic activities such as the Pt_3Au, Pt_3Ag, and Pt_3Pd alloys.[12-14] The

higher activity of the PtM alloys comparing to the pure Pt nanoparticles can be explained by the two theories including compressive strain and electronic ligand effects (Figure 1.2). The compressive strain effect relates to the decrease of the Pt lattice parameter due to the incorporation of the small-sized transition metal atoms to the Pt lattice structure which weaken the interaction of the Pt surface with adsorbates. The electronic ligand effect can be caused by the charge transfer from transition metal atoms to Pt atoms in the PtM alloy systems which can alter the binding energies to the reactants, intermediates, and products of the ORR on the Pt surface. According to the various compositions, structures, and shapes of the PtM alloys, the ORR activities have been extensively studied and proved that alloying can enhance the ORR activity. However, the PtM alloys still show the dissolution and oxidation from the transition metals which significantly cause the lowering of the ORR performance as prolonging the operation time.[15] Therefore, the protection of the transition metal in PtM alloy becomes the next challenge to scientists and researchers.

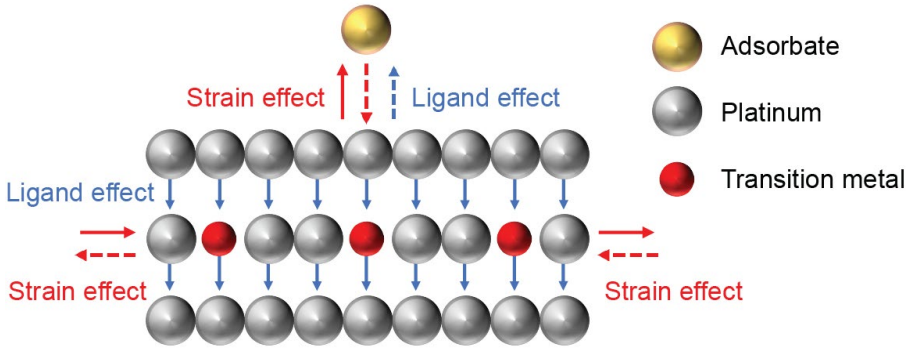

Figure 1.2 Ligand and strain effects in PtM alloy.[16]

1.2.2 Nitrogen-doped graphene

Graphene has been gained enormous attraction in the utilization for both improving the catalyst performance and increasing the lifetime of the PEMFC, due to its great electronic conductivity, charge mobility, and electrochemical stability. The pristine graphene has commonly been used as a support material to assist and strengthen the Pt catalyst due to its low active characteristic of two-dimensional sp^2 bonded carbon in the hexagonal lattice structure. However,

it was found that the pristine graphene could limit the ORR activity and lead to the unfavourable two-electron reduction pathway at the cathode of the PEMFC as shown below:

$$O_2 + 2H^+ + 2e^- \rightarrow H_2O_2 \quad (4)$$

One of the methods for tailoring the graphene characteristic is the introduction of heteroatom dopants on its structure such as nitrogen, boron, sulfur, or combination atoms.[17-20] The heteroatom dopants play as the nucleation sites which modify the electronic structure of graphene to the more active to the ORR activity. Especially, nitrogen-doped graphene (NG) has been one of the most investigated materials due to the doping of the comparable atomic size of the nitrogen atom (65 pm) compared to that of the carbon atom (70 pm). Previous studies explained that the electrochemical of graphene was enhanced remarkably by replacing some carbon atoms with nitrogen atoms. There are several NG catalysts have been synthesized and used as the cathode in the PEMFC and showed high potential as an effective electrocatalyst toward the ORR application. Several reports have drawn the contribution of the nitrogen dopant to the ORR activity in the NG based on the pyridinic N, graphitic N, pyrrolic N, and oxidized N components.[21] Although the high potential of replacing Pt catalyst by the NG for the PEMFC has been shown, the development of the NG catalyst to gain high ORR performance is still the long-term research for commercialization. Therefore, the NG catalysts still need further study to achieve comparable catalyst performance toward the Pt catalyst.

1.2.3 Nitrogen-doped graphene PtM alloy composites

To exploit the co effects of the NG and PtM alloy catalysts, the composite structures of them have been focusing on research and demonstrated the promising potential for using in the PEMFC. In theory, the NG indicates the increases of the binding energy of the Pt atom to the substrate which improves the Pt catalyst durability.[22] The formation of Pt atom on the 3 Pyridinic N (Pt-N3) lines up its Pt binding energy to –4.47 eV which makes difficult to Pt diffusion and aggregation. Besides that, the Pt-N interaction also enhances activation of O_2 due to the up-shifted of the Pt-d states.[23] Based on this theory, several reports indicated the high electrochemical

stability of the PtM alloy with NG in the PEMFC.[24-26] However, the leaching of the transition metal in the PtM alloy still causes the low durability of these catalysts. As one of the theoretical methods, completely coating the metal surface with a high stability carbon layer, especially the core-shell structure, is the common method to protect the metal-core.[27-29] Especially, the unique NG encapsulated metal nanoparticle core-shell can not only enhance the stability of the catalyst from the corrosion but also play as the active site for the reaction.[30] However, the protection ability as well as the reaction mechanism of the NG in the core-shell has not been targeted. From this point of view, the core-shell structure of the PtM alloy coated by the NG has been laying the new wide field for scientists and researchers who are looking for the ideal structure of the high durability and efficiency activity in electrocatalytic processes.

1.3 Methods for fabricating metal-carbon core-shell

The core-shell structure of the metal nanoparticle encapsulated by the carbon layer has been indicated as a promising catalyst type for electrochemical applications. Several methods have been applying to synthesize these mentioned complicated structures. However, a finding of the simple and effective synthesis method for the mentioned complicated structure is still challenging for researchers and scientists.

1.3.1 Chemical vapor deposition

Chemical vapor deposition (CVD) has been the common method to coating the high quality of graphene to the surface of the metal substrate. By modifying the synthesis conditions, the controllability of the shell thickness and quality can be obtained.[31] There are some researchers reported about the high quality of the carbon-metal core-shell structures using CVD such as Cu nanoparticle encapsulated graphene,[32] $SrTiO_3$ coated by graphene structure,[33] CoO coated by onion-like layered graphitic carbon[34] and so on. However, the complicated set-up, high temperature, and inert gas requirement cause the disadvantage of applying this method to fabricate the cheap catalyst for the PEMFC.

1.3.2 Thermal treatment

Thermal treatment is the fast developing and economical method for synthesizing the core-shell structure during the heating process. This method has been used for synthesizing PtCo bimetallic nanoparticle coated by nitrogen-doped hollow porous carbon capsules,[35] nitrogen-doped carbon shell encapsulated PtZn intermetallic nanoparticle,[36] IrCo nanoalloys wrapped in nitrogen-doped carbon cages,[37] etc. However, the high temperature is needed for rapid decomposition of organic compounds causing the uncontrollable drawbacks of possibly a thermal runaway and an explosion of the other chemical reaction during the heat treatment process.

1.3.3 Hydrothermal method

Hydrothermal method is another approach for generating the metal-carbon core-shell nanoparticles via a sealed and heated solution about ambient temperature and pressure. Accordingly, various types of metal particle cores coated by carbon nanospheres were prepared such as gold (Au), silver (Ag), or nickel (Ni) using the hydrothermal method.[38-40] This method indicated the advantage of the environment-friendliness system, the lower temperature operation at under 300 ºC, one-step synthetic procedure, and good dispersion in solution. However, the carbon shell indicated the amorphous structures which commonly conduct low electrical conductivity material.

1.3.4 Solution plasma

Solution plasma (SP), a non-equilibrium plasma discharge in liquid, has been using for various types of nanoparticle synthesis, especially, metal-carbon composites.[41-44] There are the carbonization and sputtering process which generate the carbon and metal particles during the SP. Based on the controllability of the carbonization and sputtering rates, the SP has been indicating the high potential in the synthesis of the metal-carbon core-shell materials as shown in Figure 1.3. Besides that, the solution plasma can be occurred as the low temperature, atmospheric pressure,

simple set up and facile synthesis which represents the promising method to synthesize the PtM alloys coated by the NG layer.

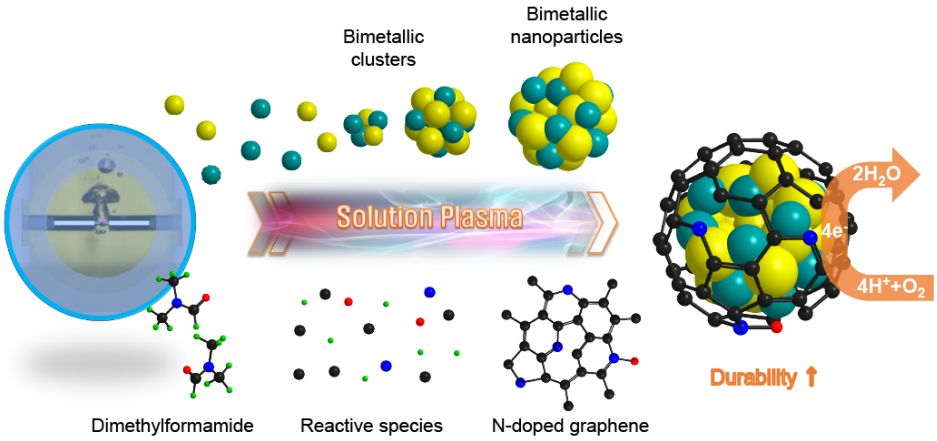

Figure 1.3 Solution plasma process of synthesis PtM alloy coated by NG.

1.4 Scope and outline of the thesis

By applying the metal-carbon core-shell catalyst in the PEMFC system, it was expected to enhance corrosion resistance in an acidic medium, increase durability during the operation time and improve catalytic performances. The purpose of our research is to synthesize a few-layer of the NG coating on the metal nanoparticles and illustrate their performances, including the high protection to the metal-core of a poor oxidization resistance and the synergistic effect of the synthesized metal-core and nitrogen-doped carbon shell on the ORR.

In this work, we addressed not only research on the in-situ synthesis of the metal-carbon core-shell structure using plasma discharge in organic solution but also evaluation of the catalytic activity for the ORR. The study contents were carried out as shown below:

Chapter 1, general introductions of the current status of the PEMFC, the Pt catalyst, and the synthesis methods for the metal-carbon core-shell structures were introduced in this chapter. Especially, we presented the development of a simple method, namely solution plasma (SP), for the synthesis of the metal-carbon core-shell nanoparticle.

Chapter 2, the copper (Cu) nanoparticle encapsulated by nitrogen-doped few-layer graphene (NFG) core-shell was successfully synthesized by the SP. The shell containing 3 to 5

layers of the NG revealed the high protection on the Cu-core which has very poor oxidation resistance according to the immersion test using acid solutions in 48 h.

Chapter 3, the synthesis and electrocatalytic evaluation of Pt nanoparticles encapsulated by the NFG coating (Pt-NFG) were described in this chapter. By comparing with the commercial Pt/C, the synthesized Pt-NFG nanoparticles exhibited higher durability with the higher selectivity toward the four-electron ORR under acid medium.

Chapter 4, the efficient ORR electrocatalytic activity of the NFG coated on the Pt-based bimetallic nanoparticle were explored. Their synthesis could be conducted via the SP process in one-pot by simply changing the metal electrodes. The NFG coated on the PtPd bimetallic nanoparticle core-shell products could be obtained as high-performance ORR catalysts. Besides, the PtPd-NFG nanoparticles exhibited comparable catalytic performance to the commercial Pt/C, according to single-cell testing.

Chapter 5, the summaries of researches in the thesis were concluded.

References

1. P. P. Edwards, V. L. Kuznetsov, W. I. David and N. P. Brandon, *Energy policy*, 2008, **36**, 4356-4362.
2. N. Bizon, A. G. Mazare, L. M. Ionescu and F. M. Enescu, *Energy Convers. Manage.*, 2018, **163**, 22-37.
3. C. Wang, S. Wang, L. Peng, J. Zhang, Z. Shao, J. Huang, C. Sun, M. Ouyang and X. He, *Energies*, 2016, **9**, 603.
4. K. Javed, R. Gouriveau, N. Zerhouni and D. Hissel, *J. Power Sources*, 2016, **324**, 745-757.
5. W. Vielstich, A. Lamm and H. A. Gasteiger, *Handbook of fuel cells: fundamentals technology and applications*, Wiley New York, 2003.
6. T. Yoshida and K. Kojima, *Electrochem. Soc. Interface*, 2015, **24**, 45.
7. B. K. Hong and S. H. Kim, *ECS Trans.*, 2018, **86**, 3.
8. M. Venturi, C. Mohrdieck and J. Friedrich, *IEEE*, 2013, 1-13.

9. B. Randrianarizafy, P. Schott, M. Gerard and Y. Bultel, *Energies*, 2020, **13**, 2338.
10. A. de Frank Bruijn and G. J. Janssen, *Fuel Cells*, Springer, 2013, 249-303.
11. B. Shabani, M. Hafttananian, S. Khamani, A. Ramiar and A. Ranjbar, *J. Power Sources*, 2019, **427**, 21-48.
12. K.-S. Lee, H.-Y. Park, H. C. Ham, S. J. Yoo, H. J. Kim, E. Cho, A. Manthiram and J. H. Jang, *J. Phys. Chem. C*, 2013, **117**, 9164-9170.
13. S. Beckord, A. K. Engstfeld, S. Brimaud and R. J. Behm, *J. Phys. Chem. C*, 2016, **120**, 16179-16190.
14. Y. Tang, F. Gao, S. Mu, S. Yu and Y. Zhao, *Russ. J. Electrochem.*, 2015, **51**, 345-352.
15. C. Zhang, X. Shen, Y. Pan and Z. Peng, *Front. Energy*, 2017, **11**, 268-285.
16. S. G. Peera, T. G. Lee and A. K. Sahu, *Sustain. Energy Fuels*, 2019, **3**, 1866-1891.
17. X. Hou, Q. Hu, P. Zhang and J. Mi, *Chem. Phys. Lett.*, 2016, **663**, 123-127.
18. G. Fazio, L. Ferrighi and C. Di Valentin, *J. Catal.*, 2014, **318**, 203-210.
19. A. Marinoiu, I. Gatto, M. Raceanu, M. Varlam, C. Moise, A. Pantazi, C. Jianu, I. Stefanescu and M. Enachescu, *Int. J. Hydrog. Energy*, 2017, **42**, 26877-26888.
20. L. Samiee, S. Sadeghhassani, M. R. Ganjali and A. Rashidi, *IJHFC*, 2018, **4**, 231-240.
21. L. Lai, J. R. Potts, D. Zhan, L. Wang, C. K. Poh, C. Tang, H. Gong, Z. Shen, J. Lin and R. S. Ruoff, *Energy Environ. Sci.*, 2012, **5**, 7936-7942.
22. M. Groves, A. Chan, C. Malardier-Jugroot and M. Jugroot, *Chem. Phys. Lett.*, 2009, **481**, 214-219.
23. X. Liu, Y. Sui, T. Duan, C. Meng and Y. Han, *Catal. Sci. Technol.*, 2015, **5**, 1658-1667.
24. M. González-Hernández, E. Antolini and J. Perez, *Int. J. Hydrogen Energy*, 2020, **45**, 5276-5284.
25. B. P. Vinayan, R. Nagar, N. Rajalakshmi and S. Ramaprabhu, *Adv. Funct. Mater.*, 2012, **22**, 3519-3526.
26. X. Zhong, W. Xu, L. Wang, Y. Qin, G. Zhuang, X. Li and J.-g. Wang, *Catal. Sci. Technol.*, 2016, **6**, 5942-5948.

27. T. D. Thanh, N. D. Chuong, H. V. Hien, N. H. Kim and J. H. Lee, *ACS Appl. Mater. Interfaces*, 2018, **10**, 4672-4681.
28. X. Zhang, J. Lin, S. Chen, J. Yang, L. Song, X. Wu and H. Xu, *ACS Appl. Mater. Interfaces*, 2017, **9**, 38499-38506.
29. F. Zhang, Y. Zhu, Y. Chen, Y. Lu, Q. Lin, L. Zhang, S. Tao, X. Zhang and H. Wang, *J. Mater. Chem. A*, 2020, **8**, 12810-12820.
30. Y. Peng and S. Chen, *Green Energy Environ.*, 2018, **3**, 335-351.
31. N. Wang, Z. Yang, F. Xu, K. Thummavichai, H. Chen, Y. Xia and Y. Zhu, *Sci. Rep.*, 2017, **7**, 1-9.
32. S. Chen, A. Zehri, Q. Wang, G. Yuan, X. Liu, N. Wang and J. Liu, *ChemistryOpen*, 2019, **8**, 58-63.
33. C. He, X. Bu, S. Yang, P. He, G. Ding and X. Xie, *Appl. Surf. Sci.*, 2018, **436**, 373-381.
34. J. Liu, Y. Xu, X. Ma, J. Feng, Y. Qian and S. Xiong, *Nano Energy*, 2014, **7**, 52-62.
35. J. Ying, J. Li, G. Jiang, Z. P. Cano, Z. Ma, C. Zhong, D. Su and Z. Chen, *Appl. Catal. B.*, 2018, **225**, 496-503.
36. Y. Xue, H. Li, X. Ye, S. Yang, Z. Zheng, X. Han, X. Zhang, L. Chen, Z. Xie and Q. Kuang, *Nano Res.*, 2019, **12**, 2490-2497.
37. P. Jiang, J. Chen, C. Wang, K. Yang, S. Gong, S. Liu, Z. Lin, M. Li, G. Xia and Y. Yang, *Adv. Mater.*, 2018, **30**, 1705324.
38. Z. Gan, Z. Chen, L. Liu, L. Zhang, W. Tu and Y. Liu, *Solar RRL*, 2017, **1**, 1600032.
39. H. Song, J. Huang, X. Jia and W. Sheng, *New J. Chem.*, 2018, **42**, 8773-8782.
40. Z. Wang, C. Lu, W. Kong, Y. Zhang and J. Li, *J. Alloys Compd.*, 2017, **690**, 95-100.
41. J. Kang, O. L. Li and N. Saito, *Nanoscale*, 2013, **5**, 6874-6882.
42. J. Kang and N. Saito, *RSC Adv.*, 2015, **5**, 29131-29134.
43. J. Kang, Y. Kim, H.-m. Kim, X. Hu, N. Saito, J.-H. Choi and M.-H. Lee, *Sci. Rep.*, 2016, **6**, 38652.
44. D.-w. Kim, O. L. Li, P. Pootawang and N. Saito, *RSC Adv.*, 2014, **4**, 16813-16819.

Chapter 2

Solution Plasma Synthesis of Remarkable Corrosion Resistance of Nitrogen-Doped Few-Layer Graphene Coated on Copper Nanoparticles

Chapter 2 - Solution Plasma Synthesis of Remarkable Corrosion Resistance of Nitrogen-Doped Few-Layer Graphene Coated on Copper Nanoparticles

2.1. Introduction

Up to now, graphene has been received enormous consideration in researches due to its fascinating properties such as high electrical, thermal, optical, and mechanical properties.[1] Especially, graphene has also demonstrated strong stability in terms of chemical, thermal and mechanical resistances.[2] Thus, it has been used as an effective protective coating for metal surfaces from some hazardous conditions, such as corrosion and oxidation, which can be beneficial in various applications. Due to the development of technology, the protection ability of graphene also has been focused on improving the stability of metal nanoparticles in terms of core-shell nanostructures.[3] A pristine graphene bilayer played as a high-energy barrier which hindered the oxygen diffusion to the metal core leading to better protection from oxidation.[4] However, the surface activity of the coated product is lowered in some cases leading to the limitation application such as a catalyst in the electrochemical reaction. The lowering of the surface activeness was affected by the existence of the only sp^2 hybridized carbon-carbon bonding of graphene coating.[4] To improve the surface activity, the production of several heteroatoms into the graphene framework regularly can provide active sites due to the different electronegativity between doping atoms and carbon atoms.[5] Especially, the nitrogen atom has been demonstrated as an efficient dopant due to its extraordinary effect on tailoring the electronic, chemical, and structural properties of graphene.[6] Therefore, the encapsulation of metal nanoparticles by nitrogen-doped graphene (NG) indicates the ideal structure for improving the chemical stability as well as the surface activity of the fabricated products.

In the past years, a chemical vapor deposition (CVD) has been applied as the favored method to introduce carbon to the surface of the metal with high quality. For instance, Lee *et. al*.

described a one-step fabrication of a scalable process for growing graphene-coated germanium (Ge) under the thermal pyrolysis of Ge with methane at 900 ºC under argon atmosphere using CVD.[7] As the improved CVD methods, the facial manufacturing method of cold wall reactors has been successfully prepared the graphene-encapsulated Cu nanoparticles at a lower temperature by 775 ºC with pressure at 0.1 mbar by Chen *et. al*.[8] Although the CVD showed an excellent performance to synthesize, it needs a huge amount of inert gas consumption, leading to the high cost of the synthesized material. A more straightforward technique of detonation method was developed by An *et. al.* for the synthesis of carbon-coated Cu nanoparticles using a combination of hexahydro–1,3,5–trinitro–1,3,5–triazine, wax, and Cu nitrate hydrate.[9] However, an abnormally high temperature and pressure around 3053 K and 21 GPa were required. The solid-state reduction reaction method used by Li *et. al.* reported the synthesis of carbon-coated Cu nanoparticles at a low temperature of 350 ºC under the nitrogen atmosphere.[10] However, the coating was found to be an amorphous structure of carbon material, which lowers the conductivity of a material. As mentioned above, modern methods consume high technology or need an extreme reaction condition and cannot achieve a coating at ambient conditions. Therefore, there are still rooms for discovering an alternative approach, which is simple and able to be operated at a room temperature and pressure condition.

Recently, solution plasma (SP) was successfully used to synthesize many kinds of contents, such as metal and bimetal nanoparticles manufactured in an aqueous solution,[11-13] allotropes of carbon materials from organic solvents,[14-16] as well as composite materials between carbon and metallic elements.[17-19] However, there was still no report to fabricate metal encapsulated with the NG by using SP. In this work, the SP synthesis of the carbon-metal core-shell nanostructured material was introduced in detail for the first time. Besides that, the copper (Cu) electrode was chosen for fabricated Cu nanoparticles encapsulated by nitrogen-doped few-layer graphene (NFG) for investigating the protection ability of the carbon shell. Transmission electron microscopy (TEM), X-ray diffraction (XRD), Raman spectroscopy, and X-ray photoelectron spectroscopy (XPS) measurements were applied to identify the structures, morphologies, and

characteristics of synthesized products. Besides, the oxidation protection performances of the carbon coating on Cu nanoparticles were then evaluated and compared with commercial Cu and as-made Cu from Cu electrode in the acid immersion tests.

2.2. Experimental procedure

2.2.1 Materials

Dimethylformamide (DMF, 99.5 %), acetone (> 99.5 %), 0.5 M sulfuric acid (H_2SO_4, 99.5 %), and nitric acid (HNO_3, 69.0 ~ 70.0 %) were purchased from Kanto Chemical Co., Inc., Japan. Commercial Cu nanoparticle powder (< 25 nm particle size), Cu standard solution (1000 $mg \cdot l^{-1}$), and PTFE filter membrane (JVWP04700, pore size 0.1 μm) were purchased from Sigma Aldrich, Germany. Cu electrodes (Cu, 99.9 %) 4.0 mm diameter were purchased from Nilaco Co., Japan.

2.2.2 Solution plasma (SP) synthesis

A 100 ml of DMF was poured into a glassy reactor attached with a pair of Cu electrodes shielded by insulator tubes. The Cu electrode tips were fixed at a gap of 0.5 mm. For plasma discharge, the Cu electrodes were connected with a bipolar-pulse power supply (Bipolar-DC pulsed power supply, Kurita Seisakusho Co., Ltd., Japan). The overall SP process setup was displayed in Figure 2.1 (a). The plasma was discharged in DMF solution for an hour with the fixed voltage and pulse width at 1000 V and 1 μs, respectively. The two types of Cu nanoparticle coated by NFG core-shell (Cu-NFG) products namely Cu-NFG-100 and Cu-NFG-200 were synthesized by different frequencies at 100 and 200 kHz, respectively. After the SP process, the solid residues were collected on a PTFE filter membrane and repeatedly washed with acetone using the filtration method. The residue powders were dried in an oven at 100 ºC for 12 h. After that, the obtained samples were weighted to determine the synthesis rate and then kept in dark bottles before further characterizations.

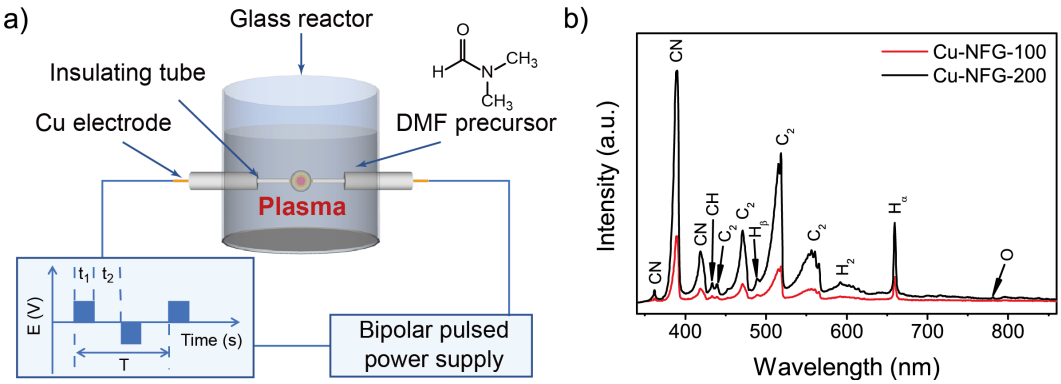

Figure 2.1 Schematic of solution plasma setup (a) and observed OES spectra during plasma discharge in DMF of Cu-NFG-100 and Cu-NFG-200 (b).

2.2.3 Characterizations

For detecting the generated radical species from SP in DMF, optical emission spectroscopy (OES, UV/Vis USB 2000+, Ocean Optics Inc., USA) was applied. The morphologies of the synthesized samples were observed by a transmission electron microscope (TEM, JEM-2500SE, JEOL Ltd., Japan) with the accelerating voltage apply at 200 kV. The crystallinity of the synthesized samples was confirmed and compared with a commercial Cu using X-ray diffraction (XRD, SmartLab, Rigaku Co., Japan) using Cu Kα radiation (λ = 0.154 nm). In order to analyze the carbon structure, Raman spectroscopy (Raman, Leica DM 2500M Ren (RL/TL) microscope, Renishaw Plc., England) was also applied using a laser-excitation wavelength of 532.5 nm. Mass compositions of the synthesized samples were also illustrated using thermal gravimetric analysis (TGA, TGA&DTG-60AH, Shimadzu Co., Japan) with a heating rate of 10 ºC/min in air. To analyze the chemical structure of the fabricated samples, X-ray photoelectron spectroscopy (XPS, PHI 5000 Versa Probe II, ULVAC-PHI, Inc., Japan) was applied using an Mg Kα X-ray source. Shirley background subtraction was used for deconvoluting the obtained XPS spectra in this research. For electrical resistivity measurement, the prepared samples were filled in a 0.3-cm-inner-diameter Teflon cylinder, and then it was compressed using brass pistons. The electrical resistivity was measured with compression at 0.6 MPa by a two-probe method using a Digital Multimeter CDM-2000D. The applied voltage and current of the plasma discharge were

measured by a digital oscilloscope (Yokogawa DLM2024-200MHz Mixed Signal Oscilloscope, Yokogawa Electric Co., Japan). The surface area and pore volume distribution results of the obtained samples were measured by the nitrogen adsorption-desorption method using the adsorption apparatus (BELSORP-mini II, BEL, Japan) at a temperature of –196 ºC.

2.2.4 Immersion test

The chemical oxidation resistance of the synthesized products was demonstrated by immersion test in an acidic medium. The immersion test will be conducted with two different types of strong acids including 1 N nitric acid and 1 N sulfuric acid solutions according to ISO 11130 with modification. The immersion in HNO_3 and H_2SO_4 occurred at room temperature of 25 ºC and temperature of 80 ºC, respectively. All measurements were carried out by immersing every 10 mg of samples in 165 ml acid solution. The solution was sampled at the immersion time of 1, 2, 4, 8, and 48 h. The Cu ion concentration, which was dissolved from the tested sample, in the collected solution was detected by inductively coupled plasma atomic emission spectroscopy (ICP-OES, SPS7800, Hitachi Corp., Japan). The mass loss and corrosion rate of the tested samples were calculated as equations below:

i) Mass loss:
$$m_{Cu,\,loss} = \frac{C_{Cu} \times V_{dd}}{1000}\ (g) \quad (1)$$

ii) Corrosion rate:
$$W = \frac{m_{Cu,\,loss}}{M \times m_{Cu} \times A \times t}\ (mol \cdot cm^{-2} \cdot h^{-1}) \quad (2)$$

where:

- C_{Cu} is the concentration of Cu ion in the obtained solution ($mg \cdot l^{-1}$),
- V_{dd} is the tested volume (l),
- M is the Cu molar mass ($g \cdot mol^{-1}$),
- m_{Cu} is the tested amount (g),
- A is the surface area of the tested sample ($cm^2 \cdot g^{-1}$),
- t is testing time (h).

In comparison, the purchased commercial Cu nanoparticles and Cu pieces cutting from Cu

electrodes by using a diamond file (Diamond thin hand form, # 150, Tsubosan file Co., Ltd., Japan) were also verified with the same testing procedure.

2.3. Results and discussion

2.3.1 Structural characterization

During the plasma discharge in the DMF solution, the reddish-grey particles were continuously produced between the Cu electrodes (Figure 2.2). The generated particles could be proposed as the combination of the carbon and Cu particles occurring through the carbonization process of the DMF precursor and the sputtering process of the Cu electrodes, respectively.[20, 21] The OES spectra were applied to observe the exciting radicals generated during the SP synthesis of the Cu-NFG-100 and Cu-NFG-200 samples. Figure 2.1 (b) presents that the C_2, CN, CH, O, and H species were produced in both conditions of the setup repetition frequencies at 100 and 200 kHz, due to the dissociation of the DMF precursor by SP.[22, 23] At higher repetition frequency, the higher intensities of the emission peaks of the generated radicals were monitored implying the higher generated species amounts from the SP process. Furthermore, the production rates at both synthesis conditions were also confirmed. As result, the higher repetition frequency gave a higher production rate which was around 15.8 $mg \cdot h^{-1}$ for the Cu-NFG-200 sample. Oppositely, the production rate in the synthesis of the Cu-NFG-100 sample indicated a low index at 5.2 $mg \cdot h^{-1}$. The higher amount of the obtained sample at the higher repetition frequency condition might be caused by the faster sputtering process occurring between the Cu electrodes leading to force the formation of Cu nanoparticles.[13]

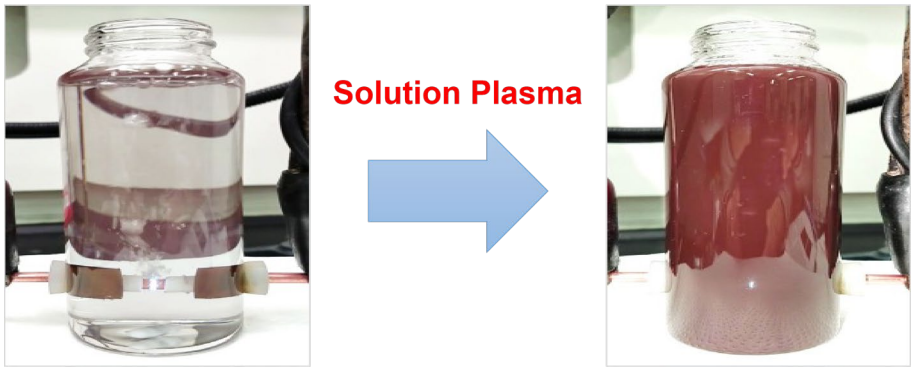

Figure 2.2 Solution plasma synthesis of Cu-NFG (initial and after 1 h of plasma discharge).

To understand the morphologies of the synthesized samples, the low- and high-resolution TEM were used in this research with the obtained results shown in Figure 2.3. In the TEM images, the existence of the black nanoparticles covered by the greyish edges was indicated as the Cu-cores and carbon-shells, respectively. The interplanar lattice space of black-cores was about 0.21 nm identifying the Cu nanoparticles structures.[24] As can be seen from the inserted graph in Figure 2.3 (a), the Cu-NFG-100 sample contained nanoparticles with the size varying from 5 nm to 11 nm and the average particle size of around 6.8 nm. Besides that, the high-resolution TEM photo in Figure 2.3 (b) illustrated that the carbon shells included from 3 to 5 layers, which were described as the proper layers of carbon coating that could progress the synergistic effect of protecting and improving the catalytic properties.[3, 25] A similar results were also observed from the TEM images of the Cu-NFG-200 sample, as displayed in Figure 2.3 (c, d). The Cu-NFG-200 sample indicated the nanoparticle structure with the size ranging from 5 to 17 nm and the average size at about 9.2 nm. As result, the increment of the operating repetition frequency enhances not only the synthesized amount but also the size of the generated samples.[26] Nevertheless, the few-layer of the carbon coatings (i.e., 1 to 3 layers), as well as some partially-covered cores, were illustrated in the Cu-NFG-200 sample referring to less amount of the synthesized carbon compared to that of the sample synthesized at repetition frequency at 100 kHz. Accordingly, the operating repetition frequency in the SP process could be adjusted for obtaining the various of the nanoparticle size as well as the number of carbon layers that suit with desired applications.

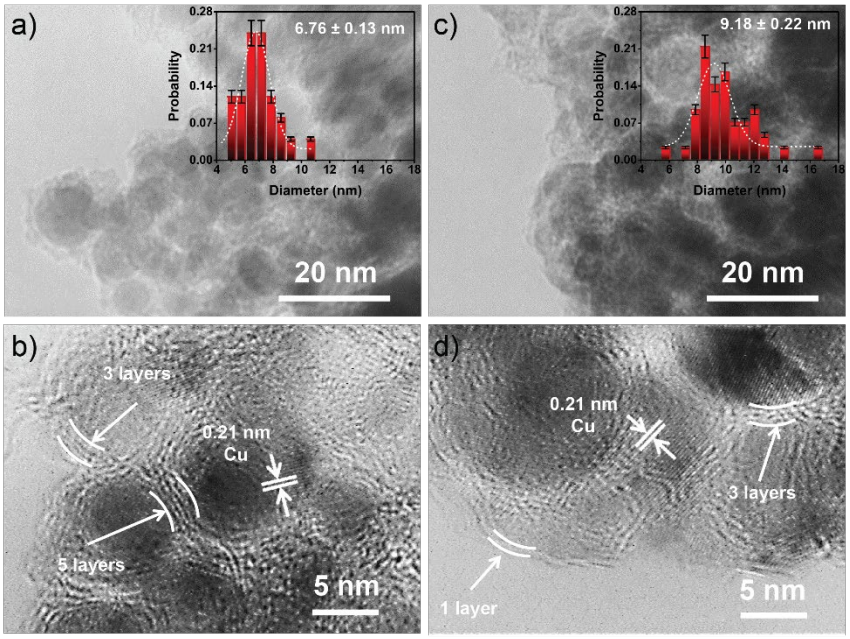

Figure 2.3 Low- and high-resolution TEM images of Cu-NFG-100 (a, b) and Cu-NFG-200 (c, d) samples.

The information of the sample structure was additionally investigated by the XRD measurement. Figure 2.4 (a) displays the XRD results taken from the Cu-NFG samples, which showed the strong peaks of the high crystallinity of the obtained Cu-core at 43.18º, 50.32º, and 74.04º, attributing to Cu 111, Cu 200, and Cu 220 planes, respectively.[27] It revealed that the major component in the synthesized cores is high crystallinity Cu metal. However, the XRD pattern of the Cu-NFG-200 sample also showed the small extra peaks at 35.48º, 38.83º, and 36.49º which corresponded to CuO 002, CuO 111, and Cu_2O 111, respectively.[28] The existence of these copper oxide peaks could refer to the oxidation process of the incomplete encapsulation of the Cu nanoparticles in the Cu-NFG-200 sample. The Cu oxide peaks were also observed from the XRD result of the commercial Cu (Figure 2.4 (b)). Additionally, the wide C 002 peaks at around 25º were also observed in both synthesized samples which were previously described to be the typical peak of graphene.[29]

Additionally, the Raman spectroscopy measurement was also applied to explore the structural information of the shell. The obtained spectra were presented in Figure 2.4 (c). The

Raman results of both synthesized samples showed off the typical G and 2D bands at 1580 cm^{-1} and 2680 cm^{-1}, respectively.[30] In general, the coexist of the G and 2D band in the Raman indicates the signature of the graphitic sp^2 structures.[31] Also, the D band at 1350 cm^{-1}, which commonly denotes the defects on carbon structure, was observed. The defects in carbon structure can be obtained due to the presence of vacancies, doping atoms, grain boundaries, or amorphous parts in carbon material.[32] Furthermore, the G+D band, which is located at around 2910 cm^{-1}, usually concerns the highly disordered carbon.[33] To identify the graphitization degree, the I_D/I_G ratio was evaluated from the obtained intensity values of the D and G band to reveal the perfection of the carbon structure.[34] The I_D/I_G ratios of the Cu-NFG-100 and Cu-NFG-200 samples were around 0.77 and 0.72, respectively. As result, the Cu-NFG-100 sample indicated more defect sites on the carbon coating compared to the Cu-NFG-200 sample. Besides, the degree of disorder of the coating could be further confirmed by the $I_D/(I_D+I_G)$ ratio and the width of the D band (W_D). The higher values of the $I_D/(I_D+I_G)$ ratio and W_D are the higher degrees of disorder. As result, the $I_D/(I_D+I_G)$ values at 0.436 and 0.420 and the W_D values at 90.01 and 87.62 cm^{-1} were represented to the Cu-NFG-100 and Cu-NFG-200 samples, respectively. The obtained values suggested the low disorder degree of the graphitic plane in the carbon shell.[35] The similar result was earlier informed the correlation between the higher input repetition frequency caused the more output energy, which causes a similar effect on carbonization, produced the ordered structure with low defects in the carbon structure.[36] Furthermore, the intensity ratio of the 2D and G bands and the full width at half maximum value of the 2D band ($FWHM_{2D}$) were also determined. The calculated I_{2D}/I_G ratios of the Cu-NFG-100 and Cu-NFG-200 samples were at 0.57 and 0.61, respectively. The $FWHM_{2D}$ values of the Cu-NFG-100 and Cu-NFG-200 samples were revealed at 89.5 cm^{-1} and 71.4 cm^{-1}. The obtained I_{2D}/I_G and $FWHM_{2D}$ values could confirm that the shell structures were few-layer graphene.[37, 38] The I_{2D}/I_G ratio and $FWHM_{2D}$ values of the Cu-NFG-100 sample inferred the higher number of carbon layers in the shell comparing to the Cu-NFG-200 sample.[38] Hence, the combination results from the TEM, XRD, and Raman measurements demonstrated that the Cu nanoparticles coated by a few-layer of graphene core-shell were successfully

synthesized using SP.

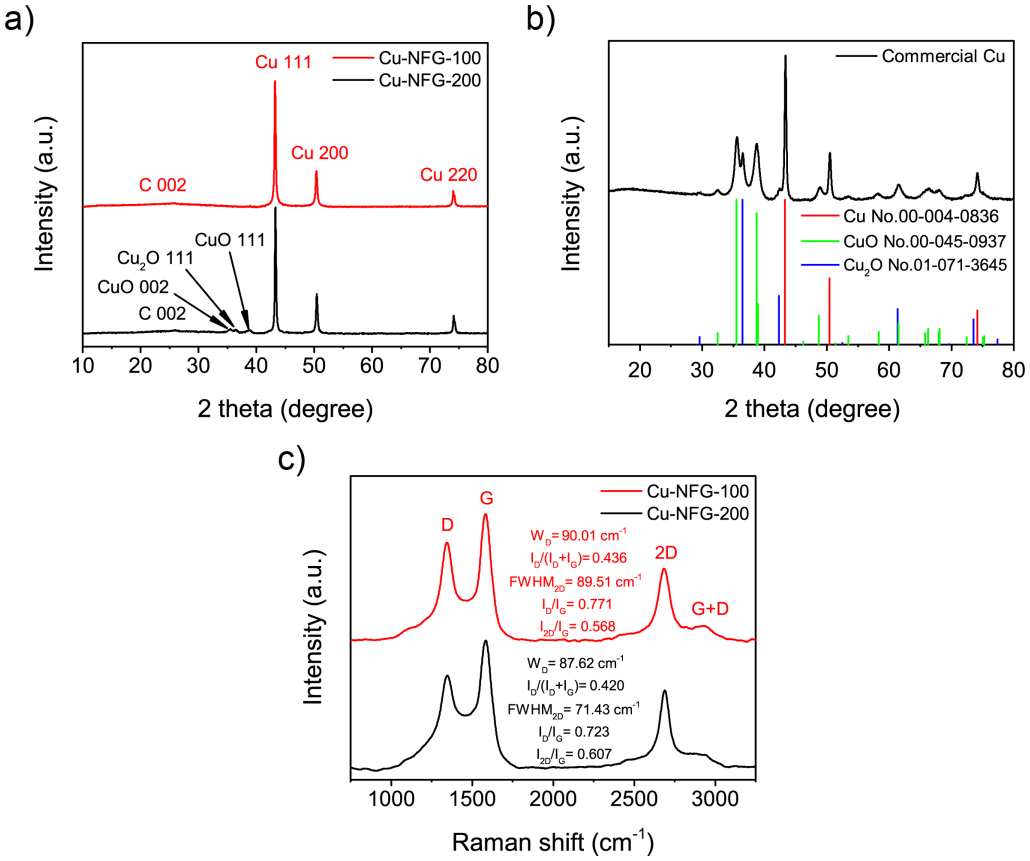

Figure 2.4 XRD patterns of synthesized samples (a) and commercial Cu (b). Raman spectra (c) of Cu-NFG-100 and Cu-NFG-200.

To confirm the comparison on the Cu amount in bulk samples, the TGA measurement was carried out by using TGA&DTG-60AH at a temperature of 30 ºC to 1000 ºC with a heating rate at 10 ºC·min^{-1} in air atmosphere. The percentage of the weight loss (%) and the DTA (mV·mg^{-1}) results of the Cu-NFG-100 and Cu-NFG-200 samples were present in Figure 2.5, respectively. The Cu-NFG-100 sample showed a mass loss of about 18 %, excluding moisture that was at around 100 ºC, representing a carbon composition on the shell. These mass losses were related to the decomposition processes of the labile oxygen-containing groups, the more stable nitrogen/oxygen, and the carbon-carbon bonding in the NFG structure at 382 ºC, 535 ºC, and 825 ºC, respectively.[39-42] The Cu-NFG-200 sample had a lower weight loss of about 10 %, meaning that the carbon part was less than the Cu-NFG-100 sample due to thinner layers of the

NFG on the Cu-core. The less amount of carbon on the Cu-NFG-200 sample might be explained by the rate of the sputtering from the Cu electrodes was much faster than the carbonization during the SP discharge due to higher energy at higher repetition frequency. Moreover, the Cu-NFG-200 sample showed an increase in mass in the TGA spectrum at around 393 ºC (Figure 2.5 (b)). The oxidation of the Cu nanoparticles with oxygen in the air can happen after some of the oxygen-containing carbon and amorphous carbon shell decomposed away, opening the new area that the Cu nanoparticles can expose to the air.[8] This confirms that the Cu-NFG-200 sample contained a smaller number of the NFG layers.

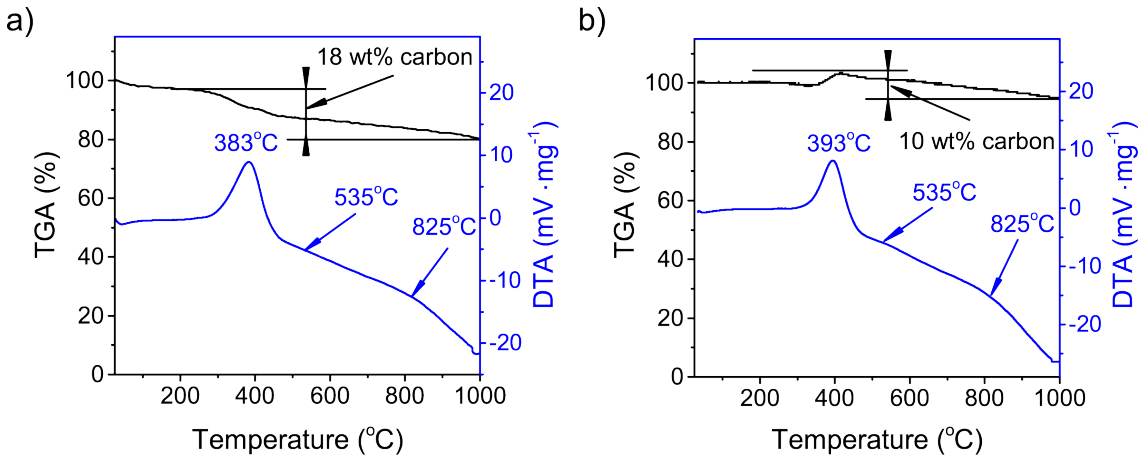

Figure 2.5 TGA and DTA results of Cu-NFG-100 (a) and Cu-NFG-200 (b).

The chemical compositions and bonding states of the fabricated samples were identified using the XPS measurement. As can be seen in Table 2.1, both of the Cu-NFG-100 and Cu-NFG-200 samples showed the presences of carbon together with the nitrogen and oxygen contents. The presence of nitrogen in both synthesized samples indicated that the NFG coating was successfully synthesized using the SP. Besides that, the Cu atomic composition in the Cu-NFG-100 sample was shown lower than that of the Cu-NFG-200 sample which was corresponded to the TGA result (Figure 2.5). To explore the chemical states of each element in the fabricated samples, the peak deconvolution was applied to the high-resolution XPS spectra with the results shown in Figure 2.6. As shown in Figure 2.6 (a, d), the C 1s spectra were deconvoluted into five peaks of the strong peak of C–C for the carbon sp^2 structures at

284.3 ± 0.1 eV following by the presences of C–N, C–O, C=O and O–C=O bonding peaks at 285.4 ± 0.2 eV, 285.8 ± 0.1 eV, 286.6 ± 0.2 eV and 289.2 ± 0.2 eV, respectively. The various carbon species displayed in the C 1s peak deconvolution implies that the graphene was functionalized.[43] Besides, the bonding states of the N 1s were deconvoluted into four subspecies including Pyridinic N, Pyrrolic N, Quaternary N, and Oxidized N peaks at 398.6 ± 0.2 eV, 399.5 ± 0.2 eV, 401.3 ± 0.2 eV, and 403.2 ± 0.2 eV, respectively (Figure 2.6 (b, e)). The Pyridinic N, Pyrrolic N, and Oxidized N species were typically denoted to the nitrogen-doped at the edge of graphene, while the Quaternary N specie is a substituent of the nitrogen atoms in the graphene frameworks.[44] However, both of the synthesized samples indicated the presences of the Pyrrolic N, Pyridinic N, and Quaternary N which confirmed the obtained nitrogen-doped carbon by using the SP process. Due to the various nitrogen doping types occurred in the synthesized samples, various catalytic performance for electrochemical reactions could be achieved.[45] According to Figure 2.6 (c, f), the high-resolution Cu $2p_{3/2}$ peak were combined of the Cu(0) at 932.7 ± 0.1 eV and Cu(II) at 934.6 ± 0.1 eV states.[46] The ratios of Cu(II)/Cu(0) were calculated to identify the Cu oxides in the fabricated samples. As result, the Cu-NFG-200 sample with the higher value of Cu(II)/Cu(0) ratio at 0.174 indicated the more oxidized Cu-core content compared to that of the Cu-NFG-100 sample which showed the lower Cu(II)/Cu(0) ratio at 0.088. The higher Cu oxides existences in the Cu-NFG-200 sample were in good agreement with the XRD results. Furthermore, the electrical resistivities of the Cu-NFG-100 and Cu-NFG-200 samples were found to be 1.72 Ω·cm and 1.37 Ω·cm, respectively which were measured by the 2-probe method. The higher resistivity of the sample synthesized at the repetition frequency of 100 kHz might be affected by a thicker shell comparing with the Cu-NFG-200 sample. According to the previous study, the thickness of the NFG was found to be an inversely proportional resistivity because electrons can not easily flow through between graphene planes.[47]

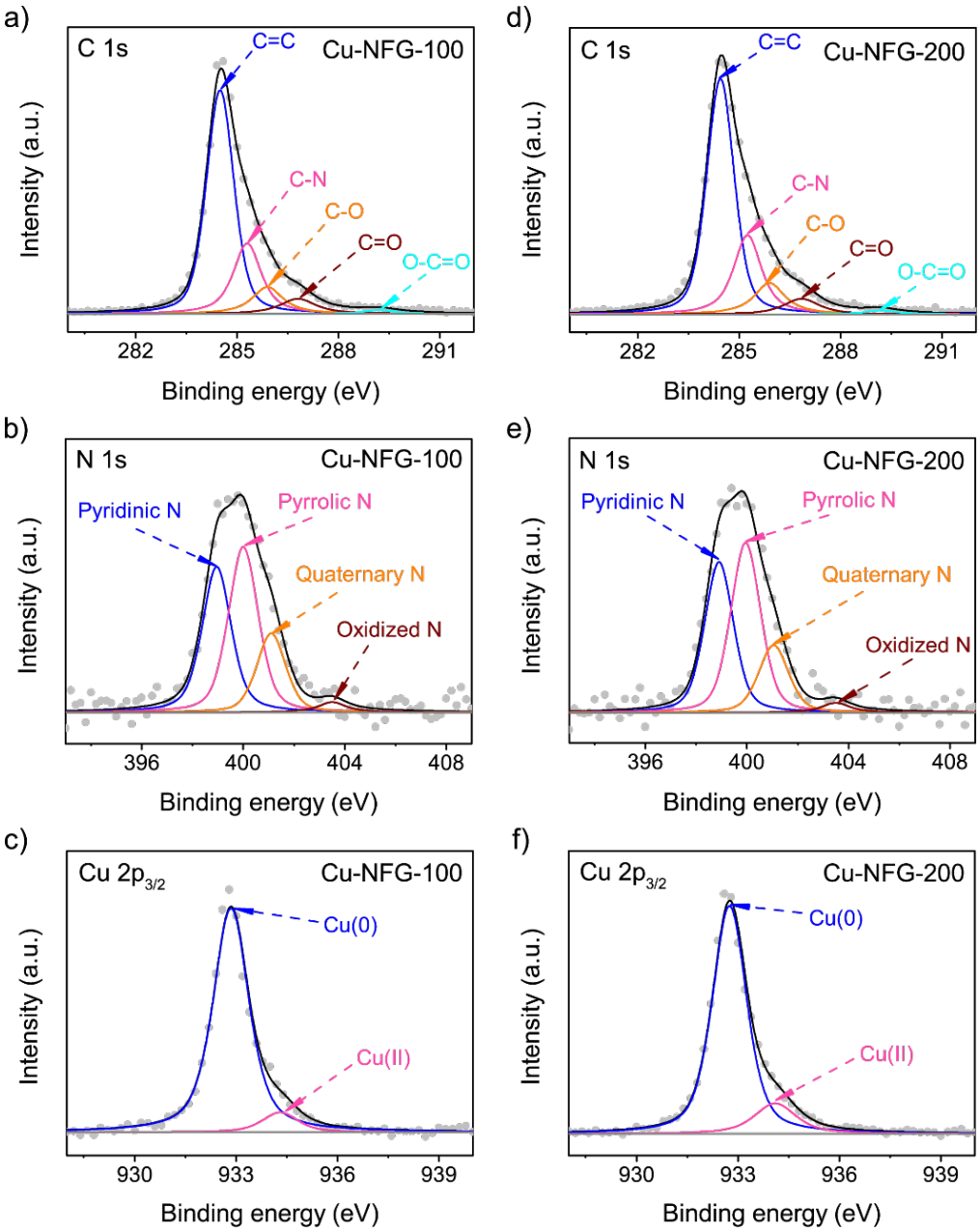

Figure 2.6 High-resolution XPS spectra of C 1s (a, d), N 1s (b, e), and Cu $2p_{3/2}$ (c, f) from Cu-NFG-100 and Cu-NFG-200, respectively.

Table 2.1 The surface elemental composition data from XPS measurements of Cu-NFG-100 and Cu-NFG-200.

Sample	C (at%)	N (at%)	O (at%)	Cu (at%)	N/C	O/C	Cu/C
Cu-NFG-100	90.94	3.93	4.53	0.60	0.04	0.05	0.01
Cu-NFG-200	90.24	3.73	3.36	2.68	0.04	0.04	0.03

2.3.2 Proposed mechanism of solution plasma synthesis of Cu-NFG

The formation mechanism of the SP synthesis of the core-shell nanospheres at the different setup repetition frequencies was introduced in this report. Based on the gained pieces of evidence, the core-shell nanostructures of the Cu nanoparticles covered by the NFG coating were produced by the two main reactions of the carbonization and sputtering processes. During the SP discharged between the tips of the Cu electrodes, the carbonization process forms the carbon materials for the shells and the plasma sputtering generated Cu atoms for the cores. In detailed of the carbonization process, the DMF molecules were firstly decomposed to form the active radicals and fragments where the temperature values of the plasma zones were at around 3700 K. Later, those fabricated fragments were grown to form the carbon framework. However, the developments of the carbon structures were quenched once they left the plasma zone to the surrounding solution where the temperature was extremely lower. In the earlier reports, it was discovered that the formation of the carbon in aromatic compounds, such as benzene, was quickly achieved due to the existence of π electrons delocalization.[19, 48-50] During the plasma discharge, the active radicals were continuously generated from the decomposition process of the organic molecules and then reacted with the neighbouring molecules to execute the polymerization process for obtaining the widespread carbon framework.[51] Conversely, the DMF precursor is an aliphatic compound without the delocalization system leading to the relatively low rate of carbon formation compared to that of the aromatic precursors. Additionally, nitrogen and oxygen atoms

in the DMF molecules could cause terminating sites and limit further carbon growth process.[23] In the case of the metal-core formations, the Cu-cores could be fabricated from the sputtering process occurred at the tips of the Cu electrodes during the SP. The metal atoms at the surface of the electrodes were bombarded and then knocked off by the energized electrons, ions, and atoms in the plasma zone during the discharge.[52] The ejected metal atoms could lead to the nucleation following with the crystal growth to form the larger cluster and nanoparticle. Instantaneously, the growth of the metal crystal has also collaborated with the formation of graphene. The metal surface acts as the substrate for adsorbing of the pre-formed single carbon layer.[53] In the beginning, the coating should contain an amorphous carbon due to the stochastic collisions of the generated radicals.[54] Nevertheless, the extremely high temperature at the plasma zone and plasma interfaces could graphitize those pre-formed carbons to form an ordered crystalline layer of graphene on the metal surface,[55] resulting in the Cu-carbon composite nano-aggregates. In the plasma zone, those aggregates coalesced each other to grow the Cu-core under high temperature. While there was the prompt carbon interdiffusion out of the nano-aggregates due to the limit of the carbon solubility in the Cu nanoparticles left the high crystallinity of the fabricated Cu-core.[56] This was agreeing to the TEM images (Figure 2.3) where the clear and uniform crystal plane of the Cu-cores can be observed. The growth of the carbon to form the multiple layers of the NFG coating might be the carbonization process of the pre-formed amorphous phase, which was first made due to the stochastic collisions of the generated radicals. After that, those amorphous carbons can graphitize to convert an ordered crystalline of the NFG coating on the Cu-core caused by the tremendously high temperature in the plasma zone.[55] Finally, the fabricated products were diffused across the plasma interface to the DMF solution, which has a much lower temperature, leading to the sudden termination of further reactions. As result, the thermodynamically metastable of the Cu-NFG core-shell nanoparticles could be formed via SP in which the conventional techniques are incapable to achieve.[15] Figure 2.7 demonstrates the synthesis pathway of the Cu-NFG core-shell structure by using the SP process. Additionally, as presented results from this report, the controllable thickness of the NFG-shell coated on the Cu-core was

also achieved via the adjusting setup repetition frequency from the plasma discharge.

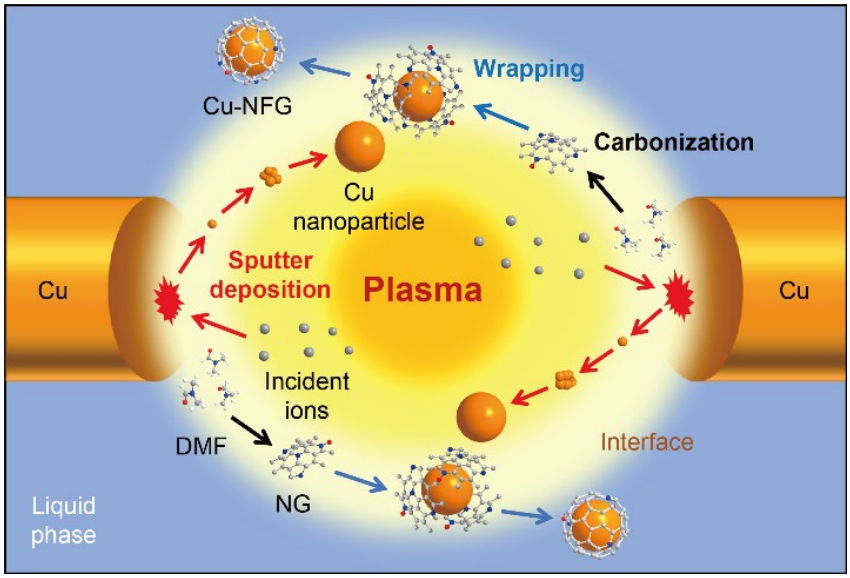

Figure 2.7 Illustration synthesis pathway of Cu-NFG core-shell structure via SP.

The observed current-voltage waveforms at the setup repetition frequency of 100 kHz and 200 kHz are presented in Figure 2.8. The input energy per pulse (E_p) supplied from the plasma discharge can be estimated by integrating the input power (voltage times ampere) in a pulse, while the energy per time (E_t) is determined by multiplying the energy per pulse with the input repetition frequency as follow $E_p = \int (V_t \times I_t) dt$ and $E_t = f \times E_p$ where V_t and I_t are the applied voltage and ampere at any t while f is the setup repetition frequency of the plasma discharge. When the input repetition frequency is doubled, the pulse number is also doubled, however, the energy strike per pulse is nearly unchanged due to the similar input current and voltage parameters produced from the power supply. As result, the increase of the setup repetition frequency leads to the unchanged energy per pulse but boosts the amount of the energy per time. The higher input striking number leads to enhance the synthesis rate via the SP process. Besides that, the higher number of striking to the metal electrode at 200 kHz produces more Cu atoms sputtering from the Cu electrodes delivering the bigger size of the synthesized nanoparticles which was in good agreement with the TEM in Figure 2.3. Besides, the number of the carbon coating was found to be one to three NG layers in the Cu-NFG-200 sample which was the thinner coating compared to the Cu-NFG-100

sample (three to five NG layers). As revealed, the increasing of the input repetition frequency increased the radicals formations, however, the similar input energy per pulse led to the similarly generated radical types from the DMF precursor during the SP process (Figure 2.1 (b)). Besides that our XPS results in Table 2.1 also demonstrated the matching composition of the NFG shells in both synthesized samples. Although, the faster synthesis rate of the carbon formation can be achieved with the repetition frequently at 200 kHz. However, it seemed the sputtering rate of the synthesis of the Cu-core was boosted faster than the increase of the carbonation rate of the NFG formation at the higher frequency. Therefore, the layer numbers of the NFG shells coated on the Cu-cores were negatively affected by the increase of the input repetition frequency. In this research, it was different from the synthesis process of decorating the metal nanoparticles on the carbon support as described in previous reports.[19, 48-50] Those used various aromatic precursors to produce the nanocarbon extremely more rapidly compared to the formation rate of the metal nanoparticles during the SP. As result, the small number of the metal nanoparticles displayed on the synthesized carbon nanosphere.

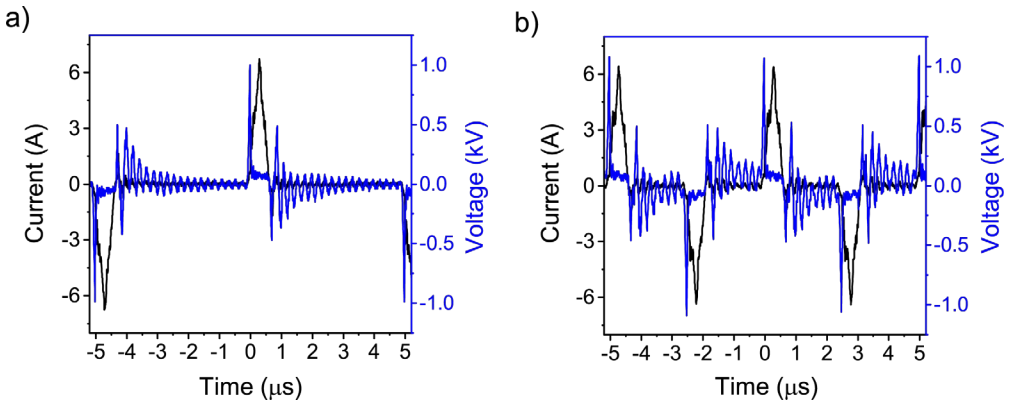

Figure 2.8 Current and voltage waveforms during plasma discharge in DMF at repetition frequencies of 100 kHz (a) and 200 kHz (b).

2.3.3 Acid resistance ability of the Cu-NFG core-shell

The protection ability of the NFG coatings to the Cu-cores in the synthesized samples were investigated by the immersion method using the two testing conditions of the HNO_3 and H_2SO_4 solutions. Normally, Cu atoms rapidly react with nitrate ions via the redox reaction process

because the E^0 of NO_3^-/NO (E^0 = +0.96 V (V vs. SHE)) is more favourable than of Cu^{2+}/Cu (E^0 = +0.34 V (V vs. SHE)). Then, the Cu metal could be oxidized to form the Cu ion when it was immersed in the nitric acid solution. So, the immersion test conditions were first arranged with the strong acid of 1 N HNO_3 at 25 ºC. The dissolved Cu ions amount from the tested samples diffused to the acid solutions was illustrated using the ICP-OES measurement as shown in Figure 2.9 (a). After 1 h of testing, the solution collected from the immersion test of the commercial Cu nanoparticles indicated the high concentration of the Cu ions at about 59.2 mg·l^{-1}. After that, the nearly unchanged values of the Cu ion concentrations were detected from the collected solutions after 2 and 4 h immersion. Based on these results, all commercial Cu nanoparticles had been dissolved into the acid solution which indicated the rapid corrosion process has occurred on the uncoated Cu nanoparticles. Besides, the uncoated sample indicated the rapid corrosion process related to the high contact area for interface reaction at a nano size. In the meantime, the Cu particles from the Cu electrode shown the increase of the Cu ion during the measurement which indicated the highest value at 64.8 mg·l^{-1} after 48 h of the immersion. Based on the results, the uncoated Cu sample represents very poor corrosion resistance ability. For the coated sample, the different pattern of the result showed in Figure 2.9 (a). The Cu-NFG-200 sample indicated the low concentration at 3.4 mg·l^{-1} after 1 h immersion and then gradually increased to the highest value at 6.9 mg·l^{-1} after the immersion test in the nitric solution for 48 h. Especially, the Cu-NFG-100 sample showed the lowest value of the Cu ion in the collected solution compared to the other samples in all the time. The highest Cu ions concentration from the immersion test of the Cu-NFG-100 sample was only shown at 2.8 mg·l^{-1} after 48 h immersion. Furthermore, the coated samples also indicated similar results when they were tested in the sulfuric acid solution at a high temperature. The slight reduction of the Cu-ion in the case of the immersion test in the sulfuric acid solution is related to the presence of the incompletely oxidized of the uncoated nanoparticles in the sample. During the immersion, the outer oxidized parts can be removed easily by reaction with the proton in the sulfuric acid solution, however, the unoxidized Cu cores will not be oxidized by the proton in the acid solution due to its higher redox

potential. The high amount of the Cu ion collected from the Cu-NFG-200 sample indicated the presence of the higher Cu oxide amount which corresponded to the XRD results (Figure 2.4 (a)) that confirmed the imperfect coating that the peak of the Cu oxides can be observed on the Cu-NFG-200 sample. The low Cu ion concentration in the collected solution related to the small Cu nanoparticle was diluted during the immersion test. With the extremely low Cu ion concentration values from the immersion tests, both synthesized samples demonstrated that the Cu-cores were successfully protected by the NFG shells. Therefore, it could be proposed that the several layers of the NG successfully indicated its significant function in protecting the Cu-core and the modification of the number layer of the NFG coating plays as a key for boosting the stability of the catalysts in future applications. Normally, the reaction rate depends on the contact area related to the surface area of the tested samples in the immersion test. For a reasonable comparison, the corrosion rates were calculated by the ratio of the diluted amount with the surface area of the tested sample. The surface area will be measured for the coated sample using the N_2 adsorption-desorption isotherm method at –196 ºC. As can be seen in Figure 2.10, the Cu-NFG-100 and Cu-NFG-200 samples indicated a similar surface area at 71.73 and 75.36 $m^2 \cdot g^{-1}$, respectively. The corrosion rate data were displayed in Table 2.2. At first, the Cu-NFG-200 sample exhibited a quite high rate of the corrosion process compared to that of the Cu-NFG-100 sample, which might be related to the corrosion on the incompletely covered part in the synthesized samples. After that, the corrosion rate of both synthesized samples illustrated the very low values at 48 h immersion. However, the Cu-NFG-200 sample indicated the higher corrosion rates which were about 2 to 5 times in the nitric acid immersion test and about 13 to 28 times in the sulfuric acid immersion test compared to that of the Cu-NFG-100 sample. The difference in the obtained corrosion rates in the synthesized samples can be justified for the efficiency from the protective coating of the NFG shell. In the case of the Cu-NFG-100 sample, the thicker carbon coating of 3 to 5 NG layers offered the better protection ability compared to the Cu-NFG-200 sample which indicated the thinner coating of 1 to 3 NG layers as well as the imperfect coating (Figure 2.3). Furthermore, the XRD analyst was also applied to the immersed

samples to examine the changed in their structures after the corrosion processes with the results as shown in Figure 2.9 (b). It can be seen that the Cu-NFG-200 sample indicated the change in the structures before and after the immersion test with HNO_3 and H_2SO_4 solution. Oppositely, the Cu-NFG-100 sample could maintain its structure after immersion tests. Accordingly to all obtained results, the synthesized NFG-shell shows its high ability to protect the Cu-core from the acid-corrosion in strong oxidation acidic conditions.

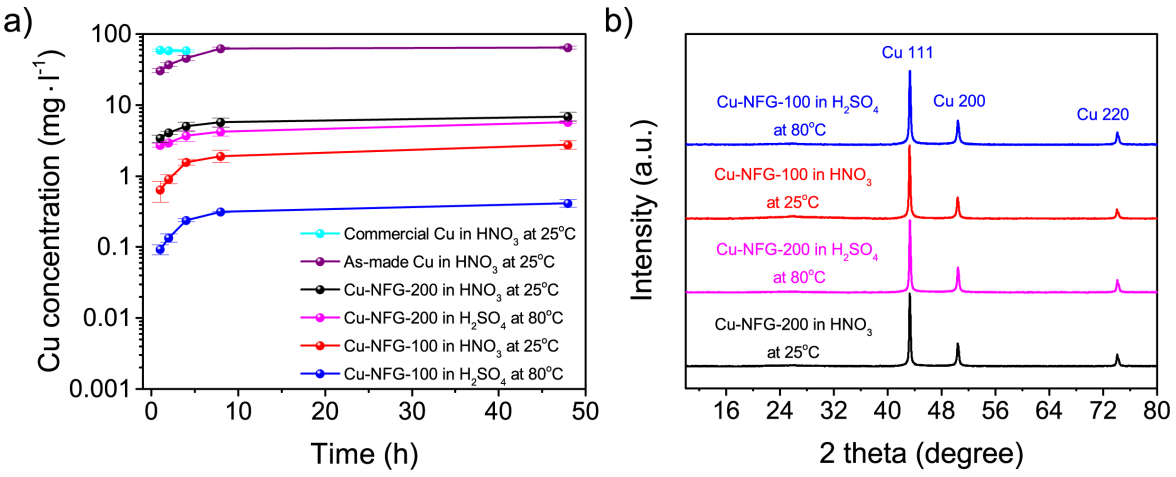

Figure 2.9 ICP-OES of Cu ion concentration in the collected solution (a) and XRD of solid residues (b) results of the tested samples from the immersion tests in acid.

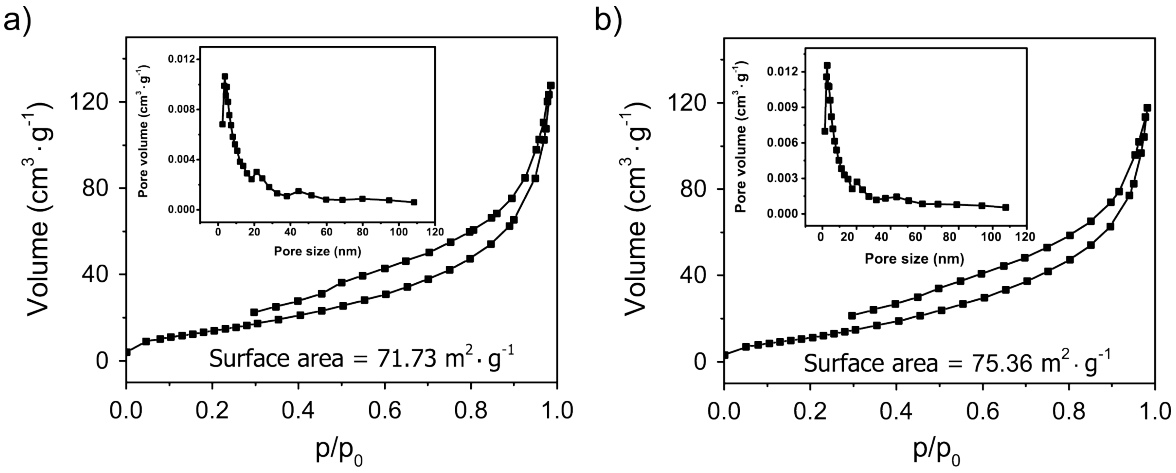

Figure 2.10 Nitrogen adsorption-desorption isotherm at –196 ºC, Brunauer-Emmett-Teller surface area, and pore volume distribution results of Cu-NFG-100 (a) and Cu NFG 200 (b).

Table 2.2 Calculated corrosion rates of Cu-NFG-100 and Cu-NFG-200 in 1 N HNO_3 at 25 °C and in 1 N H_2SO_4 at 80 °C.

Corrosion time (h)	**The corrosion rate in HNO_3 ($x10^{-12}$ mol·cm^{-2}·h^{-1})**		**The corrosion rate in H_2SO_4 ($x10^{-12}$ mol·cm^{-2}·h^{-1})**	
	$W_{Cu\text{-}NFG\text{-}100}$	$W_{Cu\text{-}NFG\text{-}200}$	$W_{Cu\text{-}NFG\text{-}100}$	$W_{Cu\text{-}NFG\text{-}200}$
1	2.308	11.721	0.334	9.377
2	1.642	6.982	0.244	5.051
4	1.418	4.328	0.217	3.175
8	0.867	2.461	0.141	1.822
48	0.208	0.495	0.031	0.414

2.4. Summary

The Cu nanoparticles encapsulated with the NFG coating was successfully synthesized in one pot via the SP process under room temperature and pressure condition. The number layer of the NFG could be tuned by adjusting the input repetition frequency to achieve the appropriate number of carbon layers, which could result in the outstanding stability of the obtained product in acid mediums. Moreover, not only the structure but also the functionalization, such as doping of N atoms onto the graphene structure, can be adjusted based on the various types of carbon precursors and metal electrodes. This leads to the performance improvement of the obtained materials to suit the desired applications, for instance, to be a durable electrocatalyst for a metal-air electrochemical cell, thermally conductive adhesives, and a conductive printing. Accordingly, the SP method showed ability as the promising tool that can explore the new opportunity, aiming to achieve the tunable synthesis of not the only core-shell structure but also other advanced materials, that can meet economic feasibility and environmental concerns.

References

1. S. K. Tiwari, S. Sahoo, N. Wang and A. Huczko, *J. Sci. Adv. Mater. Devices*, 2020, **5**, 10-29.
2. D. Selvakumar, H. Sivaram, A. Alsalme, A. Alghamdi and R. Jayavel, *J. Mater. Sci.: Mater. Electron*, 2016, **27**, 6232-6241.
3. S. Wang, X. Huang, Y. He, H. Huang, Y. Wu, L. Hou, X. Liu, T. Yang, J. Zou and B. Huang, *Carbon*, 2012, **50**, 2119-2125.
4. M. Topsakal, H. Şahin and S. Ciraci, *Phys. Rev. B*, 2012, **85**, 155445.
5. G. Panomsuwan, N. Saito and T. Ishizaki, *Phys. Chem. Chem. Phys.*, 2015, **17**, 6227-6232.
6. R. Yadav and C. Dixit, *Journal of Science: Advanced Materials and Devices*, 2017, **2**, 141-149.
7. J.-H. Lee, E.-K. Lee, S.-G. Kang, S.-H. Jung, S.-K. Son, W. H. Nam, T.-H. Kim, B. L. Choi and D. Whang, *Appl. Surf. Sci.*, 2018, **440**, 553-559.
8. S. Chen, A. Zehri, Q. Wang, G. Yuan, X. Liu, N. Wang and J. Liu, *ChemistryOpen*, 2019, **8**, 58-63.
9. C. An, P. Ding, B. Ye, X. Geng and J. Wang, *AIP Adv.*, 2017, **7**, 035324.
10. J. Li and C.-y. Liu, *New J. Chem.*, 2009, **33**, 1474-1477.
11. J. Zhang, X. Hu, B. Yang, N. Su, H. Huang, J. Cheng, H. Yang and N. Saito, *J. Alloys Compd.*, 2017, **709**, 588-595.
12. T. Sudare, T. Ueno, A. Watthanaphanit and N. Saito, *J. Surf. Finish. Soc. Jpn.*, 2016, **67**, 46-50.
13. P. Pootawang, N. Saito and S. Y. Lee, *Nanotechnology*, 2013, **24**, 055604.
14. S. Chae, G. Panomsuwan, M. A. Bratescu, K. Teshima and N. Saito, *ACS Appl. Nano Mater.*, 2019, **2**, 1350-1355.
15. K. Hyun and N. Saito, *Sci. Rep.*, 2017, **7**, 3825.
16. S. Lee, Y. Heo, M. A. Bratescu, T. Ueno and N. Saito, *Phys. Chem. Chem. Phys.*, 2017, **19**, 15264-15272.

17. J. Kang, Y. Kim, H.-m. Kim, X. Hu, N. Saito, J.-H. Choi and M.-H. Lee, *Sci. Rep.*, 2016, **6**, 38652.
18. D.-w. Kim, O. L. Li, P. Pootawang and N. Saito, *RSC Adv.*, 2014, **4**, 16813-16819.
19. J. Kang and N. Saito, *RSC Adv.*, 2015, **5**, 29131-29134.
20. M. A. Bratescu, O. Takai and N. Saito, *J. Alloys Compd.*, 2013, **562**, 74-83.
21. C. Chokradjaroen, S. Kato, K. Fujiwara, H. Watanabe, T. Ishii and T. Ishizaki, *Sustain. Energy Fuels*, 2020, 4570-4580.
22. O. L. Li, S. Chiba, Y. Wada, G. Panomsuwan and T. Ishizaki, *J. Mater. Chem. A*, 2017, **5**, 2073-2082.
23. K. Kim, K. Hashimi, M. A. Bratescu and N. Saito, *Nanosci. Nanotechnol. Lett.*, 2018, **10**, 814-819.
24. Z. Zhang, Y. Ji, J. Li, Z. Zhong and F. Su, *RSC Adv.*, 2015, **5**, 54364-54371.
25. H. Wu, T. Peng, Z. Kou, J. Zhang, K. Cheng, D. He, M. Pan and S. Mu, *Chinese J. Catal.*, 2015, **36**, 490-495.
26. D. M. McClenathan, W. C. Wetzel, S. E. Lorge and G. M. Hieftje, *J. Anal. At. Spectrom.*, 2006, **21**, 160-167.
27. L. Hang, Y. Zhao, H. Zhang, G. Liu, W. Cai, Y. Li and L. Qu, *Acta Mater.*, 2016, **105**, 59-67.
28. S. Pourbeyram, J. Abdollahpour and M. Soltanpour, *Mater. Sci. Eng., C*, 2019, **94**, 850-857.
29. Z.-L. Cheng and X.-X. Qin, *Chin. Chem. Lett.*, 2014, **25**, 1305-1307.
30. J.-B. Wu, M.-L. Lin, X. Cong, H.-N. Liu and P.-H. Tan, *Chem. Soc. Rev.*, 2018, **47**, 1822-1873.
31. S. Samanta, S. Singh and R. R. Sahoo, *RSC Adv.*, 2015, **5**, 61888-61899.
32. A. Yadegari, L. Samiee, S. Tasharrofi, S. Tajik, A. Rashidi, F. Shoghi, M. Rasoulianboroujeni, M. Tahriri, S. J. Rowley-Neale and C. E. Banks, *RSC Adv.*, 2017, **7**, 55555-55566.
33. L. Bokobza, J.-L. Bruneel and M. Couzi, *C*, 2015, **1**, 77-94.
34. M. Mowry, D. Palaniuk, C. C. Luhrs and S. Osswald, *RSC Adv.*, 2013, **3**, 21763-21775.

35. A. Cuesta, P. Dhamelincourt, J. Laureyns, A. Martinez-Alonso and J. D. Tascón, *Carbon*, 1994, **32**, 1523-1532.
36. K. Hyun, T. Ueno and N. Saito, *Jpn. J. Appl. Phys.*, 2015, **55**, 01AE18.
37. J.-S. Hwang, Y.-H. Lin, J.-Y. Hwang, R. Chang, S. Chattopadhyay, C.-J. Chen, P. Chen, H.-P. Chiang, T.-R. Tsai and L.-C. Chen, *Nanotechnology*, 2012, **24**, 015702.
38. A. C. Ferrari, J. Meyer, V. Scardaci, C. Casiraghi, M. Lazzeri, F. Mauri, S. Piscanec, D. Jiang, K. Novoselov and S. Roth, *Phys. Rev. Lett.*, 2006, **97**, 187401.
39. J. Qin, Y. Zhang, S. E. Lowe, L. Jiang, H. Y. Ling, G. Shi, P. Liu, S. Zhang, Y. L. Zhong and H. Zhao, *J. Mater. Chem. A*, 2019, **7**, 9646-9655.
40. M. Barrejón, A. Primo, M. J. Gómez-Escalonilla, J. L. G. Fierro, H. García and F. Langa, *Chem. Commun.*, 2015, **51**, 16916-16919.
41. A. Gupta, R. Jamatia, R. A. Patil, Y.-R. Ma and A. K. Pal, *ACS omega*, 2018, **3**, 7288-7299.
42. S. N. Alam and L. Kumar, *Materials Science and Engineering: A*, 2016, **667**, 16-32.
43. N. Thongwichit, O. L. H. Li, W. Yaowarat, N. Saito and U. Suriyapraphadilok, *Jpn. J. Appl. Phys.*, 2015, **55**, 01AE10.
44. D.-w. Kim, O. L. Li and N. Saito, *Phys. Chem. Chem. Phys.*, 2014, **16**, 14905-14911.
45. D. Guo, R. Shibuya, C. Akiba, S. Saji, T. Kondo and J. Nakamura, *Science*, 2016, **351**, 361-365.
46. F. Liu, L. Csetenyi and G. M. Gadd, *Appl. Microbiol. Biotechnol.*, 2019, **103**, 7217-7230.
47. X.-Y. Fang, X.-X. Yu, H.-M. Zheng, H.-B. Jin, L. Wang and M.-S. Cao, *Physics Letters A*, 2015, **379**, 2245-2251.
48. J. Kang, Y. Kim, H. M. Kim, X. Hu, N. Saito, J. H. Choi and M. H. Lee, *Sci. Rep.*, 2016, **6**, 38652.
49. J. Kang, O. L. Li and N. Saito, *Nanoscale*, 2013, **5**, 6874-6882.
50. D.-w. Kim, O. L. Li, P. Pootawang and N. Saito, *RSC Adv.*, 2014, **4**.
51. T. Morishita, T. Ueno, G. Panomsuwan, J. Hieda, A. Yoshida, M. A. Bratescu and N. Saito, *Sci. Rep.*, 2016, **6**, 36880.

52. F. Yu, M. Liu, C. Ma, L. Di, B. Dai and L. Zhang, *Nanomaterials*, 2019, **9**, 1436.

53. Y. Dedkov and E. Voloshina, *J Phys Condens Matter*, 2015, **27**, 303002.

54. C. O. Reinhold, P. S. Krstic and S. Stuart, *Nucl. Instrum. Methods Phys. Res., B*, 2009, **267**, 691-694.

55. M. A. Pimenta, G. Dresselhaus, M. S. Dresselhaus, L. G. Cancado, A. Jorio and R. Saito, *Phys. Chem. Chem. Phys.*, 2007, **9**, 1276-1291.

56. G. A. López and E. J. Mittemeijer, *Scripta Mater.*, 2004, **51**, 1-5.

Chapter 3

Oxygen Reduction Reaction Catalytic Performance of Pt Nanoparticles Coated by Nitrogen-Doped Few-Layer Graphene Synthesized by Solution Plasma Method

Chapter 3 - Oxygen Reduction Reaction Catalytic Performance of Pt Nanoparticles Coated by Nitrogen-Doped Few-Layer Graphene Synthesized by Solution Plasma Method

3.1. Introduction

The electrochemical energy storage and conversion systems such as fuel cell, rechargeable battery, and supercapacitor have been focusing on being alternatives to fossil fuels for a future "green" society. The proton exchange membrane fuel cells (PEMFCs) have been accounted for as the highly efficient power generators for sustainable energy without any pollution emission.[1] One of the essential keys in the fuel cell industry is a catalyst for oxygen reduction reaction (ORR), which was conventionally using a platinum (Pt)-based carbon. Pt-based carbon catalyst is the efficient and well-known electrochemical catalyst due to its low overpotential and fast kinetics for the ORR. However, the Pt-based carbon catalyst has been pointed out to be an unsuitable one for practical purposes because of its high-cost, low durability, and weak toxicity tolerance as well as it causes carbon corrosion.[2-4] One of the challenges to science is essential for finding a suitable material which has the highly ORR properties of long lifetime operation at the demand-working condition of the PEMFC.[5]

Later, heteroatoms-doped graphene has been discovered to be an alternative to the Pt-based carbon catalyst because of its high chemical resistance and modifiable properties.[6] Recently, various heteroatoms, such as nitrogen (N), boron (B), iodine (I), and sulfur (S), have been studied and presented the formation of the active sites for the optimal working catalysts for the ORR.[7-10] Notably, a nitrogen atom, which is a carbon-similar-sized atom and available to create strong bondings with carbon atoms, was selected to be an efficient dopant for tailoring the graphene catalyst to improve the ORR performance for applying to the fuel cell.[11] However, it has some limitations to those small active sites and the low nitrogen-doped contents. It demonstrated the

unsatisfying in the electrocatalytic properties.[12] Combining the nitrogen-doped graphene (NG) with the Pt nanoparticles have been illustrated as a good strategy for improving the ORR performance in the PEMFC due to the formation of stronger electronic interaction between nitrogen from graphene to Pt.[13-15] However, such a composite material still has some drawbacks in terms of the low poisoning tolerance from Pt nanoparticles as well as the easy corrosion and degradation of the carbon support material due to the effect of Pt which can cause a reduction of performance and stability of the catalyst for practical uses. Thus, a new design of the metal nanoparticles encapsulated by the controllable thickness of nitrogen-doped few-layer graphene (NFG) materials were then introduced in a model of the core-shell structure for future research.

The Pt nanoparticles coated by nitrogen-doped carbon core-shell materials have been focusing on their ORR performance and gained good results in enhancing the durability and catalytic performance comparing to that of commercial Pt/C.[16, 17] Nevertheless, the protection ability and catalytic ability effected by the NFG-shell has not been targeted. From this point, it is crucial to find a way that can fabricate and engineer a thickness of the NFG-shell on the Pt-core. In the past years, a chemical vapor deposition (CVD) has been applied as a favoured method to introduce the carbon to the surface of the metal with high quality. For instance, a one-step synthesis of germanium (Ge) coated by graphene using the CVD method at 900 ºC under argon atmosphere was reported by Lee *et. al.*.[18] As one of the developed in the CVD methods, a cold wall reactor has been successfully used to prepare the core-shell structure of copper (Cu) nanoparticles encapsulated by graphene at a lower temperature of 775 ºC at 0.1 mbar pressure by Chen *et. al*.[19] Although the CVD method showed an excellent performance to fabricate the metal-carbon core-shell, it requires a large amount of inert gas causing the high cost of the products. Besides that, a more facile method namely detonation was progressed by An *et. al*. for the synthesis of carbon encapsulated Cu nanoparticles.[20] However, the extraordinarily high temperature and pressure of 3053 K and 21 GPa were needed. The other method of solid-state reduction reaction process was reported as the synthesis technique of carbon coating covered on Cu particles at a lower temperature of 350 ºC under nitrogen atmosphere by Li *et. al.*.[21] However,

the coating was realized as amorphous carbon, which reduces the material conductivity. As mentioned above, current methods show up the high technology, require an extreme reaction condition, or cannot get the NG coating at ambient conditions. Therefore, there still requires an alternative approach to simply fabricate the metal-carbon core-shell structure at ambient temperature and pressure conditions.

Over the last few years, a new method called solution plasma (SP), which is a non-equilibrium plasma discharge in solution, brings a lot of attention to researchers and scientists.[22] Because of their eases of setup and no particular condition requirements, it would be an efficient way to synthesize the preferred material. In many previous reports, the SP method was successfully used to synthesize many kinds of contents, such as metal and bi-metal nanoparticles manufactured in an aqueous solution,[23-25] allotropes of carbon materials from organic solvents,[26-28] as well as composite materials between carbon and metallic elements.[29-31] Recently, we have been reported about the fabricating of Cu nanoparticles encapsulated with the NFG coating by using the SP for the first time.[32] In this research, we aimed to discover the ability to use the core-shell material of the Pt nanoparticle encapsulated by the NFG (Pt-NFG) *via* the SP process in terms of the high durability and efficiency catalytic performance for the ORR. The Pt electrode is a source of the metal-core, while the dimethylformamide (DMF) precursor acts as the nitrogen-containing carbon source for shells. Their structures, morphologies, and characteristics were revealed by several techniques such as transmission electron microscopy (TEM), X-ray diffraction (XRD), Raman spectroscopy, and X-ray photoelectron spectroscopy (XPS). After that, the oxidation resistance of the Pt-NFG sample was compared to that of commercial Pt/C in an immersion test under an acidic medium at a high temperature. Lastly, the ORR measurement was also conducted to evaluate the catalytic ability of the synthesized sample.

3.2. Experimental procedures

3.2.1 Materials

Dimethylformamide (DMF, 99.5 %), acetone (> 99.5 %), hydrofluoric acid (HF,

46.0 % ~ 48.0 %), hydrochloric acid (HCl, 35.0 % ~ 37.0 %) and 0.5 M sulfuric acid (H_2SO_4, 99.5 %) were purchased from Kanto Chemical Co., Inc., Japan. Platinum nanoparticle (particle size < 50 nm), Nafion® D-521 solution (5 wt% in a mixture of lower aliphatic alcohols and water), 20 wt% platinum on Vulcan XC-72 (20 % Pt/C), and standard solution of platinum, palladium, gold, and silver concentration 1000 $mg \cdot l^{-1}$, were purchased from Sigma Aldrich, Germany. Platinum (Pt, 99.98 %) 1.0 mm diameter wires were purchased from Nilaco Co., Japan.

3.2.2 Solution plasma (SP) synthesis

In the SP synthesis setup, a pair of Pt electrodes covered by insulating ceramic tubes were placed into a glassy reactor with a gap distance between their tips at 1.0 mm (Figure 3.1). Plasma was discharged at the tips of two Pt electrodes placed under 100 ml of the DMF solution using a bipolar pulsed power supply (Kurita Seisakusho Co., Ltd., Japan). During the plasma discharge, the pulse width and repetition frequency parameters were fixed at 1.0 µs and 30 kHz, respectively. After 60 min of the reaction, the solution mixture was filtered to collect the solid powder using PTFE 0.1 µm membrane (JVWP04700, Merck). The collected powder was washed several times using acetone before drying at a temperature of 100 ºC for 12 h. Finally, the sample was kept in a dark bottle in a desiccator.

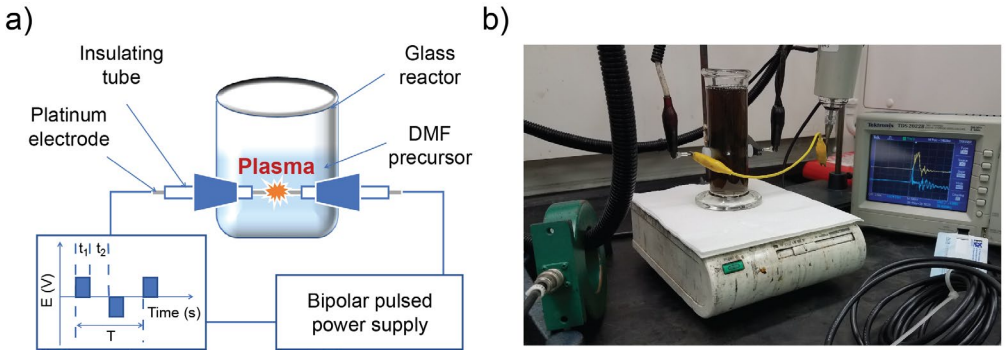

Figure. 3.1 Experimental setup (a) and the digital photo of the SP synthesis (b).

3.2.3 Characterization

The morphologies and nanostructures of the synthesized Pt-NFG sample were observed by high-resolution transmission electron microscopy (HR-TEM, JEM-2100F, JEOL Ltd., Japan) at

an accelerating voltage of 200 kV. X-ray diffraction (XRD, Rigaku Corp., Japan) using Cu Kα radiation (λ = 0.154 nm) was measured to compare the crystal structures between the Pt-NFG and commercial Pt/C samples at a scan rate of 4 degrees per minute. Raman spectroscopy (Raman, Leica DM 2500M Ren (RL/TL) microscope, Renishaw Plc., England) was also applied to indicate the carbon structural information using a 532 nm laser excitation source. Mass composition of the Pt-NFG sample was also revealed by thermal gravimetric method (TGA, TGA&DTG-60AH, Shimadzu Co., Japan) using a heating rate of 10 $^{o}C \cdot min^{-1}$ in air. X-ray photoelectron spectroscopy (XPS, PHI 5000 Versa Probe II, ULVAC-PHI, Inc., Japan) was applied to analyze the elemental composition of the obtained Pt-NFG sample with Mg Kα X-ray source.

3.2.4 Electrochemical tests

The electrochemical properties of the Pt-NFG and commercial Pt/C samples were tested by cyclic voltammetry (CV) and linear sweep voltammograms (LSVs) methods. For the measurement setup, the three-electrode cells consisted of a rotating ring-disk electrode (RRDE, HR2-RD1-Pt8/GC5), Ag/AgCl electrode, and platinum electrode as the working electrode, reference electrode, and counter electrode, respectively, which were connected with a potentiostat (Hokuto Denko Inc. HZ500) system. For fabrication of the catalyst ink, sonification method was used to disperse 5.0 mg sample into 0.5 ml of isopropanol and 50 µl of Nafion® solution for 2 h. A 10.0 µl of the prepared catalyst was dropped onto the glassy disk of the RRDE and then dried up at room temperature. Before the measurement, N_2 gas has flowed into 0.5 M H_2SO_4 electrolyte for 60 min for the O_2 degassing process. Then, O_2 gas has flowed into for 30 min to estimate the ORR performance of the obtained samples. CV curves were obtained with the potential range from 0.0 to 1.4 V (V vs. RHE) at a scan rate of 50 $mV \cdot s^{-1}$. Besides that, LSV results were also measured with the potential sweep from 1.2 to 0.2 V (V vs. RHE) at a scan rate of 10 $mV \cdot s^{-1}$.

Moreover, the hard X-ray absorption fine structure (XAFS, BL11S2, Hard X-ray XAFS II, Aichi Synchrotron Radiation Center, Japan) was also used for obtaining the physical morphology of the samples before and after a 500 CV cycles measurement.

3.2.5 Durability tests

The durabilities of the Pt-NFG and commercial Pt/C samples were examined by acid immersion with and without applying a static potential. The amount of the Pt corroded from the tested samples was inverted to a mass loss percentage for evaluation of the durability performance. For the immersion test with the applying of static potential, the suspension of each 40.0 µl sample, which was prepared as mentioned in the electrochemical test, was dropped onto the glassy carbon electrode and dried at room temperature. The tests were performed in 100 ml of a mixed solution of H_2SO_4 pH 3, 30 $mg{\cdot}l^{-1}$ HF, and 10 $mg{\cdot}l^{-1}$ HCl at 80 ºC and using three-electrode cells with a static potential of 0.9 V (V vs. RHE) for 100 h. Besides that, the immersion test without applying a static potential was also applied for every 10.0 mg of the synthesized sample powders which was immersed into the same acid solution at 80 ºC for 100 h. As a reference, the commercial Pt/C was also examined in the durability test with the same condition. Inductively coupled plasma atomic emission spectroscopy (ICP-OES, SPS7800, Hitachi Co., Japan) was applied for detecting the Pt ion content from the collected solution. As results, the Pt mass loss amount and mass loss percentage values can be determined as follows:

Mass loss amount:

$$m_{Pt,\ loss} = \frac{C_{Pt,\ mg{\cdot}l^{-1}} \times V_{dd}}{1000}\ (g) \tag{1}$$

Mass loss percentage:

$$x_{Pt,\ loss} = \frac{m_{Pt,\ loss}}{m_0}\ (\%) \tag{2}$$

where: $C_{Pt,\ mg{\cdot}l^{-1}}$ is the concentration of Pt ion ($mg{\cdot}l^{-1}$), V_{dd} is the tested volume (l) and m_0 is the mass of the tested sample (g).

3.3. Results and discussion

First, the TEM photos of the Pt-NFG and commercial Pt/C samples were recorded to understand their morphology. As can be seen in Figure 3.2 (a, b), the TEM photos of commercial Pt/C indicated several Pt nanoparticles were dispersed on the carbon-based with the size range

from 2 nm to 7 nm. Oppositely, the synthesized Pt-NFG particles were agglomerated particles with an average size at around 2.3 nm (Figure 3.2 (c, d)). Moreover, the enlarged-view images of the Pt-NFG sample revealed the presence of the thin coating of 2 layers closely covered on the core. Besides, the presences of the Pt, carbon, and nitrogen atoms on the Pt-NFG sample were also detected using the TEM-EDS with results shown in Figure 3.3. Based on the TEM results, the Pt coated by the NFG layer could be obtained by using the SP synthesis. This coating-shell has been reported that it helps to stabilize the metal core catalyst.[33]

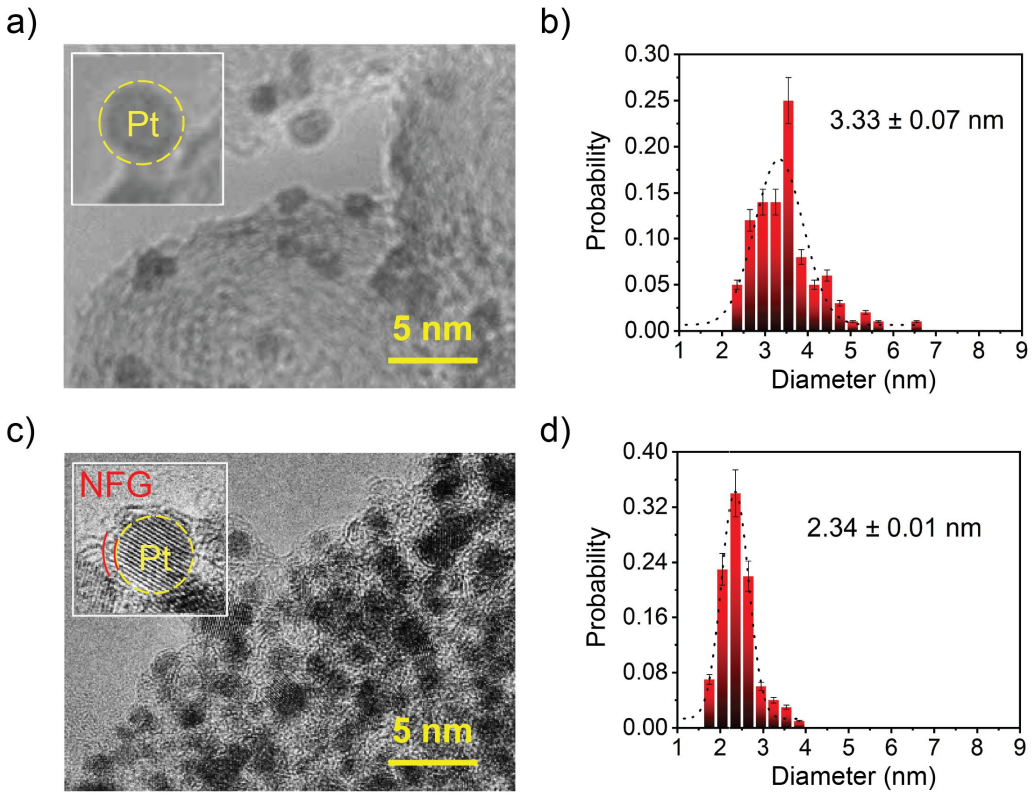

Figure 3.2 HR-TEM images (left) and size distribution results (right) for commercial Pt/C (a, b) and Pt-NFG (c, d).

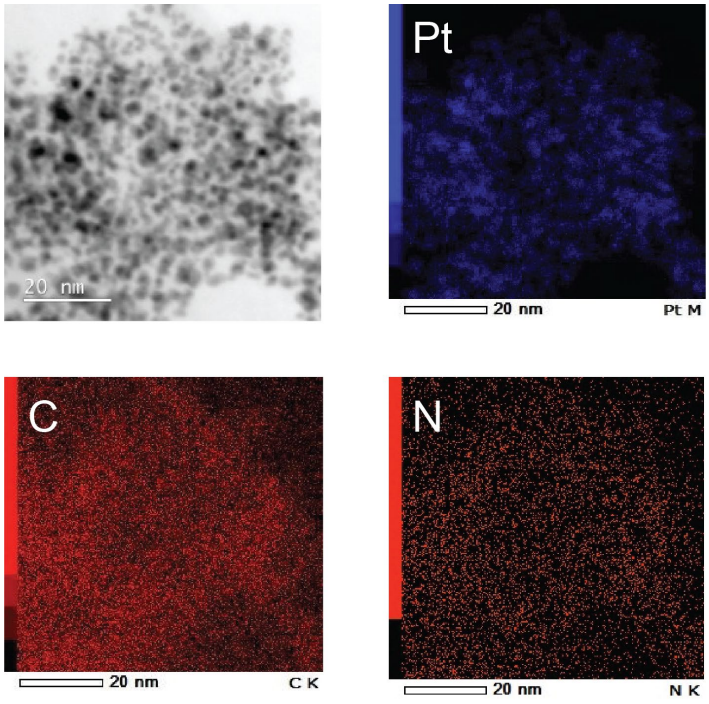

Figure 3.3 TEM-EDS elemental mapping of Pt-NFG.

The Pt-NFG structure was further determined using the XRD measurements. The XRD patterns in Figure 3.4 (a) indicated a broad diffraction peak at 23.50º corresponding to the (002) plane of graphene.[34] Also, the sharp peaks exhibited at 39.70º, 46.15º, 67.40º, and 81.20º, corresponding to the Pt 111, Pt 200, Pt 220, and Pt 311 planes of Pt cores. Oppositely, the XRD pattern of the commercial Pt/C sample indicated two clear broad peaks at about 25.00º and 39.70º which indicated the C 002 peak of amorphous carbon and Pt 111 of low crystallinity of Pt particles, respectively.

The carbon structural information of the Pt-NFG and Pt/C samples was investigated by the Raman measurement. As shown in Figure 3.4 (b), the Raman spectra of the Pt-NFG sample reveals the three evident peaks at approximately 1580, 2675, and 2940 cm^{-1}, which represent the G, 2D, and G+D bands as signatures for the sp^2 structure of graphene.[26] Besides, the representation of the D band approximately at 1348 cm^{-1} indicates defects on graphene.[35] The relative intensity ratio of the D to G band (I_D/I_G) is typically used for the defect ratio in the carbon structure.[36, 37] The relative intensity of the D band to the G band (I_D/I_G) of the Pt-NFG sample was 0.892, which

was also caused by the nitrogen doping due to the presence of the D' band in the Raman result.[26] Besides, the value of I_{2D}/I_G can be used to identify monolayer ($I_{2D}/I_G > 2$), bilayer ($I_{2D}/I_G \approx 1$), and multilayer ($I_{2D}/I_G < 1$) of graphene.[38] The values of I_{2D}/I_G obtained in the Raman result of the Pt-NFG sample was identified at 0.363, which could be implied that the NFG shell was multilayer graphene. Otherwise, the full width at half maximum (FWHM) value of the 2D band was also calculated with the value at 79.46 cm^{-1} which also indicated that the obtained shell was the few-layers graphene.[39] In the case of the commercial Pt/C sample, the Raman indicated only two peaks of the D and G bands identifying for the presences of the defects and graphite structures of the carbon supports. Due to the high ratio value of I_D/I_G, the carbon on the commercial Pt/C sample indicated the large defect sites on the surface of graphitized carbon caused by the deposition of the Pt nanoparticles.[40]

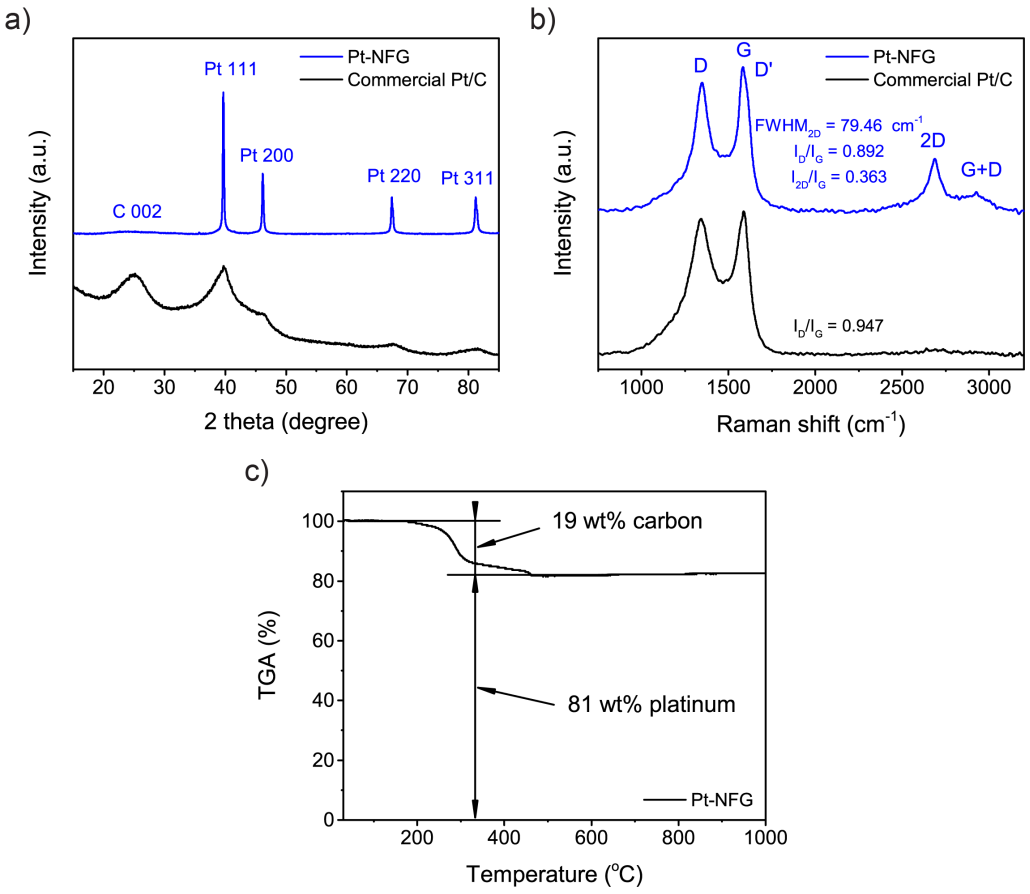

Figure 3.4 XRD patterns (a), Raman spectrum (b) of the commercial Pt/C and Pt-NFG, and TGA curve of Pt-NFG (c).

The core-shell composition of the Pt-NFG sample was also determined and showed in Figure 3.4 (c). During the heating from 25 ºC to 1000 ºC, the TGA curve indicated the mass loss of the NFG shell at about 20 % from the decomposition processes which started at 200 ºC and then finished at around 700 ºC. Based on this result, the Pt nanoparticles showed the main composition in the Pt-NFG sample.

Furthermore, the surface element compositions and the chemical states of the Pt-NFG and commercial Pt/C samples were investigated by the XPS measurement. The XPS result of the Pt-NFG sample showed the C, N, O, and Pt atomic compositions at 83.96, 1.53, 5.14, and 9.37 at%, respectively. The presence of the N element in the XPS result indicated that nitrogen was successfully doped on the graphene framework. To understand the chemical state of the synthesized samples, the high-resolution XPS spectra were also deconvoluted and displayed in Figure 3.5. The C 1s spectrum, shown in Figure 3.5 (a), exhibited a strong peak at 284.3 ± 0.1 eV of the sp^2 bonding configuration. Besides that, the following five deconvoluted peaks were represented for the C–N (285.4 ± 0.2 eV), C–O (285.8 ± 0.1 eV), C=O (286.6 ± 0.2 eV), O–C=O (289.2 ± 0.2 eV) and π–π* interaction (289.9 ± 0.1 eV).[41, 42] In case of N 1s spectrum, the four components corresponding to Pyridinic N (398.6 ± 0.2 eV), Pyrrolic N (399.5 ± 0.2 eV), Quaternary N (401.3 ± 0.2 eV) and Oxidized N (403.2 ± 0.2 eV) are shown in Figure 3.5 (b).[43] Notably, the significant contribution of the Pyrrolic N, Pyridinic N, and Quaternary N in the N 1s peaks indicated that the nitrogen dopants were mostly bonded to the neighbouring carbon atoms.[44] For understanding the effect of the NFG shell on the Pt core, the Pt 4f peaks of the Pt-NFG and commercial Pt/C samples were deconvoluted and exhibited in Figure 3.5 (c, d). The Pt 4f spectra of the Pt-NFG sample indicated the two main peaks at 71.2 eV and 74.6 eV which represented the Pt $4f_{7/2}$ and Pt $4f_{5/2}$ states, respectively. Comparing to the Pt $4f_{7/2}$ and Pt $4f_{5/2}$ from the commercial Pt/C sample, which was located at 70.7 eV and 74.2 eV, the related peaks from the Pt-NFG sample were positively shifted. These positive shifts were caused by the effect of difference electronegativity between the Pt-core and the NFG-shell.[45-47] Pt transfers its electron to the carbon shell making itself less electron-dense which was enhanced by nitrogen atoms due

to the more electronegative compared with the carbon atom. Thus, the upshift of binding energy on the Pt 4f state in the Pt-NFG sample indicated the interaction of the metal-core to carbon-shell.

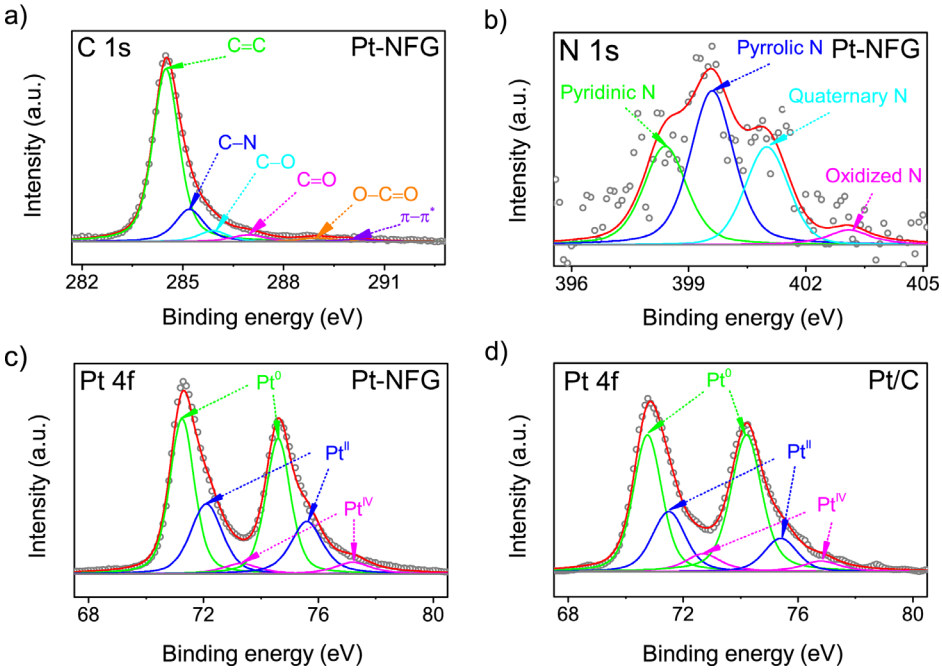

Figure 3.5 Deconvoluted XPS peaks of C 1s (a), N 1s (b), and Pt 4f (c) of Pt-NFG and Pt 4f (d) of commercial Pt/C.

For understanding the ORR performance of the Pt-NFG sample, the cyclic voltammetry (CV) and linear sweep voltammetry (LSV) methods were conducted and compared with that of the commercial Pt/C sample. They were performed in the 0.5 M H_2SO_4 electrolyte with the presence of O_2 bubbling in solution with the scan rate at 50 $mV \cdot s^{-1}$ (Figure 3.6 (a)). The potential between 0.0 to 0.4 V (V vs. RHE) was attributed to the hydrogen region, which can indicate the adsorption and desorption abilities of the tested catalysts with hydrogen.[48] The electrochemical surface area (ECSA) was also calculated by using hydrogen underpotential deposition (H_{upd}) method together with assuming the charge transfer of a hydrogen monolayer contributed by Pt (Q_H) is 210 $\mu C \cdot cm^{-2}$. The ECSA values of the commercial Pt/C and Pt-NFG samples were showed at 59.74 and 29.81 $m^2 \cdot g^{-1}$, respectively. From the results, the ECSA of the Pt-NFG sample was lower than of the commercial Pt/C sample which indicated that the presence of the NFG coating caused the reduction of the hydrogen amount for interacting directly to the Pt-core. The result

pointed out that the lower hydrogen adsorption/desorption ability was showed to the Pt-NFG sample compared to that of the commercial Pt/C sample. At the oxygen region of the potential ranging from 0.4 to 1.4 V (V vs. RHE), the CV curves in the O_2-saturated solution of the Pt-NFG and commercial Pt/C samples exhibited strong peaks which represented the ORR. However, the peak potentials of the Pt-NFG sample showed the negative shifts differed from the commercial Pt/C sample which might be related to the effect of the NFG shell. For finding more detailed performance of the ORR, the LSV curves obtained from the reaction from catalyst on the RRDE electrodes were also conducted at a disk rotation speed by 1600 rpm with the negative sweep of potential from 1.2 to 0.2 V (V vs. RHE). The Pt-NFG sample represented the comparable onset potential compared with the commercial Pt/C sample (0.880 V (V vs. RHE)). Besides that, the Pt-NFG sample also indicated the comparable current density from the disk electrode at 4.314 $mA \cdot cm^{-2}$, which was almost as good as the correlation values of the commercial Pt/C sample (at 4.438 $mA \cdot cm^{-2}$). Additionally, the mass activities (MA) and specific activity (SA) of the Pt-NFG and Pt/C samples were calculated using kinetic current (I_k) at 0.8 V (V vs. RHE). From the results, the MA values of the Pt-NFG and Pt/C samples were 19.27 and 31.82 $mA \cdot mg^{-1}$, respectively. However, the SA result of the Pt-NFG sample indicated the higher value at 64.63 $\mu A \cdot cm^{-2}$ compared to that of the commercial Pt/C sample (53.27 $\mu A \cdot cm^{-2}$). The result of the lower MA together with the higher SA from the Pt-NFG sample, compared to the commercial Pt/C sample, suggested that the few-layer heteroatom-doped graphene might be the key for preserving the ORR activity of the core-shell sample in this study, while the previous study reported that a pristine graphene shell could alter the active surface of metal-core.[49]

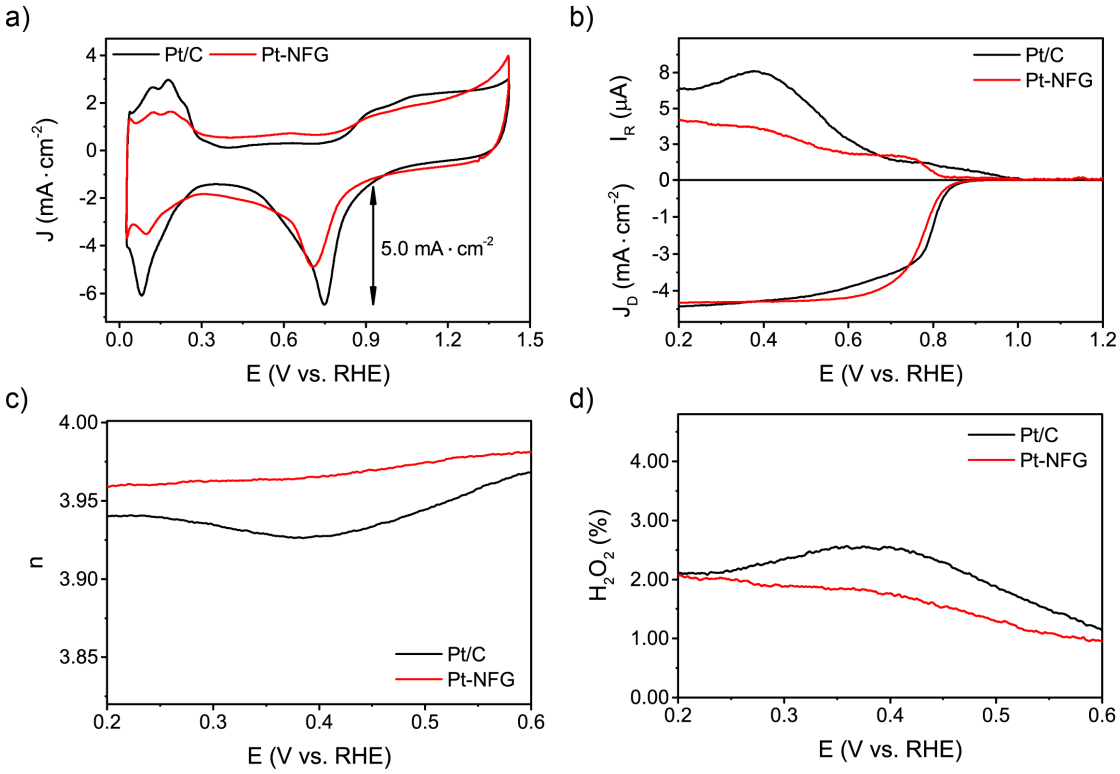

Figure 3.6 CV curves from the electrochemical measurements with scan rate at 50 $mV \cdot s^{-1}$ (a). LSV (b), electron transfer number (c), and H_2O_2 yields (d) results from the electrochemical measurement with scan rate at 10 $mV \cdot s^{-1}$.

The possible pathways of the ORR which can proceed through two general pathways, direct four-electron, and two-electron pathways, were also evaluated in the 0.5 M H_2SO_4 electrolyte. The direct four-electron pathway is ideal ORR in fuel cell application which shown as below:

$$O_2 + 4H^+ + 4e^- \rightarrow 2H_2O \qquad (E^o = +1.23\ V) \qquad (3),$$

while the two-electron pathway conducts a two-step reduction as shown below:

$$O_2 + 2H^+ + 2e^- \rightarrow H_2O_2 \qquad (E^o = +0.70\ V) \qquad (4),$$

$$H_2O_2 + 2H^+ + 2e^- \rightarrow 2H_2O \qquad (E^o = +1.78\ V) \qquad (5).$$

The generated hydrogen peroxide percentage and electron transfer number (*n*) per O_2 values were then discovered as equations bellow:

$$n = 4 \times \frac{I_{disk}}{I_{disk} + I_{ring}/N} \qquad (6),$$

$$\%H_2O_2 = \frac{200 \times I_{ring}}{N \times I_{disk} + I_{ring}} \quad (7).$$

Where I_{disk} and I_{ring} are the currents obtained from the RRDE at the inner carbon disk and the outer Pt ring, respectively. The collection efficiency (N) was exhibited at 0.482 using 0.1 M $HClO_4$ with a 10 mM $K_3Fe(CN)_6$ electrolyte. As the result in Figure 3.6 (c), the n values of the tested samples derived from the RRDE measurements were ranging from 3.92 to 3.98. Notably, the n values of the Pt-NFG sample was higher than the commercial Pt/C sample in the whole measurement range. Besides that, the significantly low H_2O_2 (1–2 %) was also observed for the Pt-NFG sample. The results could be proposed that the obtained Pt-NFG nanoparticles coated with the few-layer of the NG tended to catalyze the ORR through a direct four-electron pathway, similar to the commercial Pt/C sample.

To confirm the physical change of the catalysts, we could only present the preliminary result of XAFS measurement for the commercial Pt/C and Pt-NFG samples before and after 500 CV cycles measurement. The results were displayed in Figure 3.7 when the XAFS spectra before ORR was compared with that after ORR. For the commercial Pt/C sample after ORR, the increase of the peak intensity at 11585 eV was observed in the XAFS result which indicated that there was a physical change occurred. Oppositely, the Pt-NFG sample indicated a similar peak position with the Pt plate reference before and after measurement which indicated that the Pt core structure nearly unchanged during the CV measurement.

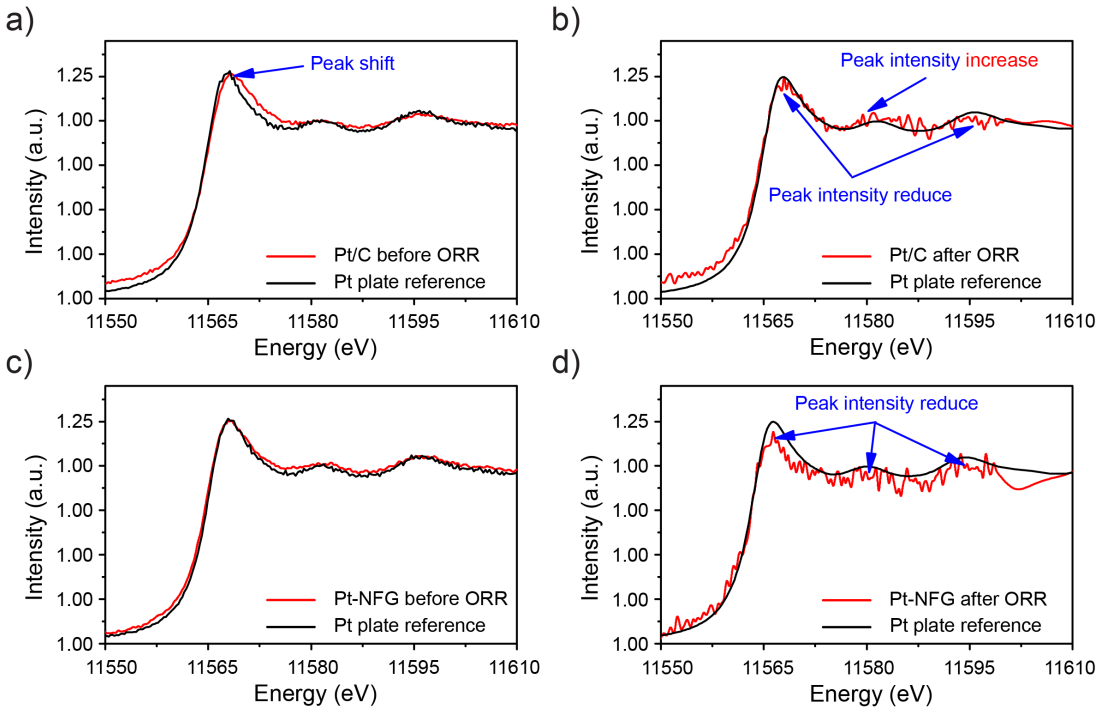

Figure 3.7 XAFS patterns before (left) and after (right) ORR measurement of commercial Pt/C (a, b) and Pt-NFG (c, d).

For a further demonstration of the protection ability of the NFG coating, the immersion test without applying a static potential was also applied in an 80 ºC acidic solution for 100 h. The results in Figure 3.8 displayed the mass loss percentage of the Pt-NFG sample was at around forth times lower than that of the commercial Pt/C sample. Besides that, Figure 3.8 also revealed the result from the durability tests with the applying static potential at 0.9 V (V vs. RHE) in an 80 ºC acidic solution for 100 h. The percentages of the Pt mass loss from the Pt-NFG sample in this measurement was also indicated the lower value compared to that of the commercial Pt/C sample. Accordingly, not only the comparable ORR activity to the commercial Pt/C sample with highly selective toward four-electron reduction but the Pt-NFG nanoparticles also presented better durability due to the effect of the NFG coating.

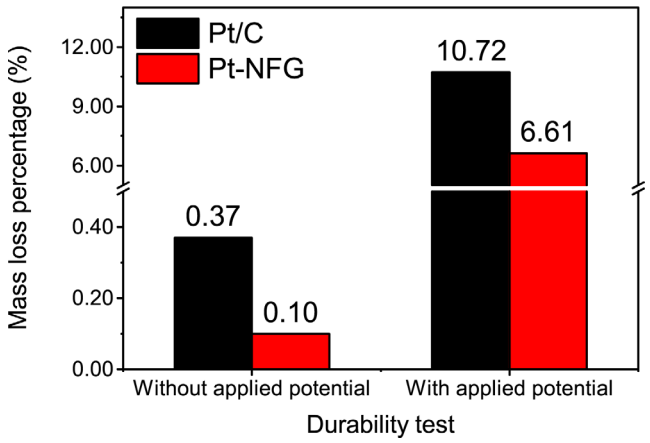

Figure 3.8 Durability test results of commercial Pt/C and Pt-NFG.

The possible mechanism of the O_2 adsorption and ORR of the metal nanoparticles captured in the few-layer of the NG was also proposed, as shown in Figure 3.9. Theoretically, the O_2 could be adsorbed on the carbon-based metal-free catalyst by two possible modes, including side-on (Yeager model) and end-on (Pauling model).[12] Then, both protons and electrons were transferred to the adsorbed oxygen which was called proton-coupled electron transfer (PCET).[50] After PCET, the ORR follows. The metal-core and the NFG-shell promote the proton adsorption onto the NFG-shell surface by the interfacial interactions that reduce the free energy for protons adsorption.[51] Also, the existences of the nitrogen and oxygen atoms, which have higher electronegativity than that of the carbon atom in the NG, create electropositive sites. These promote the O_2 adsorption onto the NG surface by decreasing the adsorption barrier.[12, 52] Typically, the metal-free carbon catalyst, even nitrogen-doped carbon, is preferential to the associative adsorption as shown below:

$$O_{2(g)} + * \rightarrow O_2^* \quad (8)$$

$$O_2^* + H^+ + e^- \rightarrow HOO^* \quad (9)$$

$$HOO^* + H^+ + e^- \rightarrow O^* + H_2O \quad (10)$$

$$O^* + H^+ + e^- \rightarrow HO^* \quad (11)$$

$$HO^* + H^+ + e^- \rightarrow H_2O + * \quad (12)$$

where * stands for adsorption site on a catalyst. Since there was a difficulty to overcome the

energy barrier of the dissociative adsorption by breaking the O–O bond.[51, 53] However, the synergistic effect from the presence of both nitrogen atom in the carbon framework and metal-core could reduce the activation energy of the dissociative adsorption of oxygen, shifting the mechanism towards the dissociative adsorption through the Yeager chemisorption as below:[54]

$$O_{2(g)} + 2* \rightarrow 2O^{*} \quad (13)$$

Oxygen atoms can be individually adsorbed and undergo ORR without the formation of the H_2O_2 product. Therefore, the few-layer of the NG encapsulated the Pt nanoparticle, obtained in this study, showed high selectivity for the reaction direction of the four-electron reduction pathway. The shreds of evidence obtained in this work proved that the few-layer of the NG not only acted as a protective shell but also collaborated with the Pt-core to efficiently catalyze the desired ORR. Therefore, the NFG coating encapsulated on the Pt nanoparticles could be proposed as the further ORR catalysts for the electrocatalysis study.

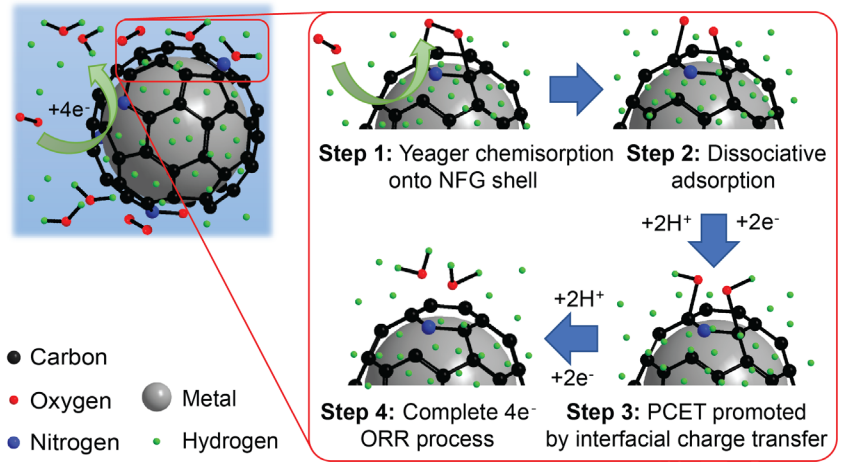

Figure 3.9 Purposed mechanism for ORR and proton transfer of Pt coated by NFG core-shell catalyst synthesized by SP.

3.4 Summary

In conclusion, we have rationally designed and presented the efficient synthesis strategy of the NFG shell coated on the Pt nanoparticle core as the efficient ORR catalysts. The synthesis of the Pt-NFG core-shell was successfully conducted in one pot through the SP process using only the DMF precursor for the carbon source and the Pt electrodes for the Pt source at ambient

temperature and atmospheric pressure. The NFG coating played the remarkable protective shell, which helps to improve the durability of the Pt-NFG catalyst in comparison to commercial Pt/C. Also, the incorporation of the nitrogen atoms in the carbon framework of the NFG shell could collaborate with the Pt-core, leading to the ORR with high selectivity toward the four-electron pathway which is the desired reaction in fuel cell application. This may open a great opportunity for the further development to achieve a new high-performance catalyst, as an alternative to the commercial Pt/C catalyst, through facile and tunable SP synthesis method for the economic practicality and environmental requirements.

References

1. R. E. Yonoff, G. V. Ochoa, Y. Cardenas-Escorcia, J. I. Silva-Ortega and L. Meriño-Stand, *Heliyon*, 2019, **5**, e01724.
2. B. Randrianarizafy, P. Schott, M. Gerard and Y. Bultel, *Energies*, 2020, **13**, 2338.
3. A. de Frank Bruijn and G. J. Janssen, in *Fuel Cells*, Springer, 2013, 249-303.
4. B. Shabani, M. Hafttananian, S. Khamani, A. Ramiar and A. Ranjbar, *J. Power Sources*, 2019, **427**, 21-48.
5. X. X. Wang, M. T. Swihart and G. Wu, *Nat. Catal.*, 2019, **2**, 578-589.
6. X. Zhang and R. Zhang, *Appl. Surf. Sci.*, 2019, **479**, 1039-1047.
7. X. Hou, Q. Hu, P. Zhang and J. Mi, *Chem. Phys. Lett.*, 2016, **663**, 123-127.
8. G. Fazio, L. Ferrighi and C. Di Valentin, *J. Catal.*, 2014, **318**, 203-210.
9. A. Marinoiu, I. Gatto, M. Raceanu, M. Varlam, C. Moise, A. Pantazi, C. Jianu, I. Stefanescu and M. Enachescu, *Int. J. Hydrog. Energy*, 2017, **42**, 26877-26888.
10. L. Samiee, S. Sadeghhassani, M. R. Ganjali and A. Rashidi, *IJHFC*, 2018, **4**, 231-240.
11. S. Zhuang, B. B. Nunna, D. Mandal and E. S. Lee, *Nano-Struct. Nano-Objects*, 2018, **15**, 140-152.
12. D. Guo, R. Shibuya, C. Akiba, S. Saji, T. Kondo and J. Nakamura, *Science*, 2016, **351**, 361-365.

13. A. Heydari and H. Gharibi, *J. Power Sources*, 2016, **325**, 808-815.
14. T. Varga, Á. T. Varga, G. Ballai, H. Haspel, Á. Kukovecz and Z. Kónya, *Carbon*, 2018, **133**, 90-100.
15. R. I. Jafri, N. Rajalakshmi and S. Ramaprabhu, *J. Mater. Chem.*, 2010, **20**, 7114-7117.
16. H. Lee, Y.-E. Sung, I. Choi, T. Lim and O. J. Kwon, *J. Power Sources*, 2017, **362**, 228-235.
17. J. Liu, W. Li, R. Cheng, Q. Wu, J. Zhao, D. He and S. Mu, *Langmuir*, 2019, **35**, 2580-2586.
18. J.-H. Lee, E.-K. Lee, S.-G. Kang, S.-H. Jung, S.-K. Son, W. H. Nam, T.-H. Kim, B. L. Choi and D. Whang, *Appl. Surf. Sci.*, 2018, **440**, 553-559.
19. S. Chen, A. Zehri, Q. Wang, G. Yuan, X. Liu, N. Wang and J. Liu, *ChemistryOpen*, 2019, **8**, 58-63.
20. C. An, P. Ding, B. Ye, X. Geng and J. Wang, *AIP Adv.*, 2017, **7**, 035324.
21. J. Li and C.-y. Liu, *New J. Chem.*, 2009, **33**, 1474-1477.
22. O. Takai, *Pure Appl. Chem.*, 2008, **80**, 2003-2011.
23. J. Zhang, X. Hu, B. Yang, N. Su, H. Huang, J. Cheng, H. Yang and N. Saito, *J. Alloys Compd.*, 2017, **709**, 588-595.
24. T. Sudare, T. Ueno, A. Watthanaphanit and N. Saito, *J. Surf. Finish. Soc. Jpn.*, 2016, **67**, 46-50.
25. P. Pootawang, N. Saito and S. Y. Lee, *Nanotechnology*, 2013, **24**, 055604.
26. S. Chae, G. Panomsuwan, M. A. Bratescu, K. Teshima and N. Saito, *ACS Appl. Nano Mater.*, 2019, **2**, 1350-1355.
27. K. Hyun and N. Saito, *Sci. Rep.*, 2017, **7**, 3825.
28. S. Lee, Y. Heo, M. A. Bratescu, T. Ueno and N. Saito, *Phys. Chem. Chem. Phys.*, 2017, **19**, 15264-15272.
29. J. Kang, Y. Kim, H.-m. Kim, X. Hu, N. Saito, J.-H. Choi and M.-H. Lee, *Sci. Rep.*, 2016, **6**, 38652.
30. D.-w. Kim, O. L. Li, P. Pootawang and N. Saito, *RSC Adv.*, 2014, **4**, 16813-16819.
31. J. Kang and N. Saito, *RSC Adv.*, 2015, **5**, 29131-29134.

32. P. Q. Phan, S. Chae, P. Pornaroontham, Y. Muta, K. Kim, X. Wang and N. Saito, *RSC Adv.*, 2020, **10**, 36627-36635.
33. Y. Su, Y. Zhu, H. Jiang, J. Shen, X. Yang, W. Zou, J. Chen and C. Li, *Nanoscale*, 2014, **6**, 15080-15089.
34. F. T. Johra, J.-W. Lee and W.-G. Jung, *J. Ind, Eng. Chem.*, 2014, **20**, 2883-2887.
35. K. Hyun, T. Ueno, O. L. Li and N. Saito, *RSC Adv.*, 2016, **6**, 6990-6996.
36. C. H. Choi, S. H. Park and S. I. Woo, *J. Mater. Chem.*, 2012, **22**, 12107-12115.
37. G. Panomsuwan, N. Saito and T. Ishizaki, *J. Mater. Chem. A*, 2015, **3**, 9972-9981.
38. P. R. Kidambi, C. Ducati, B. Dlubak, D. Gardiner, R. S. Weatherup, M.-B. Martin, P. Seneor, H. Coles and S. Hofmann, *J. Phys. Chem. C*, 2012, **116**, 22492-22501.
39. P. Tan, W. Han, W. Zhao, Z. Wu, K. Chang, H. Wang, Y. Wang, N. Bonini, N. Marzari and N. Pugno, *Nat. Mater.*, 2012, **11**, 294-300.
40. M. Hara, M. Lee, C.-H. Liu, B.-H. Chen, Y. Yamashita, M. Uchida, H. Uchida and M. Watanabe, *Electrochim. Acta*, 2012, **70**, 171-181.
41. N. Thongwichit, O. L. H. Li, W. Yaowarat, N. Saito and U. Suriyapraphadilok, *Jpn. J. Appl. Phys.*, 2015, **55**, 01AE10.
42. J. Kim, J. Chun, S.-G. Kim, H. Ahn and K. C. Roh, *J. Electrochem. Sci. Technol*, 2017, **8**, 338-343.
43. D.-w. Kim, O. L. Li and N. Saito, *Phys. Chem. Chem. Phys.*, 2014, **16**, 14905-14911.
44. G. Panomsuwan, N. Saito and T. Ishizaki, *Carbon*, 2016, **98**, 411-420.
45. J. Ma, A. Habrioux, Y. Luo, G. Ramos-Sanchez, L. Calvillo, G. Granozzi, P. B. Balbuena and N. Alonso-Vante, *J. Mater. Chem. A*, 2015, **3**, 11891-11904.
46. P. Kannan, T. Maiyalagan, N. G. Sahoo and M. Opallo, *J. Mater. Chem. B*, 2013, **1**, 4655-4666.
47. T. Holme, Y. Zhou, R. Pasquarelli and R. O'Hayre, *Phys. Chem. Chem. Phys.*, 2010, **12**, 9461-9468.
48. D. Zhan, J. Velmurugan and M. V. Mirkin, *J. Am. Chem. Soc.*, 2009, **131**, 14756-14760.

49. M. Topsakal, H. Şahin and S. Ciraci, *Phys. Rev. B*, 2012, **85**, 155445.
50. E. Odella, S. J. Mora, B. L. Wadsworth, J. J. Goings, M. A. Gervaldo, L. E. Sereno, T. L. Groy, D. Gust, T. A. Moore and G. F. Moore, *Chem. Sci.*, 2020, **11**, 3820-3828.
51. Y. Peng and S. Chen, *Green Energy Environ.*, 2018, **3**, 335-351.
52. D. Deng, L. Yu, X. Chen, G. Wang, L. Jin, X. Pan, J. Deng, G. Sun and X. Bao, *Angew. Chem.*, 2013, **125**, 389-393.
53. L. Yu, X. Pan, X. Cao, P. Hu and X. Bao, *J. Catal.*, 2011, **282**, 183-190.
54. K. Gong, F. Du, Z. Xia, M. Durstock and L. Dai, *Science*, 2009, **323**, 760-764.

Chapter 4

Nitrogen-Doped Few-Layer Graphene Encapsulated Pt-Based Bimetallic Nanoparticle Synthesis by Solution Plasma as an Efficient Oxygen Reduction Reaction Catalyst

Chapter 4 - Nitrogen-Doped Few-Layer Graphene Encapsulated Pt-Based Bimetallic Nanoparticle Synthesis by Solution Plasma as an Efficient Oxygen Reduction Reaction Catalyst

4.1. Introduction

The fossil fuel cells consumptions have been rapidly increasing leading to the depletion of fossil fuel resources as well as the global pollution in the world. To face that global issue, scientists and researchers have been focusing on finding alternative sustainable energy sources in both natural and man-made energy. As one of the efficient power generation, fuel cells have been extensively studying on replacing conventional energy conversion devices.[1] Notably, the proton exchange membrane fuel cell (PEMFC) has been presented as one of the most desirable technology because it has been presented the high conversion efficiency of the chemical energy to electrical energy without causing pollution at low temperature.[2] In the PEMFC system, the rate-determining step influencing the overall electricity source was mainly related to the oxidization process of H_2 gas on the anode which releasing electrons as well as the reduction process of O_2 molecules at the cathode.[3] Between them, the oxygen reduction reaction (ORR) places the most important key for improving the PEMFC performance due to the large overpotential. Platinum (Pt) has been proposed as an extremely effective cathodic catalyst since it can effectively promote the ORR at low temperatures.[4] On the other hand, the high cost due to the large Pt used amount leading to the difficulty in applying the PEMFC system to common applications.

Recently, Pt-based bimetallic nanoparticles have been drawn enormous attention to cut down the PEMFC price.[5-7] Outstandingly, alloying the Pt with transition metal (M) to form PtM bimetallic catalysts have been demonstrated as the higher catalytic activities compared to the commercial Pt/C such as Pt_3Ag/C, Pt_3Au/C, and Pt_3Pd/C alloys.[8-10] The electrocatalyst activity

enhancement of the PtM bimetallic was justified by the two theories of the compressive strain and electronic ligand effect.[11] The presences of the transition metal atoms in the structure of the Pt lattice influence the electronic charge redistribution on the catalyst surface. As a result, the binding energy and releasing ability between the PtM surface with the reactants can be altered to enhance the ORR performance.[12] Even though the Pt and PtM bimetallic materials have been exhibited as the excellent catalysts for the ORR, the improvement of their durability and stability is still one of the concerning issues.[13]

Currently, carbon materials, which have excellent electronic conductivity, high thermal and chemical stability, and low cost have been broadly used as support for PtM catalysts in the form of composite material. Remarkably, nitrogen-doped graphene (NG) is one of the important candidate materials in the carbon support material, due to its promising properties, exceptionally high chemical stability, and catalytic ability.[14-16] To get those high properties, the nitrogen in the carbon structure is placed as an important factor to the availability of the Pt–N interaction which enhances the activation of O_2 due to the up-shifted of the Pt–d states.[17] However, the leaching of the transition metal M in the PtM alloy still causes the low durability of these catalysts. Hence, the ideal structure of the PtM bimetallic nanoparticles encapsulated by the NG core-shell indicates the high potential for optimizing the durability and the ORR activity.

Carbon-encapsulated metal nanoparticles can be produced by various techniques such as chemical vapor deposition and thermal treatment.[18, 19] So far, these methods usually need high temperatures as well as a multi-step process including the synthesis of the metal nanoparticles before the coating process. Recently, solution plasma (SP), a liquid-phase plasma technology, has been reported as a simple way for synthesizing heteroatom-doped carbon and bimetallic nanoparticles under ambient temperature and pressure condition.[20, 21] In the SP process, some molecules in solution nearby the plasma can be transformed into highly reactive species which can react with other surrounding molecules to form products.[20] Therefore, the NG can be done in one-step by using a nitrogen-containing organic solution using SP.[22] In addition, the variable bimetallic materials can also be achieved *via* the SP process during the sputtering process on the

different metal electrodes.[21] According to these phenomena, the PtM bimetallic nanoparticles encapsulated in the NG could be rapidly synthesized *via* the plasma discharge in the nitrogen-containing organic solution between the pair electrodes of the Pt and M materials.

In this research, we applied the SP method to produce the PtAu, PtAg, or PtPd bimetallic nanoparticles encapsulated in nitrogen-doped few-layer graphene (NFG) using different pairs of Pt-Au, Pt-Ag, or Pt-Pd electrodes, respectively, in dimethylformamide (DMF) precursor. Several methods of high-resolution transmission electron microscopy (HR-TEM), X-ray powder diffraction (XRD), X-ray photoelectron spectroscopy (XPS), and Raman spectroscopy were applied to confirm the formation of the PtM bimetallic nanoparticle encapsulated in the NFG (PtM-NFG). Besides that, the ORR catalytic performances of the PtM-NFG samples were also illustrated and compared with the commercial Pt/C catalyst in detail, including their electrocatalytic activity and durability. Lastly, a single-cell measurement was conducted for evaluating the practical application ability of the PtM-NFG in the PEMFC.

4.2. Experimental procedure

4.2.1 Materials

Dimethylformamide (DMF, 99.5 %), acetone (> 99.5 %), 0.5 M sulfuric acid (99.5 %) and methanol (MeOH, > 99.8%) were purchased from Kanto Chemical Co., Inc., Japan. Platinum nanoparticle (particle size < 50 nm), Nafion® D-521 solution (5 wt% nafion in lower aliphatic alcohol and water mixture), and 20 wt% platinum on Vulcan XC-72 (Pt/C) were purchased from Sigma Aldrich, Germany. Platinum (Pt, 99.98 %), palladium (Pd, 99.95 %), gold (Au, 99.95 %), and silver (Ag, 99.99 %) 1.0 mm diameter wires were purchased from Nilaco Co., Japan.

4.2.2 Solution plasma (SP) synthesis

The PtM bimetallic nanoparticles covered by the NFG coating were synthesized via the SP process using the pair of the Pt wire together with Au, Ag, or Pd wire as an opposite electrode. In the SP setup, the electrodes were plugged into a glassy reactor with the gap between their tips at

1.0 mm, as shown in Figure 4.1 (a). Plasma discharge was generated and maintained between the two electrode tips under 100 ml of the DMF precursor using a bipolar pulsed power supply (Kurita Seisakusho Co., Ltd., Japan). During the plasma discharge, the operating conditions were fixed with the pulse width and repetition frequency of 1.0 µs and 30 kHz, respectively. After 60 min of the reaction, the black solid particles were separated and washed with acetone by filtration method using PTFE 0.1 µm membrane (JVWP04700, Merck). The collected solid samples were left in the oven at 100 ºC for 12 h and then kept in a dark bottle in a desiccator before further characterizations.

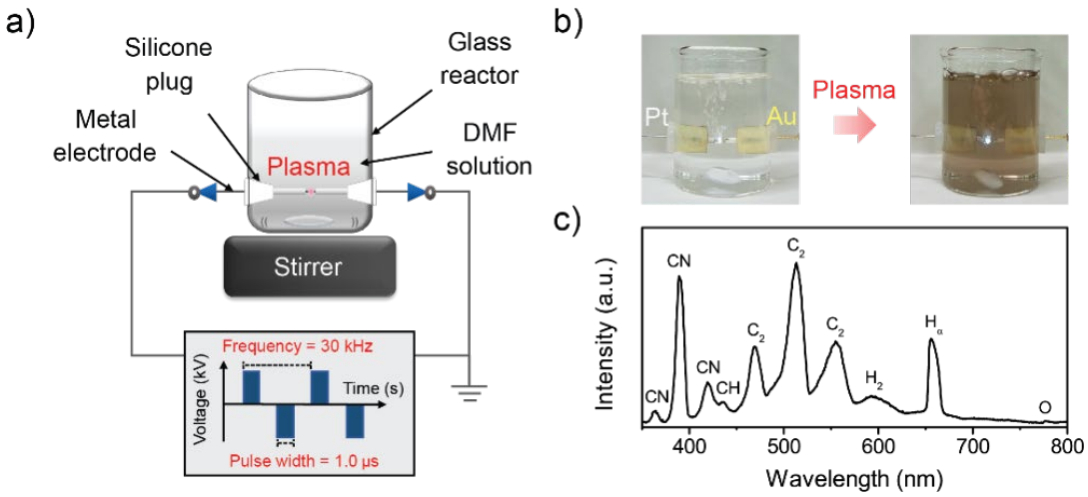

Figure 4.1 Experimental set up of SP process (a), synthesis process of PtAu-NFG (b), and OES spectra of plasma discharge in DMF at 30 kHz (c).

4.2.3 Characterizations

The generated radicals during the SP discharge in the DMF precursor was detected by optical emission spectroscopy (OES, UV/Vis USB 2000+, Ocean Optics Inc., USA). The nanostructures of the synthesized samples were observed by high-resolution transmission electron microscopy (HR-TEM, JEM-2100F, JEOL Ltd., Japan) using an accelerating voltage of 200 kV. The crystal structures of the PtM and NFG were examined using X-ray diffraction (XRD, Rigaku Corp., Japan) with Cu Kα radiation (λ = 0.154 nm) with a scan rate of 4 degrees per minute. Raman spectroscopy (Leica DM 2500M Ren (RL/TL), Renishaw Plc., England) was applied to

study the NFG structural information with a 532 nm laser excitation source. X-ray photoelectron spectroscopy (XPS, PHI 5000 Versa Probe II, ULVAC-PHI, Inc., Japan) with Mg Kα X-ray source was applied to investigate the elemental composition of the fabricated samples.

4.2.4 Electrochemical tests

For evaluating the electrochemical performances of the synthesized samples, the cyclic voltammetry (CV) and linear sweep voltammogram (LSV) measurements were applied using a potentiostat (Hokuto Denko Inc. HZ500) system. Three electrode cells of the working electrode, counter electrode, and reference electrode used in the measurements were rotating ring-disk electrode (RRDE, HR2-RD1-Pt8/GC5), platinum electrode, and Ag/AgCl electrode, respectively. The catalyst ink of 5.0 mg sample mixed with 0.5 ml of isopropanol and 50 µl of Nafion® suspension was prepared using sonification method in 2 h. Every 10.0 µl of prepared catalyst mixture was dropped onto the RRDE and dried before testing. All CV measurements were evaluated in a 0.5 M H_2SO_4 solution with a potential range from 0.0 V to 1.4 V (V vs. RHE) at a scan rate of 50 $mV \cdot s^{-1}$. Besides that, the LSV curve was also obtained with a potential range from 1.2 V to 0.2 V (V vs. RHE) at a scan rate of 10 $mV \cdot s^{-1}$.

Furthermore, the sample with the highest ORR performance was chosen for further investigation using the LSV method after the durability test of 500 CV cycles at the scan rate at 100 $mV \cdot s^{-1}$ from 0.0 V to 1.4 V (V vs. RHE) to indicate the stability performance compared with the commercial Pt/C. Besides that, the chronoamperometric study of the PtPd-NFG and commercial Pt/C samples were also applied in this paper at 0.4 V (V vs. RHE) in 11000 s at a rotating speed at 1600 rpm. For the MeOH tolerant test, the chronoamperometric measurement was also used at 0.6 V (V vs. RHE) with the addition of 3 M MeOH after 500 s measurement.

4.2.5 Single-cell test

The current-voltage data were recorded on the MEA installed in a single cell using a potentio-galvanostat (VMP-300, Biologic) system. Sonication method was used to prepare the

cathode catalyst ink of 4 mg synthesis sample, 16 mg carbon black, 900 µl isopropanol, and 253 µl of 5 wt% Nafion in 1 h. For anode catalyst ink, the same procedure was applied with the used catalyst is 20 mg of the commercial Pt/C. The catalyst ink was dropped onto the Teflon plate with the catalyst loading at 0.2 $mg \cdot cm^{-2}$. To fabricate the MEA, the prepared Teflon plates (cathode and anode with 1 cm^2 area) were pressed at 150 ºC and 2 MPa onto Nafion® Membrane NRE-212 for 3 min. The catalyst performance of the prepared MEA was tested in a fully humidified atmosphere at 80 ºC with 200 sccm of H_2 and O_2 and back pressure at 0.2 MPa.

The electrochemical impedance spectroscopy (EIS) was also used for the single-cell test with the same condition. The sweeping frequencies were ranged from 10 kHz to 10 mHz with 10 points per decade. The amplitude of the AC signal was fixed at 10 mV to measure the steady-state current at 0.7 V and 0.6 V.

4.3. Results and discussion

In this study, the samples obtained were assigned to be PtAu-NFG, PtAg-NFG, PtPd-NFG and Pt-NFG for the NFG coated on PtAu, PtAg, PtPd, and Pt nanoparticle core-shell, respectively. Figure 4.1 (b) illustrates the digital image of the synthesis of the PtAu-NFG core-shell by the SP method. During the SP process, the carbonization and sputtering processes will be occurred leading to the change of the solution colour to dark yellow. The carbon material was produced through the decomposition and recombination of the reactive species (i.e., C_2, CN, CH, and H radicals) generated from the DMF precursor during the SP discharge. These generated radicals were confirmed using the OES spectrometry, as shown in Figure 4.1 (c). A similar phenomenon was also reported in the synthesis of nitrogen-doped carbon nanoparticles using the SP method.[23] Besides, the PtM alloy particles could be formed from the combination of the generated metal atoms from the sputtering process on the electrode tips via the SP process.[24] Therefore, the change of the solution colour related to the suspension of the presences of the carbon and metal particles formed in the DMF solution.

According to the HR-TEM images (Figure 4.2), the obtained particles were found to be the

nano-size particles with an average size of 2–4 nm. Moreover, the core-shell structures were also observed with clear carbon layers. As can be seen in Figure 4.2, the enlarged-view images of each sample indicated the thin coatings of 2 to 4 carbon layers on the metal nanoparticles. These thin layers were found to be the nitrogen-containing carbon due to the presences of both C and N in the TEM-EDS mapping result (Figure 4.3). Besides that, the bimetal structures were indicated using the combination options of the TEM-EDS element mapping and point analysts. As can be seen in Table 4.1, the synthesized samples of the PtAu-NFG, PtAg-NFG, and PtPd-NFG samples indicated the coexisted of the Pt with Au, Ag, and Pd elements, respectively.

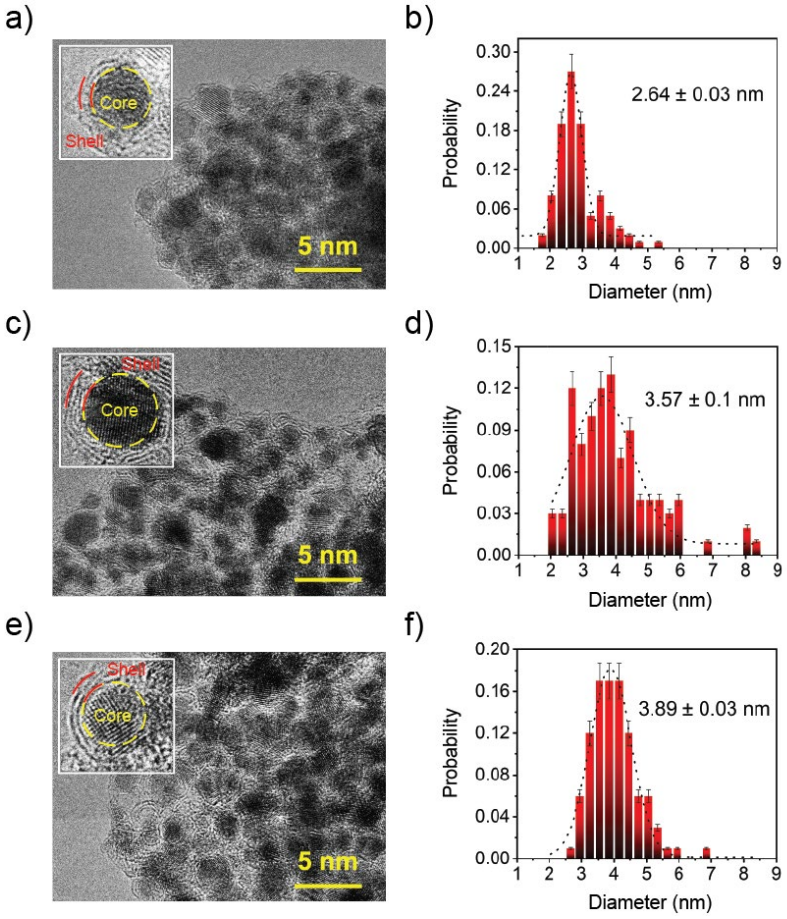

Figure 4.2 HR-TEM images (left) and size distribution results (right) of PtAu-NFG (a, b), PtAg-NFG (c, d), and PtPd-NFG (e, f).

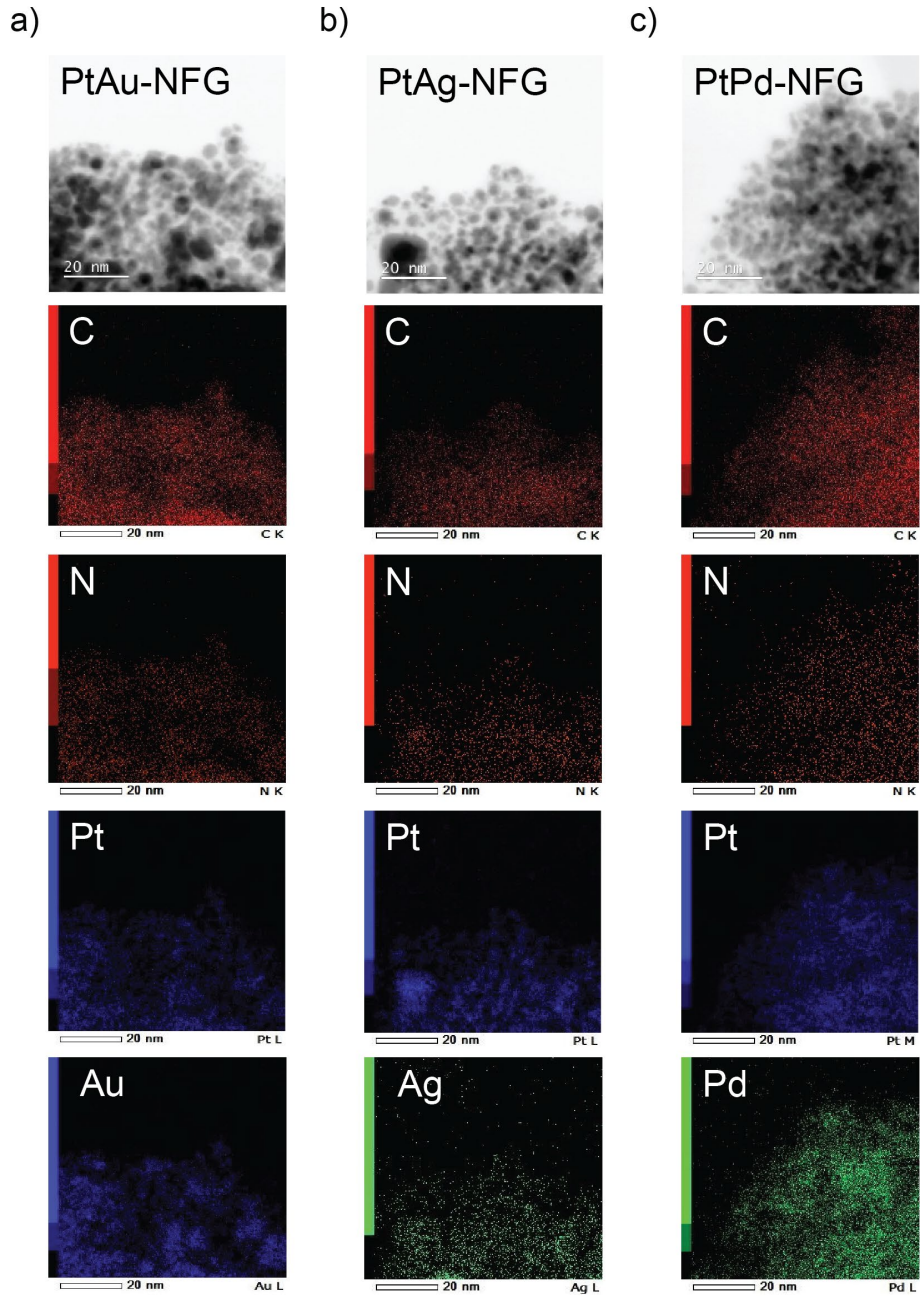

Figure 4.3 TEM-EDS elemental mapping results of PtAu-NFG (a), PtAg-NFG (b), and PtPd-NFG (c).

Table 4.1 TEM-EDS analysis results of element compositions from bi-metal cores.

Element content	**Sample**		
(%)	**PtAu-NFG**	**PtAg-NFG**	**PtPd-NFG**
Pt	32.05	91.37	73.55
Au	67.95	–	–
Ag	–	8.63	–
Pd	–	–	26.45

Structural details of the synthesized samples were distinguished using the XRD and Raman analysts. The XRD results of all synthesized samples (Figure 4.4 (a)) indicated a wide diffraction peak at 2θ = 23.50º, corresponding to the C 002 peak of graphene.[25] Besides, all synthesized samples indicated the high crystallinity of the Pt-cores with the presences of four sharp peaks at 39.70º, 46.15º, 67.40º, and 81.20º corresponded to the Pt 111, Pt 200, Pt 220, and Pt 311 planes, respectively. As can be seen from the enlarged view in Figure 4.4 (b), the Pt 111 plane in the synthesized PtM-NFG samples indicated the slight shift toward the lower 2θ region compared to the relative peak of the pure commercial Pt sample and the value from standard JCPDS cards (Table 4.2). The shifted of the Pt 111 peak related to the lattice strain due to the interaction between the cores and the shells.[26, 27] Besides that, the XRD pattern of each sample indicated some extra peaks, however, the intensity is not that strong compared to the Pt peaks. As detailed, the XRD pattern of the PtAu-NFG sample showed the peaks at 38.65º associating with the Au 111 plane of the Au metal, moreover, the relatively broad peak between (111) planes of the Au and Pt could be observed, which implied to the formation of the PtAu alloyed.[28] As a result, the presences of the Pt, Au, and PtAu peaks from the XRD pattern of the PtAu-NFG sample indicated the coexisting of the individual Au, Pt, and AuPt alloy in the synthesized sample.[24] In the case of the PtAg-NFG and PtPd-NFG samples, the (111) planes of Ag and Pd were not been observable in the XRD result, but the presences of the additional peaks at 38.85º and 39.35º were revealed,

respectively. These additional peaks located at the lower 2θ region compared to the Pt 111 peak suggested that Ag and Pd atoms, which have smaller atomic sizes than that of Pt, were alloyed with Pt atoms. Therefore, the PtAg-NFG and PtPd-NFG samples should contain the Pt nanoparticles as well as the PtAg and PtPd alloy, respectively. The change of the geometric structure from the alloying indicated the potential of altering the binding energy of O_2 on the catalyst surface for tailoring the ORR performance of the alloy catalysts.[12]

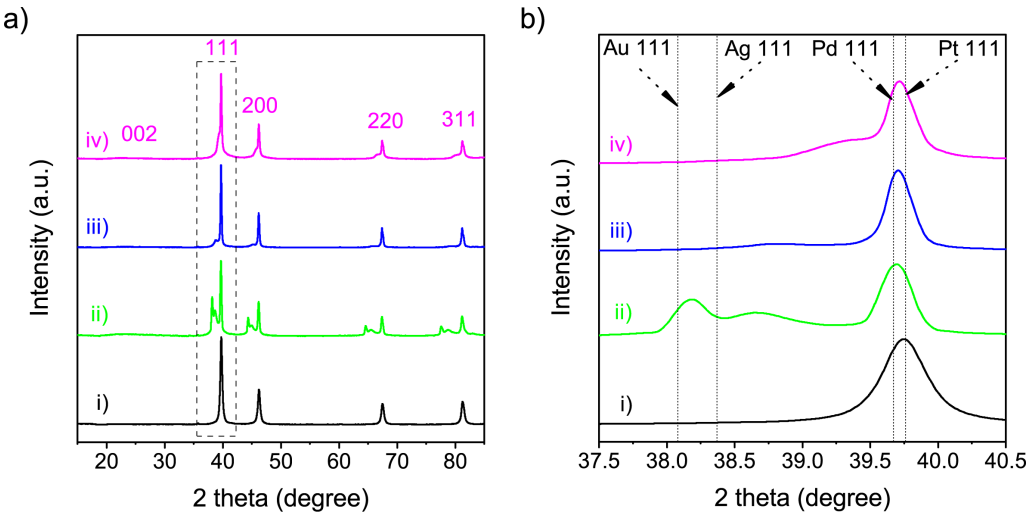

Figure 4.4 XRD patterns (a) and the enlarged view of the XRD peaks corresponding to the (111) plane (b) of the commercial Pt (i), PtAu-NFG (ii), PtAg-NFG (iii), and PtPd-NFG (iv).

Table 4.2 Joint committee on powder diffraction standards (JCPDS) database values of Pt, Au, Ag, and Pd.

Metal	Card number	2 theta (degree)			
		111	**200**	**220**	**311**
Pt	00-004-0802	39.76	46.24	67.46	81.24
Au	01-071-4614	38.08	44.26	64.38	77.31
Ag	01-077-6577	38.37	44.60	64.91	77.99
Pd	00-001-1310	39.67	46.04	66.76	80.68

The NFG structural information was further investigated using the Raman measurement. As shown in Figure 4.5, all obtained samples showed the similar Raman pattern of four main peaks at approximately 1348 cm^{-1}, 1580 cm^{-1}, 2675 $cm^{-1,}$ and 2940 cm^{-1} attributing to D, G, 2D, and G+D bands, respectively.[22] The D band usually indicated some defects while the G band related to the in-plane sp^2 phonon vibrations of carbon atoms in the graphitic planes.[29] The relative intensity ratio of the D to G bands (I_D/I_G) is typically devoted to the graphitization degree of the carbon materials.[30, 31] The I_D/I_G ratios of the obtained samples were estimated and shown in Figure 4.5. As the result, the values of I_D/I_G seemed to be varied depending on the metal nanoparticles in the cores. Also, the presences of the 2D bands in all Raman spectra of the synthesized samples indicated the higher-order carbon structure. In particular, the ratio value of I_{2D}/I_G can be applied to identify the number of the carbon layer.[32] The obtained I_{2D}/I_G values in this work were ranged from 0.34 to 0.38, which could be suggested that the SP-induced shells were multilayer graphene. However, the full width at half maximum (FWHM) of the 2D bands showed the values at below 100 cm^{-1} which indicated the few-layer graphene structure,[33] which was responsible for the TEM results. Additionally, the D' bands were also observed from the Raman spectra for all obtained samples which illustrate the nitrogen dopants in the NFG coatings.[22] Thus, the XRD and the Raman results could be suggested that the obtained nanoparticles in this work had the NFG shell coated on the bimetallic cores.

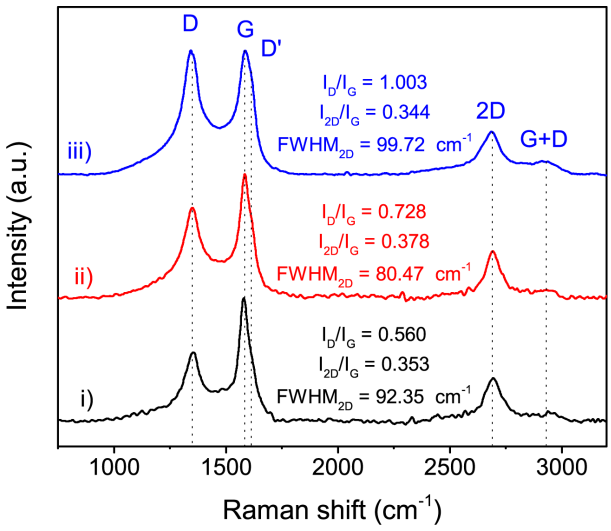

Figure 4.5 Raman spectra of PtAu-NFG (i), PtAg-NFG (ii), and PtPd-NFG (iii).

Furthermore, the surface element composition and chemical states of the synthesized samples were illustrated using the XPS measurement. The XPS results showed that the obtained atomic compositions were found to belong not only from the NFG coatings but also from the PtM bimetallic cores (Table 4.3). According to Table 4.3, the presence of the nitrogen elements could be the evidence representing the successful doping of nitrogen atoms into the graphene framework and N/C ratios were found to be comparable for all obtained samples. The PtPd-NFG sample showed the highest number of heteroatoms of N and O dopants, which was in agreement with the highest value of I_D/I_G=1.01 from the Raman spectroscopy result. For Pt-based bimetallic cores composition, the PtAu-NFG and PtPd-NFG samples indicated the high values of M/Pt ratio at 1.957 and 1.580 which illustrated that the large amounts of the Pt elements were replaced by the Au and Pd, respectively. Combined with the XRD results in Figure 4.4 (b), the metal cores indicated the substitution structures of the Pt lattices due to the stronger Pt 111 peak intensities of the small amount of the Pt elements in synthesized samples. In contrast, the PtAg-NFG sample showed a lower percentage of the Ag content in the core with the M/Pt value at only 0.415. The low atomic percentage of Ag obtained from the TEM-EDS and the XPS indicated that the bimetallic core of the PtAg-NFG sample still contains mainly Pt metal. Besides, the high-resolution XPS spectra were then deconvoluted to gain a deeper insight into the chemical bonding states of a particular element, as displayed in Figure 4.6. The XPS spectra of the Pt 4f of the PtM-NFG samples were found to have two main peaks at 71.2 eV and 74.6 eV which represented the Pt $4f_{7/2}$ and Pt $4f_{5/2}$ states, respectively. These peaks were positively shifted compared to the pure metallic state of Pt 4f on commercial Pt/C which were located at 70.7 eV and 74.2 eV for Pt $4f_{7/2}$ and Pt $4f_{5/2}$, respectively. The positive shifts were interpreted in many previous studies for two major reasons. First, the effect of the difference in electronegativity between the Pt and the carbon shell.[34-36] Pt transfers its electron to the carbon shell making itself less electron-dense. Besides, this effect was enhanced by nitrogen atoms doped to the carbon shell where the nitrogen is more electronegative than carbon atoms. Thus, the upshift of binding energy on the Pt 4f state arises. The second was because of the alloying effect on the Pt with a secondary

metal.[37] Generally, the work function of metals descends from Pt > Pd > Au > Ag. The electron transfer must move from other metal to Pt. This should tend to cause a negative shift of the binding energy. However, it upshifts the Fermi level of the Pt electronic structures resulting in an opposite downshift of the d-band center, as well as the Pt 4f. Therefore, it strengthened the binding energy found in photoelectron measurements. Additionally, the deconvoluted of the Au 4f, Ag 3d, and Pd 3d peaks were also exhibited in Figure 4.6 (e–g). The relative integrated area for each species in the Au 4f and Ag 3d peaks of the PtAu-NFG and PtAg-NFG sample could indicate that the oxide species were rarely found,[38, 39] compared to that of the PtPd-NFG sample. The deconvoluted peaks of the Pt 4f and Pd 3d from the PtPd-NFG sample could suggest that there should be the presence of the PtO and PtO_2 and PdO, respectively,[40, 41] with relatively high amounts. According to the previous study, the reactivity and oxygen-binding for the Pt, Pd, Au, and Ag atoms were diagnosed by the density functional theory (DFT) calculations.[42] The adsorption and reaction with oxygen were found to be exothermic for the Pt and Pd and favoured to form oxides of the Pt and Pd, respectively. Meanwhile, the Au or Ag could lead to an endothermic reaction which was more difficult to form bonds with oxygen. As result, the presence of the oxide species at the core structure was also reported that they could affect the formation of the graphene layer.[43] When the oxygen has existed on the metal-core, it could hinder the formation of the larger size graphene flakes, due to the diminishing the graphene nucleation density. Therefore, the metals without the presence of the oxides could give the formation of the compact graphene. Accordingly, it could explain the relatively high density of defect sites, from the Raman results.

Table 4.3 Atomic compositions of Pt-NFG, PtAu-NFG, PtAg-NFG, and PtPd-NFG by XPS.

Sample	Atomic composition (at%)					Doping ratio		
	C	N	O	Pt	M	N/C	O/C	M/Pt
PtAu-NFG	82.54	1.89	3.77	3.99	7.81	0.023	0.046	1.957
PtAg-NFG	84.82	2.87	5.80	4.60	1.91	0.034	0.068	0.415
PtPd-NFG	73.04	1.58	17.63	3.00	4.74	0.022	0.241	1.580

*M represented secondary metal in the Pt-based bimetallic catalysts.

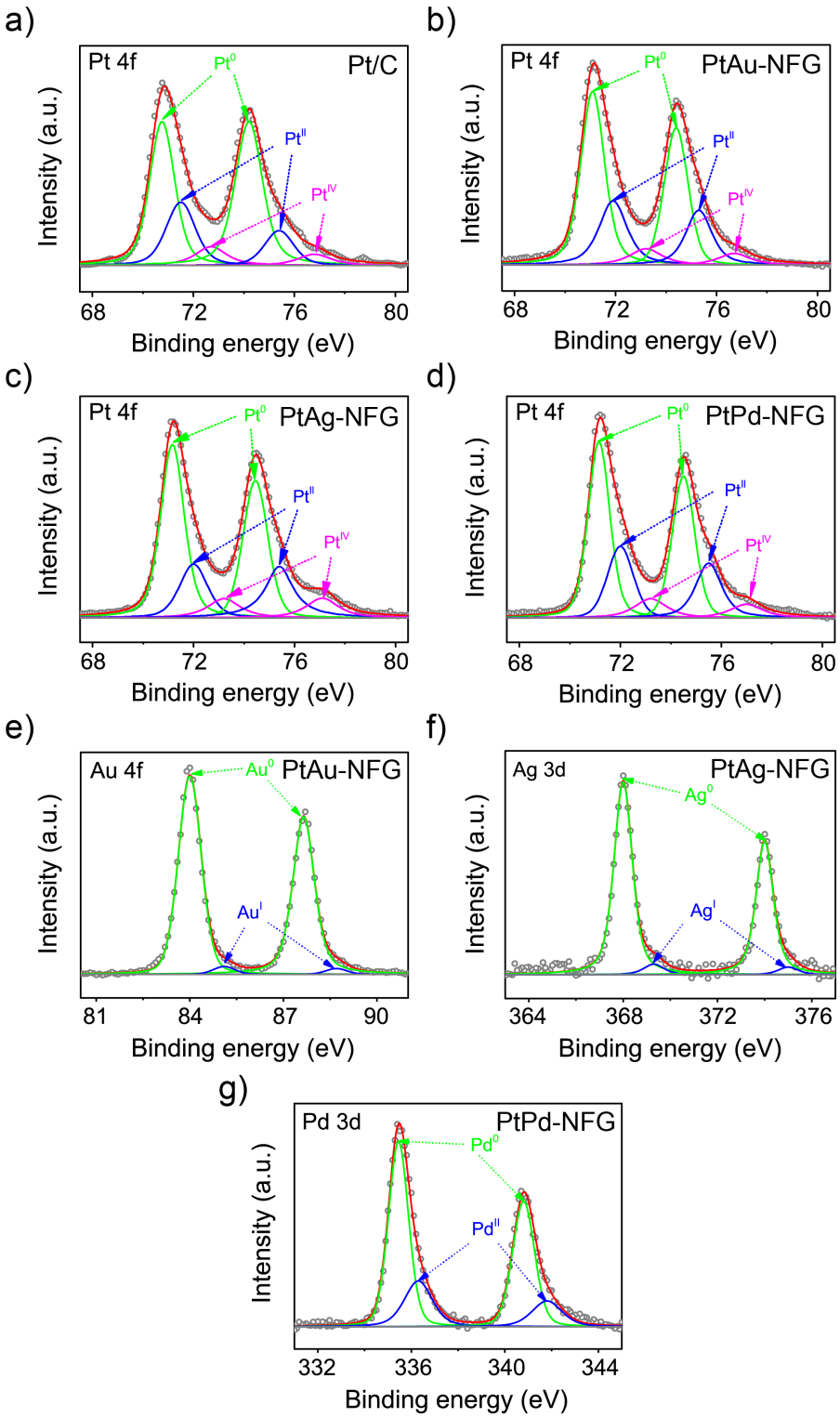

Figure 4.6 Deconvoluted XPS results of Pt 4f peaks of commercial Pt/C (a), PtAu-NFG (b), PtAg-NFG (c), PtPd-NFG (d), Au 4f of PtAu-NFG (e), Ag 3d of PtAg-NFG (f), and Pd 3d of PtPd-NFG (g).

The CV method was done to identify the ORR activity of the obtained samples. They were performed in the 0.5 M H_2SO_4 electrolyte in the presence of the O_2 bubbling with the scan rate at 50 $mV \cdot s^{-1}$ (Figure 4.7 (a)). The potential between 0.0 to 0.4 V (V vs. RHE) was attributed to the hydrogen region, which can indicate the hydrogen adsorption and desorption abilities of catalysts.[44] The result pointed out that the obtained NFG encapsulated the PtM bimetallic nanoparticles showed lower ability to adsorb and desorb hydrogen molecules, compared to that of the commercial Pt/C sample. At the oxygen region of the potential ranging from 0.4 to 1.4 V (V vs. RHE), the CV curves revealed the peaks referring to the electrochemical properties toward ORR. The ORR peaks of the Pt-NFG, PtAu-NFG, PtAg-NFG, and PtPd-NFG samples appeared at 0.706, 0.702, 0.698, and 0.669 V (V vs. RHE), respectively. As a result, the peak potentials showed negative shifts compared to that of the commercial Pt/C sample. For current density, the PtPd-NFG sample could provide comparable value to that obtained from the commercial Pt/C sample, while other samples showed relatively lower current density.

Moreover, the LSV measurements of an RRDE were conducted with the rotation speed of 1600 rpm with the potential sweep in the negative direction from 1.2 to 0.2 V (V vs. RHE) to gain more information about the ORR performance as showed in Figure 4.7 (b). The tested samples indicated the close onset potential values at around 0.880 V (V vs. RHE) which indicated the comparable catalytic performance of our synthesized samples to the commercial Pt/C sample. Nevertheless, the rise in the current density in the kinetic-diffusion mixed region indicated the different rates which represented the various ORR activity of the synthesized sample. The quantitative of the catalysts in this region can be represented by the haft-wave potential ($E_{1/2}$).[45] All the synthesis samples indicated the lower $E_{1/2}$ values comparing to that of the commercial Pt/C sample which indicated that the ORR rates are slower than the diffusion rates in the core-shell samples. The low ORR rate occurred in the kinetic-diffusion mixed region related to poor O_2 diffusion from the electrolyte due to the hydrophobicity of the NFG coating. Nevertheless, the Pt-NFG, PtAu-NFG, PtAg-NFG, and PtPd-NFG sample could give the current density from the disk electrode at 4.314, 4.018, 4.125, and 4.228 $mA \cdot cm^{-2}$, which was almost comparable to the

correlation values of the commercial Pt/C sample (at 4.438 $mA \cdot cm^{-2}$) after reach to the diffusion-controlled region. The comparison of the onset potential and diffusion-limited current density values of the obtained catalysts with the core-shell structure in this work led to the comparable ORR performance compared to the commercial Pt/C sample, which is the Pt deposited carbon structure. This evidence suggested that the few-layer heteroatom-doped graphene might be the key for preserving the ORR activity of the core-shell sample in this study, while the previous study reported that the pristine graphene shell could alter the active surface of metal-core.[46] Furthermore, the formation of hydrogen peroxide and the corresponding electron transfer number per O_2 was then discovered as equations below:

$$n = 4 \times \frac{I_{disk}}{I_{disk} + I_{ring}/N} \quad (1),$$

$$\%H_2O_2 = \frac{200 \times I_{ring}}{N \times I_{disk} + I_{ring}} \quad (2).$$

Where I_{disk} and I_{ring} are the observed currents from the RRDE at the glassy carbon disk and Pt ring, respectively. N is the collection efficiency which was obtained at 0.482 using 0.1 M $HClO_4$ with a 10 mM $K_3Fe(CN)_6$ electrolyte. As the result in Figure 4.7 (c), the n values of the obtained samples in this work derived from the RRDE measurements were ranging from 3.92 to 3.98. Notably, the n values of the PtAg-NFG and PtPd-NFG samples was higher than that of the commercial Pt/C sample in the whole measurement range. The significantly low percentages of generated H_2O_2 (1–4 %) were observed for all obtained samples, which was comparable to that of the commercial Pt/C sample. In the light of the evidence, it could be proposed that the obtained PtM bimetallic nanoparticles encapsulated with the NFG coating tended to catalyze the ORR through the direct four-electron pathway, similar to the commercial Pt/C sample.

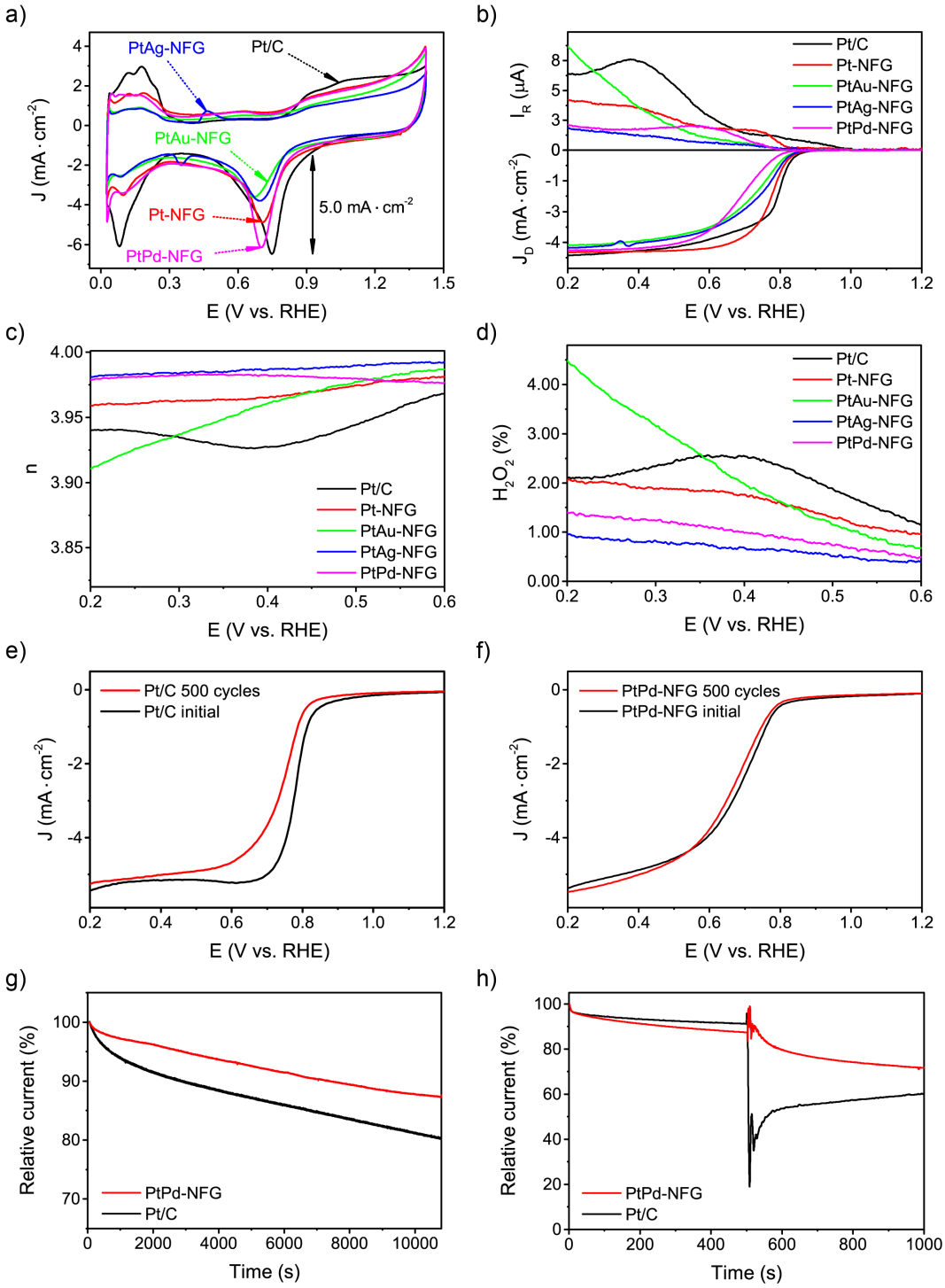

Figure 4.7 CV curves with scan rate at 50 $mV \cdot s^{-1}$ (a), LSV curves (b), electron transfer number (n) values (c), and H_2O_2 yields (d) with scan rate at 10 $mV \cdot s^{-1}$. LSV curves of Pt/C (e) and PtPd-NFG (f) at initial and after 500 CV cycles with scan rate at 10 $mV \cdot s^{-1}$. I-t curves of PtPd-NFG and Pt/C at 0.4 V (V vs. RHE) (g). I-t curves of PtPd-NFG and Pt/C at 0.6 V (V vs.RHE) followed by adding of 3 M MeOH (h).

Figure 4.7 (e, f) shows the LSV results of the PtPd-NFG and Pt/C samples at initial and after 500 CV cycles. The LSV curves of the commercial Pt/C sample exhibited a significant change in the onset of the potential and the limiting current density between the initial and 500th cycle measurement. On the other hand, there was no significant change that could be observed in the LSV of the PtPd-NFG sample. In addition, the chronoamperometric test was also conducted and the results were shown in Figure 4.7 (g). In the beginning, the commercial Pt/C sample showed the rapid drop of the current, while the PtPd-NFG sample gave the decrement of the current with a slower rate. In summary, our obtained core-shell catalyst, e.g., PtPd-NFG, revealed the higher durability, compared to that of the commercial Pt/C sample, which might be related to the protective ability of the NFG shell. Besides that, to investigate the durability and tolerance of the obtained catalyst to the MeOH in an acidic electrolyte, we conducted the MeOH tolerance test with the addition of 3 M MeOH after 500 s chronoamperometric measurement at 0.6 V (V vs. RHE) and rotating speed at 1600 rpm. The result was shown in Figure 4.7 (h). By adding 3 M MeOH during the chronoamperometric tests, the significant current decrease was found in the commercial Pt/C system, while the PtPd-NFG system showed a slight drop of the current. This result confirms that the synthesized core-shell structured catalyst by the SP technique in this work had better durability and MeOH tolerance in the acidic solution compared to those of the commercial Pt/C sample. Accordingly, it could imply that the NFG shell could act as the protective barrier which helps to improve the chemical stability of the catalyst.

Single-cell test of a catalyst was also applied for identifying the potential for practical applications. The comparison of the catalytic performances of the PtPd-NFG and commercial Pt/C sample was evaluated by applying them as the cathode for a single-cell test at 80 ºC with the results showed in Figure 4.8 (a). The open-circuit voltage (OCV) values of the PtPd-NFG and commercial Pt/C samples were similar at around 0.9 V. The maximum power densities (P_{max}) of the PtPd-NFG and Pt/C samples were 427 and 379 mW·cm^{-2}, respectively. Besides, the commercial Pt/C samples showed the rapid drop of the current density which indicated the more gas transport loss due to the generation of the water on the surface of the catalyst.[47] Meanwhile,

the PtPd-NFG sample, having the carbon coating, which is hydrophobic, could prevent the water molecules, leading to effectively facilitate the mass transfer.[48] Accordingly, the catalytic performance of the PtPd-NFG cathode was better than that of the Pt/C cathode. Figure 4.8 (b) presents the EIS as the Nyquist plots of the PtPd-NFG-based MEA (above) and Pt/C-based MEA (below). The equivalent circuit was applied to fit the observed impedance spectra. Each spectrum exhibits only one loop corresponding to charge transfer resistance (R_{ct}). The high-frequency intercept at the real impedance axis corresponds to the ohmic resistance of the cell (R_{Ω}). R_{Ω} and R_{ct} resistances were 0.09 and 0.50 $\Omega \cdot cm^2$ for the PtPd-NFG sample and 0.31 and 0.74 $\Omega \cdot cm^2$ for the commercial Pt/C sample at 0.7 V, respectively. The commercial Pt/C sample indicated the higher ohmic resistance which is related to the fabricated water absorption on the catalyst which was reduced the active sites.[49] Besides that, the R_{ct} of the PtPd-NFG-based MEA showed a low value compared to that of the Pt/C-based MEA, which could imply that charge transfer could be effectively facilitated during the fuel cell operation of the PtPd-NFG-based MEA. It was probably due to the NFG shell which can promote the ability of the charge transfer from the catalyst.[50] Furthermore, the lower value of the total impedance from the PtPd-NFG-based MEA at 0.40 $\Omega \cdot cm^2$ compared to that of the Pt/C-based MEA at 0.72 $\Omega \cdot cm^2$ at 0.6 V demonstrated that the synthesized sample indicated the better fuel cell performance.[51]

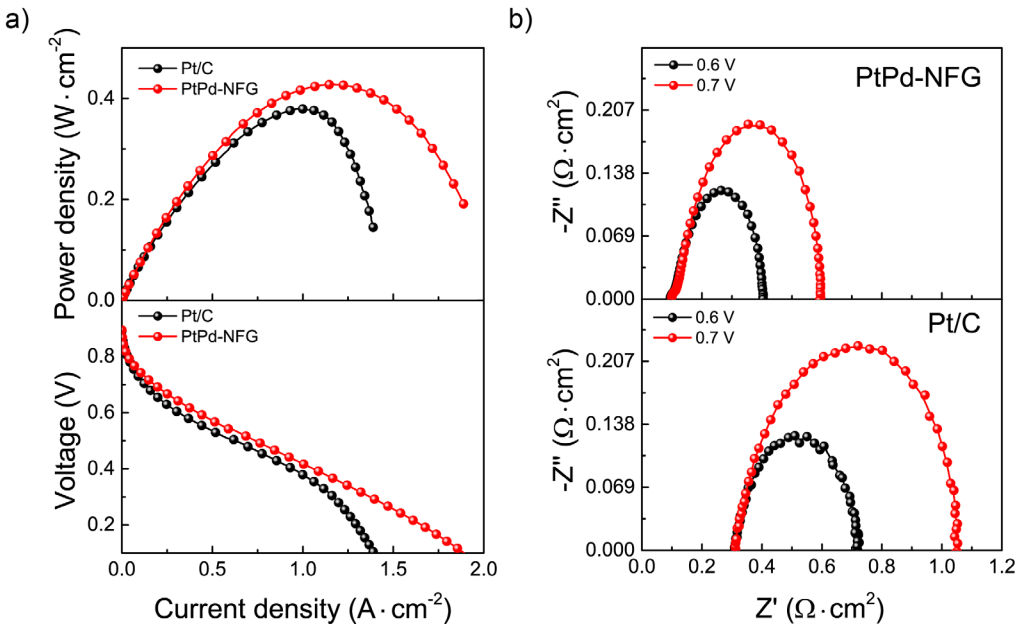

Figure 4.8 I–V–P (a) and EIS (b) results from single-cell testing of commercial Pt/C and PtPd-NFG at 80ºC.

4.4 Summary

In conclusion, we have designed and presented the efficient strategy to synthesize the NFG coating encapsulated on the PtM bimetallic nanoparticles as the efficient ORR catalysts. The synthesis was successfully conducted in one pot *via* the SP method using only the DMF precursor for the carbon source and a pair of the Pt and M electrodes for the metal source at room temperature and atmospheric pressure. The PtM bimetallic core can be tuned by varying electrodes, while various heteroatom doped shell can be prepared by simply changing precursors. The NFG played an important role in the protective shell, which helps to improve the durability of the catalyst in comparison to the commercial Pt/C. Also, the incorporation of nitrogen atoms in the carbon framework of the graphene shell could collaborate with the PtM bimetallic core, leading to the ORR with high selectivity toward the four-electron pathway which is the desired reaction for the fuel cell applications. This may open a great opportunity for further development to achieve a new high-performance catalyst *via* facile and tunable synthesis method, solution plasma, that can meet the economic feasibility and environmental concerns.

References

1. B. Gou, W. Na and B. Diong, Fuel cells: modeling, control and applications, *CRC press*, 2017.
2. S. J. Peighambardoust, S. Rowshanzamir and M. Amjadi, *Acc. Chem. Res.*, 2010, **35**, 9349-9384.
3. L. Yang, J. Shui, L. Du, Y. Shao, J. Liu, L. Dai and Z. Hu, *Adv. Mater.*, 2019, **31**, 1804799.
4. O. T. Holton and J. W. Stevenson, *Platinum Met. Rev.*, 2013, **57**, 259-271.
5. M. Ammam and E. B. Easton, *J. Power Sources*, 2013, **236**, 311-320.
6. Y. Zhao, J. Liu, Y. Zhao and F. Wang, *Phys. Chem. Chem. Phys.*, 2014, **16**, 19298-19306.
7. H. Abe, J. Liu and K. Ariga, *Mater. Today*, 2016, **19**, 12-18.
8. K.-S. Lee, H.-Y. Park, H. C. Ham, S. J. Yoo, H. J. Kim, E. Cho, A. Manthiram and J. H. Jang, *J. Phys. Chem. C*, 2013, **117**, 9164-9170.
9. S. Beckord, A. K. Engstfeld, S. Brimaud and R. J. Behm, *J. Phys. Chem. C*, 2016, **120**, 16179-16190.
10. Y. Tang, F. Gao, S. Mu, S. Yu and Y. Zhao, Russ. *J. Electrochem.*, 2015, **51**, 345-352.
11. S. G. Peera, T. G. Lee and A. K. Sahu, *Sustain. Energy Fuels*, 2019, **3**, 1866-1891.
12. M. Shao, J. H. Odell, A. Peles and D. Su, *Chem. Commun.*, 2014, **50**, 2173-2176.
13. C. Zhang, X. Shen, Y. Pan and Z. Peng, *Front. Energy Res.*, 2017, **11**, 268-285.
14. M. González-Hernández, E. Antolini and J. Perez, *Int. J. Hydrogen Energy*, 2020, **45**, 5276-5284.
15. B. P. Vinayan, R. Nagar, N. Rajalakshmi and S. Ramaprabhu, *Adv. Funct. Mater.*, 2012, **22**, 3519-3526.
16. X. Zhong, W. Xu, L. Wang, Y. Qin, G. Zhuang, X. Li and J.-g. Wang, *Catal. Sci. Technol.*, 2016, **6**, 5942-5948.
17. X. Liu, Y. Sui, T. Duan, C. Meng and Y. Han, *Catal. Sci. Technol.*, 2015, **5**, 1658-1667.
18. S. Chen, A. Zehri, Q. Wang, G. Yuan, X. Liu, N. Wang and J. Liu, *ChemistryOpen*, 2019, **8**, 58-63.
19. W. Lei, H. M. Barnes, J. Zhang and Z. Cai, *Wood Fiber Sci.*, 2017, **49**, 22-32.

20. T. Morishita, T. Ueno, G. Panomsuwan, J. Hieda, A. Yoshida, M. A. Bratescu and N. Saito, *Sci. Rep.*, 2016, **6**, 36880.
21. X. Hu, X. Shen, O. Takai and N. Saito, *J. Alloys Compd.*, 2013, **552**, 351-355.
22. S. Chae, G. Panomsuwan, M. A. Bratescu, K. Teshima and N. Saito, *ACS Appl. Nano Mater.*, 2019, **2**, 1350-1355.
23. O. L. Li, S. Chiba, Y. Wada, G. Panomsuwan and T. Ishizaki, *J. Mater. Chem. A*, 2017, **5**, 2073-2082.
24. M. A. Bratescu, O. Takai and N. Saito, *J. Alloys Compd.*, 2013, **562**, 74-83.
25. F. T. Johra, J.-W. Lee and W.-G. Jung, *J. Ind, Eng. Chem.*, 2014, **20**, 2883-2887.
26. T. Daio, A. Staykov, L. Guo, J. Liu, M. Tanaka, S. M. Lyth and K. Sasaki, *Sci. Rep.*, 2015, **5**, 13126.
27. E. Westsson, S. Picken and G. Koper, *Chem. Commun.*, 2019, **55**, 1338-1341.
28. A. Balkis and A. P. O'Mullane, *Mater. Chem. Phys.*, 2014, **143**, 747-753.
29. K. Hyun, T. Ueno, O. L. Li and N. Saito, *RSC Adv.*, 2016, **6**, 6990-6996.
30. C. H. Choi, S. H. Park and S. I. Woo, *J. Mater. Chem.*, 2012, **22**, 12107-12115.
31. G. Panomsuwan, N. Saito and T. Ishizaki, *J. Mater. Chem. A*, 2015, **3**, 9972-9981.
32. P. R. Kidambi, C. Ducati, B. Dlubak, D. Gardiner, R. S. Weatherup, M.-B. Martin, P. Seneor, H. Coles and S. Hofmann, *J. Phys. Chem. C*, 2012, **116**, 22492-22501.
33. P. Tan, W. Han, W. Zhao, Z. Wu, K. Chang, H. Wang, Y. Wang, N. Bonini, N. Marzari and N. Pugno, *Nat. Mater.*, 2012, **11**, 294-300.
34. J. Ma, A. Habrioux, Y. Luo, G. Ramos-Sanchez, L. Calvillo, G. Granozzi, P. B. Balbuena and N. Alonso-Vante, *J. Mater. Chem. A*, 2015, **3**, 11891-11904.
35. P. Kannan, T. Maiyalagan, N. G. Sahoo and M. Opallo, *J. Mater. Chem. B*, 2013, **1**, 4655-4666.
36. T. Holme, Y. Zhou, R. Pasquarelli and R. O'Hayre, *Phys. Chem. Chem. Phys.*, 2010, **12**, 9461-9468.

37. M. Wakisaka, S. Mitsui, Y. Hirose, K. Kawashima, H. Uchida and M. Watanabe, *J. Phys. Chem. B*, 2006, **110**, 23489-23496.
38. N. J. Firet, M. A. Blommaert, T. Burdyny, A. Venugopal, D. Bohra, A. Longo and W. A. Smith, *J. Mater. Chem. A*, 2019, **7**, 2597-2607.
39. J.-P. Sylvestre, S. Poulin, A. V. Kabashin, E. Sacher, M. Meunier and J. H. Luong, *J. Phys. Chem. B*, 2004, **108**, 16864-16869.
40. J. H. Kim, J. Y. Cheon, T. J. Shin, J. Y. Park and S. H. Joo, *Carbon*, 2016, **101**, 449-457.
41. G. K. Reddy, C. Ling, T. C. Peck and H. Jia, *RSC Adv.*, 2017, **7**, 19645-19655.
42. L. Xiao and W. F. Schneider, *Chem. Phys. Lett.*, 2010, **484**, 231-236.
43. Y. Hao, M. S. Bharathi, L. Wang, Y. Liu, H. Chen, S. Nie, X. Wang, H. Chou, C. Tan, B. Fallahazad, H. Ramanarayan, C. W. Magnuson, E. Tutuc, B. I. Yakobson, K. F. McCarty, Y.-W. Zhang, P. Kim, J. Hone, L. Colombo and R. S. Ruoff, *Science*, 2013, **342**, 720-723.
44. D. Zhan, J. Velmurugan and M. V. Mirkin, *J. Am. Chem. Soc.*, 2009, **131**, 14756-14760.
45. L. Zhang, L. Fan, P. Yang, M. Li, H. Zhang, Y. Tang, Z. Kang, H. Guo, R. Wang and D. Sun, *Materials Advances*, 2020.
46. M. Topsakal, H. Şahin and S. Ciraci, *Phys. Rev. B*, 2012, **85**, 155445.
47. Q. Yan, H. Toghiani and H. Causey, *J. Power Sources*, 2006, **161**, 492-502.
48. S. Yu, X. Li, S. Liu, J. Hao, Z. Shao and B. Yi, *RSC Adv.*, 2014, **4**, 3852-3856.
49. B. Najafi, P. Bonomi, A. Casalegno, F. Rinaldi and A. Baricci, *Energies*, 2020, **13**, 3643.
50. Y. Xue, J. M. Baek, H. Chen, J. Qu and L. Dai, *Nanoscale*, 2015, **7**, 7078-7083.
51. B. Y. Kaplan, N. Haghmoradi, E. Biçer, C. Merino and S. A. Gürsel, *Int. J. Hydrogen Energy*, 2018, **43**, 23221-23230.

Chapter 5

Summary

Chapter 5 - Summary

In the thesis, the research of exploring the simple synthesis and evaluation of the metal-carbon core-shell catalysts for the proton exchange membrane fuel cell (PEMFC) was introduced. At first, the investigation of the one-pot synthesis of the metal nanoparticle coated by the nitrogen-doped few-layer graphene core-shell (M-NFG) by solution plasma was illustrated. The solution plasma synthesis of M-NFG was demonstrated as the fast route during the coexist of two processes of the carbonization from the carbon precursor and metal sputtering from electrodes at the plasma zone. From a practical point of view, the solution plasma has been indicated as an excellent alternative technique for the M-NFG core-shell synthesis due to its simple setup, ambient temperature and pressure condition, facile synthesis process, and controllable products. Secondly, the benefits of the NFG coating were demonstrated in terms of the high protection ability barriers for metal-core as well as the efficient support for enhancing the catalytic performance of the catalyst. The high protection abilities of the NFG were illustrated and compared using copper, a very poor oxidation resistance material, as the metal core of the coated and uncoated samples. Besides that, the platinum nanoparticle encapsulated by NFG was also synthesized for the study of the catalytic performances in oxygen reduction reaction, compared to commercial Pt/C. Finally, the Pt-based bimetallic nanoparticle coated by the NFG catalyst was successfully synthesized *via* solution plasma for the first time and introduced with the research in use for the PEMFC. Due to the partly substituted Pt by the Au, Ag, or Pd, the catalyst with higher durability and comparable ORR activity, compared to commercial Pt/C, was discovered.

In chapter 1, the introduction of the main thesis target of using Pt-based bimetallic for use in PEMFC was introduced. The general introduction of the PEMFC was introduced in detail in terms of the reaction route for the electron generation, the single-cell setup, and the catalyst for the cathode electrode. The literature reviews of the development of the efficient catalysts for the PEMFC were also introduced in this chapter followed by the conventional methods for the

synthesis of the metal-coated by carbon material. As of last, the brief introduction of solution plasma was mentioned for the new method of synthesis of the Pt-based bimetallic nanoparticle covered by the NFG coating.

In chapter 2, the synthesis of the copper nanoparticles coated with nitrogen-doped few-layer graphene (Cu-NFG) was synthesized in one pot *via* the SP process. By changing the repetition frequencies at 100 kHz and 200 kHz, the core-shell structure of the Cu-NFG samples was evaluated with the nano size of Cu nanoparticles at below 10 nm as well as the thin NFG coating with the number of graphene less than 5 layers. By evaluating the plasma synthesis process and material characterization, the explanation of the SP synthesis of the Cu-NFG core-shell nanoparticle was illustrated in detail. Furthermore, the protection ability of the NFG coating was successfully evaluated by immersion test in nitric acid and sulfuric acid solutions. To be the outstanding protection coating, the Cu-NFG sample of 3 to 5 layers of the NFG shell indicated the very low corrosion rate which confirms at 0.208 x 10^{-12} mol·cm^{-2}·h^{-1} in nitric acid solution and 0.031 x 10^{-12} mol·cm^{-2}·h^{-1} in sulfuric acid solution.

In chapter 3, the Pt electrode was selected to fabricate the Pt nanoparticle coated by the NFG (Pt-NFG). The synthesized Pt-NFG sample indicated the smaller particle size with the higher crystallinity of the Pt-core comparing to commercial Pt/C. The cyclic voltammetry and linear sweep voltammogram results indicated the possible reaction mechanism in the Pt-NFG catalyst which occurred at the NFG shell. Besides that, the XAFS results were also indicated that the commercial Pt/C structure was changed after the electrochemical measurement. Lastly, the higher durability in the PEMFC testing condition of the Pt-NFG sample compared with commercial Pt/C was also demonstrated in both conditions of with and without applying a static potential.

In chapter 4, the SP synthesis of the new catalyst structure of Pt-based bimetallic coated by NFG was displayed. The reduction of Pt amount by the other metal was evaluated using the TEM-EDS and XPS measurements. Especially, 60 % of Pt were replaced by the Au in the synthesized bimetallic cores when the pairs of the Pt-Au electrodes were used for the plasma

discharge in the dimethylformamide solution. For the ORR performance, the Pt-based bimetallic coated by the NFG indicated the higher electron transfer number compared with the commercial Pt/C. Besides that, the PtPd bimetallic nanoparticles covered by the NFG coating core-shell (PtPd-NFG) indicated the higher durability during the chronoamperometric measurement with and without the addition of methanol. Furthermore, the PtPd-NFG sample was demonstrated the better performance in the single-cell test comparing to commercial Pt/C due to the higher peak power density as well as the lower charge transfer resistance.

In summary, we successfully synthesized the new type of catalyst for the PEMFC application. From all mentioned shreds of evidence, we believe that our new type of catalyst with the high durability as well as high power density will be the good alternative catalyst for applying in the PEMFC industry.

Achievements

List of publications

1. Phu Quoc Phan, Sangwoo Chae, Phuwadej Pornaroontham, Yukihiro Muta, Kyusung Kim, Xiaoyang Wang, Nagahiro Saito, "In Situ Synthesis of Copper Nanoparticles Encapsulated by Nitrogen-Doped Graphene at Room Temperature via Solution Plasma", RSC Advances, Vol.10, pp.36627-36635 (2020)
2. Phu Quoc Phan, Rinyarat Naraprawatphong, Phuwadej Pornaroontham, Junmu Park, Chayanaphat Chokradjaroen, Nagahiro Saito, "N-Doped Few-Layer Graphene Encapsulated Pt-Based Bimetallic Nanoparticles via Solution Plasma as An Efficient Oxygen Catalyst for The Oxygen Reduction Reaction", Published by Materials Advances (2020)
3. Sangwoo Chae, Phu Quoc Phan, Gasidit Panomsuwan, Maria Antoaneta Bratescu, Takeshi Hashimoto, Katsuya Teshima, Nagahiro Saito, "Single-Walled Carbon Nanotubes Wrapped by Cationic Nitrogen-Doped Carbon for Electrocatalytic Applications", ACS Applied Nano Materials, Vol.3, No. 10, pp.10183-10189 (2020)

List of international conferences

1. Phu Quoc Phan, Kyusung Kim, Yukihiro Muta, Tipplook Mongkol, Sangwoo Chae, Nagahiro Saito, Analyzing properties of nitrogen, boron and nitrogen-boron doped few-layer graphene-coated copper nanoparticles synthesized by solution plasma for oxygen reduction reaction catalyst, Materials Research Meeting 2019, December 10-14, Yokohama (Japan), p.7 (2019).
2. Phu Quoc Phan, Kyusung Kim, Yukihiro Muta, Tipplook Mongkol, Sangwoo Chae, Nagahiro Saito, Solution Plasma Synthesis of Nitrogen-doped few-layer graphene-coated copper and silver nanoparticles for oxygen reduction reaction catalyst under acid condition, 12th Asian-European International Conference on Plasma Surface Engineering, September 01-05, Jeju (Korea), p.79 (2019).
3. Phu Quoc Phan, Kyusung Kim, Yukihiro Muta, Tipplook Mongkol, Sangwoo Chae, Bratescu Maria Antoaneta, Nagahiro Saito, Solution plasma synthesis of core-shell copper particle

protected by nitrogen-doped multilayer graphene as an oxygen reduction reaction catalyst, The International Conference on Advanced and Applied Petroleum, Petrochemicals, and Polymers 2018, December 18-20, Bangkok (Thailand), p.26 (2018).

4. Phu Quoc Phan, Kyusung Kim, Yukihiro Muta, Tipplook Mongkol, Sangwoo Chae, Bratescu Maria Antoaneta, Nagahiro Saito, Solution plasma synthesis of core-shell copper particle protected by nitrogen-doped multilayer graphene as an oxygen reduction reaction catalyst, The Final Seminar on JSPS Core-to-Core Program (B. Asia-Africa Science Platforms) Establishment of Research Hub for Compact Mobility Model in the ASEAN Region, December 12-14, Vientiane (Laos), p.30 (2018).

List of domestic conference

1. Phu Quoc Phan, Kyusung Kim, Yukihiro Muta, Tipplook Mongkol, Sangwoo Chae, Nagahiro Saito, A one-step procedure for synthesizing core-shell nanospheres of metal nanoparticles protected by nitrogen-doped few-layer graphene, 3rd Smart Materials Research Meeting Lecture, November 26, Tokyo, (Japan), p.32 (2019).

List of awards

1. Poster rewards, A one-step procedure for synthesizing core-shell nanospheres of metal nanoparticles protected by nitrogen-doped few-layer graphene, 3rd Smart Materials Research Meeting Lecture, Tokyo, (Japan), (2019).
2. The Macromolecular Materials and Engineering poster award in Sustainable Energy, Solution plasma synthesis of core-shell copper particle protected by nitrogen-doped multilayer graphene as an oxygen reduction reaction catalyst, The International Conference on Advanced and Applied Petroleum, Petrochemicals, and Polymers 2018, Bangkok (Thailand), (2018).
3. The Reaction Chemistry & Engineering poster award, Solution plasma synthesis of core-shell copper particle protected by nitrogen-doped multilayer graphene as an oxygen reduction reaction catalyst, The International Conference on Advanced and Applied Petroleum, Petrochemicals, and Polymers 2018, Bangkok (Thailand), (2018).